Universitat Politècnica de València

Departamento de Sistemas Informáticos y Computación

Instituto de Instrumentación Para Imagen Molecular

Optimisation of nonlinear photonic devices: design of optical fibre spectra and plasmonic systems

tesi doctoral

carles milián i enrique

directors

vicente hernández garcía

albert ferrando i cogollos

València, Gener 2012

Als meus pares, Pau, Pilar i la meva germana
A la flor del cel

No hi ha meta que no esdevinga
punt de partida, dinàmica de la cadència,
virtut de la experiència.

Resum

El propòsit d'aquesta tesi és dissenyar i optimitzar dispositius fotònics en el règim no lineal. En particular, s'han triat dos tipus de dispositius, que es classifiquen d'acord amb el fenomen físic d'interés. El primer tipus correspon a fibres convencionals o del cristall fotònic, dissenyades per tal que la dinàmica temporal dels paquets d'ona que es propaguen al seu interior, genere espectres amb les característiques desitjades, en el context del supercontinu. El segon tipus explota la fenomenologia espacial associada a les ones electromagnètiques que es propaguen sobre la superfície d'un metall. Aquestes permeten, des de dissenyar dispositius tipus *chip* fotònic, llurs dimensions típiques estan molt per sota la longitud d'ona de la llum, fins la generació d'estats no lineals híbrids de dinàmica singular.

Tots aquests efectes es troben dintre del marc proporcionat per les equacions de Maxwell macroscòpiques, que s'han resolt numèricament. En alguns casos grans aproximacions teòriques les simplifiquen a sistemes uni-dimensionals, mentre que en d'altres, s'integren directament en les tres dimensions espacials. En el cas en que la optimització del dispositiu en qüestió resulta no trivial després del coneixement que s'ha adquirit del mateix de manera teòrica, s'empra una recent eina numèrica que sorgeix de la combinació d'algoritmes genètics i plataforma *Grid*.

Resumen

El propósito de esta tesis es diseñar y optimizar dispositivos fotónicos en el régimen no lineal. En particular, se han elegido dos tipos de dispositivos, que se clasifican según los fenómenos físicos de interés. La primera clase corresponde a fibras convencionales o de cristal fotónico, diseñadas para que la dinámica temporal de los paquetes de onda que se propagan en su interior genere espectros con las características deseadas, en el contexto del supercontinuo. La segunda clase explota la fenomenología espacial asociada a las ondas electromagnéticas que se propagan sobre la superficie de un metal. Estas ondas permiten, desde diseñar dispositivos tipo *chip* fotónico cuyas dimensiones típicas están muy por debajo de la longitud de onda de la luz, hasta la generación de estados no lineales híbridos de dinámica singular.

Todos estos efectos tienen lugar dentro del marco proporcionado por las ecuaciones de Maxwell macroscópicas, las cuales han sido resueltas numéricamente. En algunos casos se emplean grandes aproximaciones teóricas para estudiar sistemas 1D, mientras que en otros se integran directamente en 3D. En el caso en el que la optimización del dispositivo resulta no trivial tras haber adquirido un conocimiento teórico profundo del mismo, se emplea una novedosa herramienta numérica que nace de la combinación de algoritmos genéticos con plataforma *Grid*.

Abstract

The aim of this thesis is to design and optimise photonic devices in the non linear regime. In particular, two types of devices have been chosen according to the physical phenomena. The first one corresponds to optical fibres, designed so that the temporal dynamics associated to the wave-packets travelling along them generates spectra with the desired characteristics, in the context of supercontinuum. The second one exploits the spatial phenomenology associated to the electromagnetic waves at the surface of a metallic material. These waves make possible the design of photonic chips with dimensions well below the light wavelength and the generation of hybrid nonlinear states with very particular dynamics.

All these effects are found in the frame provided by the macroscopic Maxwell equations, which have been solved numerically. In some cases, big theoretical approximations have been used to study systems of one dimension, whereas in some others they have been integrated in 3D straight away. In the case in which the device optimisation is non trivial, even possessing a deep theoretical knowledge about it, a recently developed numerical tool, combining genetic algorithms and Grid technology, has been used.

Acknowledgements

I would like to express my most sincere gratitude to my supervisors Prof. Vicente Hernández García and Prof. Albert Ferrando i Cogollos for giving me the opportunity to join their groups, their supervision and also their complete trust and support during the last five years. In the same level of commitment and enthusiasm are Dr. Mario Zacarés González and Prof. Dmitry V. Skryabin, who have always believed in me and gave me all their time. I want to dedicate this thesis very warmly to them all.

I am much obliged to Prof. Vicente Vento Torres, for guiding and advising me during and after my university studies so selflessly, and to my collaborators and friends Miguel Arevalillo, Germán Moltó, Daniel Enrique, Noé González and Paco Arteaga.

To all my friends, for all the moments of fun and laugh, to Gabriel Teruel (Gabi), Nelson Delle-Vigne and Juana Martínez, whose lessons and conversations so many times inspire my thinking and life.

Contents

Resum vii

Resumen ix

Abstract xi

Acknowledgements xiii

1 Introduction 1

2 Theory of nonlinear propagation of light 7

2.1 Propagation equations of electromagnetic waves 7

2.1.1 Origin of nonlinearities 8

2.2 Linear vs nonlinear waveguide modes 11

2.2.1 Weak guidance 12

2.3 Pulses in silica fibres 13

2.3.1 Temporal solitons and the NLS equation 16

2.3.2 A note on dimensions 17

2.3.3 Lagrangian formalism 18

2.4 Continuous wave beams 21

2.4.1 Waveguide arrays: discrete NLS equation 22

3 Continuum generation by dark solitons in optical fibres 25

3.1 Perturbation of solitons and Galilean transformation 25

3.2 Radiation frequency: resonance condition 28

3.2.1 Effect of soliton greyness and frequency detuning 30

3.2.2 Numerical results 31

3.3 Radiation amplitude 34

3.3.1 Equations for the two resonant waves 35
3.3.2 Ratio between the spectral resonant peaks 39
3.3.3 Amplitude of the stronger RR root 39
3.3.4 Raman effect 44
3.4 Continuum generation in the realistic excitation 48
3.5 Conclusions: optimal supercontinuum 50

4 Polychromatic Cherenkov radiation and continuum generation in tapered fibres 53
4.1 Bright solitons and Cherenkov radiation 54
4.2 Tapered fibres 55
4.3 Cherenkov continuum with positive TOD 57
4.3.1 Higher order solitons 61
4.4 Cherenkov continuum with negative TOD 62
4.5 Compression of the radiation pulses 65
4.6 Conclusions: further optimisation 66

5 Nonlinear switching in subwavelength semiconductor on metal plasmonic waveguides 69
5.1 Nonlinear coupled oscillator model 70
5.1.1 Directional coupler 70
5.1.2 Three channel system 73
5.2 Linear surface plasmon polariton waves 75
5.3 Properties of the plasmonic modes 77
5.3.1 Linear properties 77
5.3.2 Nonlinear properties 78
5.3.3 Comparison with ”on glass” waveguides 80
5.4 Nonlinear switching: numerical results 80
5.4.1 Two waveguides: optimisation of the array geometry 82
5.4.2 Three waveguides 84
5.5 Conclusions 84

6 Existence, stability and dynamics of soliplasmons: soliton-plasmon supermodes 89
6.1 The spatial solitary wave 90
6.2 Weak coupling between linear SPP’s and spatial solitons 91
6.3 Coupled oscillator model for Metal-Dielectric-Kerr media 92
6.4 Stationary solutions 95

6.4.1 Metal-Dielectric-Kerr media 95
6.4.2 Numerical results: P-μ resonance and δ-soliplamons 97
6.4.3 Metal-Kerr media 98
6.4.4 A note on the soliplasmon waveguide: Metal-Dielectric-Kerr-Dielectric-Metal structure 99
6.5 Stability analysis: amplitude-phase dynamics 99
6.5.1 Effect of metal losses 103
6.6 Conclusions 104

7 Optimisation of a fibre based narrow-band optical source in Grid platform 107
7.1 Motivation and case study 107
7.2 The genetic algorithm 109
7.2.1 Steady state algorithm 111
7.3 The Grid service 113
7.3.1 GMarteGS: A Service-Oriented Meta-Scheduler 114
7.3.2 Interfacing the Genetic Algorithm with GMarteGS 115
7.4 Results 116
7.5 Conclusion 119

8 Conclusions and future work 121

A Numerical method to compute stationary soliplasmons 125

B Papers, conferences and workshops 129

Bibliography 131

Chapter 1

Introduction

The first motivation of this thesis is to study theoretically and by means of numerical simulations a variety of nonlinear photonic devices consisting of crafted and self-induced optical waveguides. In particular, they can be divided into two main groups. The first one is based on silica optical fibres, whereas the second one deals with metal-dielectric junctions. The physical effects are divided accordingly, in the former group we study temporal effects associated to wave packets and in the latter, spatial (monochromatic) effects in conjunction with plasmonics.

Technological applications arising from a particular physical effect require in many cases a fine tuning of the device parameters and particular excitation conditions. For this reason, the deep theoretical understanding of a particular effect or system is not the ultimate objective of this thesis, but the scope is also to apply it to the device optimisation for it to operate with the desired performance. In fact, most of the effects shown in this work only occur efficiently under very strict determined conditions, being accidental and of very low importance otherwise. Because the dynamics associated to a nonlinear system is in general very complex and can be highly unpredictable, the usage of genetic algorithms combined with Grid technology is explored in the last chapter for one particular case example. We proceed by introducing first the optimisation tool in general terms.

Genetic algorithms belong to the more general category of numerical optimisation methods called evolutionary algorithms. This class of optimisation strategies mimic some essential features of the evolutionary theories of species in nature. Schematically, this is done by assimilating each of the input parameters of the physical problem to an *individual*'s gene, constituting the genome altogether. The suitability for adaptation of a genome is evaluated by a *fitness* function, which constitutes the medium to which individuals are to adapt. The evolution towards the *best* adapted individuals is carried out by processing the data retrieved from many simulations and creating

new individuals or *off-springs*. This is done by the corresponding genetic operators, such as mutation, cross over or random generation [Ashlock06].

One key advantage of this type of methods relies on their scalability, since the number of parameters to optimise, i.e., the dimensionality of the associated space over which the values of the fitness function are extended, requires a trivial extension of the optimisation algorithm. The scalability of the computing resources is then essential to address problems of different complexities. Such a computational tool is provided by the *Grid* infrastructure, which coordinates, via the *middle-ware*, geographically de-localised resources for them to add together and work on one or several problems at a time, according to their particular needs [Foster04]. With this technology, created by Ian Foster in the 1990's, the sophisticated and expensive usage of supercomputers is avoided.

In order to understand in more detail the physical effects explored in this thesis, a general view is given below. In first place the attention is focused on temporal optics, around its most attractive effect of the last decade, i.e., supercontinuum generation in optical fibres.

Experimental observation of the nonlinear regime of optics in a macroscopic scale was just impossible before the first laser was developed in 1960 [Maiman60]. Soon after, frequency conversion effects arising due to nonlinearity started to be noted, but it was not until ten years later that [Alfano70a, Alfano70b] reported the first observation of a spectral broadening covering the whole visible spectrum in bulk BK7 glass. Typical self trapped beam filaments were observed due to the self focusing nature of the material and as a result of new wave vector components (spatial frequencies) generated by the nonlinear interaction.

The study of such spectral broadening, baptised as *supercontinuum* (SC), attracted a massive interest at the begining of this century with the development of the *Photonic Crystal Fibre* (PCF) [Russell03, Knight03]. In its original form, the first PCF was a silica fibre with a cross section consisting of an hexagonal lattice of circular air holes with a defect (absence of hole) at the centre [Ranka00], structure that was analysed theoretically by [Ferrando99]. PCF's permitted both to avoid the loss of spatial coherence, happening in Alfano's experiments, and the manipulation of the linear dispersion properties via the lattice parameters, i.e., the holes shape and spacing (see e.g. [Ferrando00]). The first SC experiment already showed a spectrum spanning over an octave at both sides of the pump wavelength [Ranka00]. The underlying physics for such SC generation was soon understood to be related to the dynamics of temporal *solitons* of the *nonlinear Schrödinger* (NLS) equation, predicted soon after Alfano's experiments by [Hasegawa73b,Hasegawa73a] and conceived for decades as information

carriers, due to their non dispersive nature [Mollenauer06]. However, the ability to engineer PCF's dispersion changed dramatically the way to perceive them, and they are nowadays widely recognised as mediators of efficient frequency conversion in the infrared and visible parts of the spectrum.

Amongst all nonlinear effects in optical fibres, two are the main ingredients for SC generation. In first place, solitons where found to emit resonant dispersive waves at a blue-shifted frequency far detuned from their carrier, if they were spectrally close to the lowest zero of the *group velocity dispersion* (GVD) wavelength of the fibre. Because of its similarities to previously well known physical effects these waves were called Cherenkov radiation [Auston84]. Second, the solitons where also observed to develop a red-shift due to the Raman effect, which was described analytically by [Gordon86]. Basic details of the underlying physics in SC, history and applications are summarised in [Dudley06] and further insight, with other nonlinear processes, are provided by [Skryabin10]. SC generation and soliton dynamics in PCF's is still a fast developing field [Stark11b, Stark11a].

The spatial effects studied in this thesis belong to the general field of *plasmonics*. In particular, we focus on phenomena involving the electromagnetic surface waves that propagate at the interface between a metal and a dielectric material, which are the so called *surface plasmon polaritons* (SPP's). The interesting property from both physical and technological view points is that these surface waves are confined well below the diffraction limit, at the subwavelength scale, so they are the first potential candidates for photonic circuitry at the nano scale [Bozhevolnyi06], already achieved in electronics. Linear plasmonics is a vast field [Zayats05], but our interest here is focused on the nonlinear dynamics of these surface waves when only the dielectric material presents a flux dependent refractive index. Technological evolution and the possibility of performing experiments at the nanosacle in the nonlinear regime, re-opened the interest in this topic only few years ago, as briefly summarised below.

A single interface between two semi-infinite dielectric and metal regions is enough to support SPP waves, which dispersion relations taking into account the nonlinear boundary conditions were already obtained more than twenty years ago [Mihalache87]. The ohmic losses inherent to metals motivated recent studies around the inclusion of gain in the dielectric material [Marini09]. The propagation of waves in this case becomes the *Ginzburg-Landau* equation, which supports bright and dark localised SPP waves [Marini10b]. Diffraction compensation of a beam propagating along a 2D metal surface has been recently shown numerically to be compensated above certain power threshold [Davoyan09] forming a spatial soliton. Extension to the two interface problem, one dielectric slab sandwiched between two metal do-

mains, has been found to support coupled SPP solutions [Davoyan08] and spatial plasmon-solitons [Feigenbaum07]. The tapering of this sandwich has been proposed to compensate for the linear losses introduced by the metal in the absence of gain in the dielectric [Davoyan10]. Periodicity effects associated to the 1D stratified problem where found to support subwavelength discrete solitons [Liu07] and more general solutions of these systems were analysed by means of coupled mode theory [Marini10a]. Examples of more realistic set-ups, involving finite waveguide sizes, are the nonlinear directional coupler [Salgueiro10], arrays of metallic nanowires embedded by nonlinear material [Ye10] and arrays in two dimensions [Wurtz06, Ye11].

In what follows, the content of the different chapters in this thesis are described. Chapter 2 starts with transparent derivation of the well known generalised-NLSE (GNLSE), used to simulate supercontinuum, pointing out all the approximations involved and their physical consequences. This equation is analysed further by means of Lagrangian and Hamiltonian formalisms, which provide valuable insight and the capability to perform numerical checks on the evolution of the Hamiltonian. The last section provides the derivation of the discrete NLS equation (DNLS) [Christodoulides88], used for the arrays of coupled waveguides and introduces some concepts used later on.

The continuum generation part of this thesis is constituted by chapters 3 and 4. They are both inspired by the typical SC spectral evolution picture formed by bright solitons and their associated Cherenkov radiation [Gorbach07]. Chapter 3 is entirely devoted to explore the possibility of generating a similar SC spectrum seeded from dark solitons. Here, first order time independent perturbation theory is used to understand the Cherenkov radiation emitted by these solitons and numerical simulations are performed to explore the influence of Raman effect and the optimised fibre parameters to excite realistically such SC [Milián09]. The second effect that captivated our attention was the possibility to enhance both the amplitude and spectral content of the Cherenkov radiation associated to a single bright soliton. This originated the chapter 4, where it is found numerically the appropriate variation in a fibre profile along propagation for this low power spectral broadening effect to be maximised.

Chapters 5 and 6 concern nonlinear plasmonics. Plasmons have been studied in this thesis always in the context of multichannel systems. In the first of these chapters, arrays of two and three coupled semiconductor on metal waveguides have been considered for the study of the nonlinear switching, i.e., suppression of the linear mode beating, occuring above the threshold power. In this case the waveguides support plasmonic modes and the coupling between them occurs through the weak electric field component, the one parallel to the metal interface, and the predictions

of the DNLSE has been compared with 3D first principle numerical modelling of the nonlinear and vectorial Maxwell equations [Milián11]. The second chapter of this part, chapter 6, focuses on a more complex system. Now a one dimensional single interface is considered to study the coupling between a plasmon at the interface and a spatial soliton, which propagates in the dielectric material and induces its own waveguide [Bliokh09]. In that sense, this is a *hybrid* coupled two channel system. Another difference with chapter 5 is now that the coupling between the soliton and plasmon channels occurs through the strongest electric field component, the one perpendicular to the interface. This hybrid coupling required going beyond the DNLSE model to qualitatively describe its physics. The forced nonlinear oscillator model is shown to provide enough insight about the stationary solutions supported by this system.

Optimisation using Grid technology consists the last part of this work and is explored in chapter 7. The SC codes implement the well known Split-Step and Runge-Kutta numerical integration methods and were developed in Matlab. This made easy the compilation into C++ language and the later integration into the Grid service. The problem presented in this thesis is the one of optimising the initial pulse parameters to obtain the maximum spectral power in a narrow and fixed frequency interval, located in this case in the anomalous GVD regime of the fibre [Moltó, Ferrando].

Conclusions of the thesis, future work and new directions to explore are exposed finally in chapter 8.

Chapter 2

Theory of nonlinear propagation of light

The purpose of this chapter is to introduce in a clear and transparent way the theoretical frame and most of the equations used in the following chapters. Section 2.1 introduces the general propagation equations, discussing the origin of nonlinearities in the materials considered for our waveguides, which are basically dielectrics and semi-conductors. The properties of waveguide modes are discussed in section 2.2 in general terms and also under the usual *weakly guiding* approximation. In section 2.3, the pulse propagation equation is derived in a slightly more general way than in the literature and the temporal solitons are introduced. Further theoretical insight is provided by the Lagrangian and Hamiltonian, which clearly show the terms responsible for the loss of energy. To finish, section 2.4 focuses on continuous wave (CW) beams in arrays of parallel waveguides, where the overlapping fields couple to each other inside the different cores.

2.1 Propagation equations of electromagnetic waves

Our starting point is the macroscopic Maxwell equations for dielectric and non-magnetic media in frequency domain,

$$\vec{\nabla}\vec{\mathcal{D}}_w = 0 \tag{2.1}$$

$$\vec{\nabla} \times \vec{\mathcal{E}}_w = i\omega\vec{\mathcal{B}}_w \tag{2.2}$$

$$\vec{\nabla}\vec{\mathcal{B}}_w \equiv 0 \tag{2.3}$$

$$\vec{\nabla} \times \vec{\mathcal{H}}_w = -i\omega\vec{\mathcal{D}}_w, \tag{2.4}$$

where $\overrightarrow{\mathcal{E}}_w$, $\overrightarrow{\mathcal{B}}_w$, $\overrightarrow{\mathcal{D}}_w$ and $\overrightarrow{\mathcal{H}}_w$ are the Fourier components of the real electric and magnetic fields, electric displacement and magnetic excitation, respectively, defined as $\overrightarrow{\psi}_w(\overrightarrow{r},\omega) \equiv \hat{\mathcal{F}}(\overrightarrow{\psi}) \equiv \int_{-\infty}^{+\infty} dt\, \overrightarrow{\psi}(\overrightarrow{r},t)e^{i\omega t} \iff \psi_w(\overrightarrow{r},-\omega) \equiv \psi_w^*(\overrightarrow{r},\omega)$. Historical reasons established the convention that $\overrightarrow{\mathcal{E}}_w$ and $\overrightarrow{\mathcal{H}}_w$ are to be incident in the volume element of the medium and the radiation-matter interaction yields to the outcomes $\overrightarrow{\mathcal{D}}_w$ and $\overrightarrow{\mathcal{B}}_w$ [Born99]. Such picture motivates the material equations, or constitutive relations,

$$\overrightarrow{\mathcal{D}}_w = \epsilon_0 \hat{\mathcal{F}}\left(\hat{\epsilon}\,\overrightarrow{\mathcal{E}}\right) \equiv \epsilon_0\,\overrightarrow{\mathcal{E}}_w + \overrightarrow{\mathcal{P}}_w\left(\overrightarrow{\mathcal{E}}_w\right) \tag{2.5}$$

$$\overrightarrow{\mathcal{B}}_w = \mu_0 \overrightarrow{\mathcal{H}}_w, \tag{2.6}$$

in which the relative permittivity tensor, $\hat{\epsilon}$, maps the incident field onto the output and the polarisation, $\overrightarrow{\mathcal{P}}_w$, accounts for the non transparent medium response to the electric field. The magnetic part is not directly scattered, according to eq. 2.6. When both electric and magnetic fields are time dependent, they automatically couple and equations 2.1-2.4 describe the propagation of light ($\omega \neq 0$) through the wave equation

$$\left(\partial_z^2 + \overrightarrow{\nabla}_\perp^2\right)\overrightarrow{\mathcal{E}}_w - \overrightarrow{\nabla}\left[\overrightarrow{\nabla}\overrightarrow{\mathcal{E}}_w\right] = -\mu_0\omega^2\overrightarrow{\mathcal{D}}_w, \tag{2.7}$$

where the subscript $\perp$ projects the corresponding vector onto the transverse plane $\hat{XY}$ and the z coordinate defines the propagation direction.

The validity of equation 2.5 relies on the light wavelength, $\lambda = 2\pi c/\omega$ in vacuum. It has to be large enough for an atom or molecules of the material to experience an almost constant field. This permits taking the averaged response of the molecules in the volume element, $\langle\overrightarrow{p}_w\rangle_V$, and assign it as a point property of that volume [Jackson62], $\overrightarrow{\mathcal{P}}_w \equiv \langle\overrightarrow{p}_w\rangle_V$, which is then the *thick* point of the above differential equations 2.1-2.6. The cut-off wavelength for the validity of these equations can be thought to be of the order of $\lambda \sim 10nm$ (beginning of the X-ray spectrum), since the density $\rho \approx 2.2$ g/cm^3 [her] and molar mass $M \approx 60gmol^{-1}$ of the silica glass (SiO_2) implies there are around 22 molecules/nm^3.

2.1.1 Origin of nonlinearities

All the physics of the light-matter interaction is contained in the polarisation introduced in eq. 2.5. Physically, a photon with visible or infra-red frequency travelling inside a piece of a transparent[1] material interacts with the atoms and molecules introducing only small perturbations (in space and time) in their electronic and vibrational

states, since the frequency is far from the resonances. A beam of photons with low intensity can be regarded to as constituted of *independent* photons, so each of them interacts with the medium as if no previous photon has passed through it. However, this picture fails for high intensities because the probability of a photon interacting with the material that still has not recovered from the interaction with the previous photons starts to increase. At this point, processes involving several photons start playing a macroscopic role in the dynamics, exciting new spatial and temporal frequencies, polarisation states and modal distributions. Formally, the equations need to include the electromagnetic field components inside the dielectric tensor, $\hat{\epsilon}$, becoming nonlinear. In particular, when the frequencies and intensities involved are such that ionisation probability is negligible, the external field $\overrightarrow{\mathcal{E}}$ is small in comparison with the internal field that the atomic nuclei exert on the electrons and $\overrightarrow{\mathcal{P}}$ may be expanded in McLaurin series around $\overrightarrow{\mathcal{E}} = \overrightarrow{0}$, $\overrightarrow{\mathcal{P}} \equiv \Sigma_{m=0}^{\infty} \overrightarrow{\mathcal{P}}^{(m)}$ [Mills91]. The $i-th$ Cartesian component of the $m-th$ order polarisation may be expressed in the time domain general form

$$\begin{aligned}
&\mathcal{P}_i^{\pi(m)}\left(\overrightarrow{r},t\right) \equiv \epsilon_0 \int_{-\infty}^{\infty} d\overrightarrow{r}_1 dt_1 \cdots d\overrightarrow{r}_m dt_m \times \\
&\hat{\chi}_{i;l_1\cdots l_m}^{\pi;\rho_1\cdots\rho_m(m)}\left(\overrightarrow{r},\overrightarrow{r}_1,\cdots,\overrightarrow{r}_m;t,t_1,\cdots,t_m\right) \times \\
&\mathcal{E}_{l_1}^{\rho_1}\left(\overrightarrow{r}_1,t_1\right)\cdots\mathcal{E}_{l_m}^{\rho_m}\left(\overrightarrow{r}_m,t_m\right),
\end{aligned} \tag{2.8}$$

where the $\hat{\chi}_{i;l_1\cdots l_m}^{\pi;\rho_1\cdots\rho_m(m)}$ is the $(m+1)-th$ order susceptibility tensor mixing polarisation states (l_m) and spatial modes (ρ_m). However, the assumption that the waveguides are single mode automatically eliminates the Greek indices. The integrals account for non local interactions in the material, being the spatial ones negligible for those considered here. So are negligible the temporal ones in spatial optics because the electromagnetic fields are assumed in the continuous wave (CW) form and generation of temporal frequencies is disregarded[2]. However, temporal nonlocalities become relevant to describe delayed nonlinear effects arising in the dynamics of ultra short pulses in silica optical fibres. The most well known of these effects is the Raman scattering (see chapters 3 and 4). This motivates the functional form for the susceptibility $\hat{\chi}_{i;l_1\cdots l_m}^{(m)} = \chi_{i;l_1\cdots l_m}^{(m)}(\overrightarrow{r})\Pi_{j:1\to m}\delta(\overrightarrow{r}-\overrightarrow{r}_j)\mathcal{R}(t-t_{k:1\to m})$, where $\mathcal{R}$ is the time response function, considered later on in section 2.3. The zero order term $(m=0)$

[1]Dielectric materials are by definition transparent in the visible spectrum. However, semiconductors can also be transparent if no transitions between the valence and conducting bands are excited. This depends much on the energy band-gap between the two bands, which is in many cases controlable by the relative concentration of the different atomic species.

of the expansion is the electric dipole moment in the absence of $\overrightarrow{\mathcal{E}}$, which vanishes for the materials of our interest. The first order term, scalar for our non birefringent materials, is the contribution to the linear refractive index $n_L = \sqrt{\epsilon_L} \equiv \sqrt{1+\chi^{(1)}}$ and all the higher order terms ($m > 1$) account for nonlinearity. Symmetry properties of the susceptibility tensors imply that all even order terms (odd order tensors) are exactly zero for amorphous materials and centrosymmetric crystals. An example of the former is the silica glass and one of the latter the zincblende cubic lattice of the AlGaAs semi-conductor. This leaves the 3rd order susceptibility (4th order tensor) as the main responsible of nonlinear effects. Symmetry also imposes restrictions on the even order tensors. In particular, only 21 components of $\hat{\chi}^{(3)}$, out of the $3^4 = 81$, are non vanishing and they satisfy [Boyd03]

$$\begin{aligned} &\chi^{(3)} \equiv \chi^{(3)}_{iiii}, \quad \chi^{(3)}_{iijj} = \chi^{(3)}_{ijij} = \chi^{(3)}_{ijji}, \quad \chi^{(3)}_{iiii} = 3\chi^{(3)}_{iijj} \\ &\forall i,j \in \{x,y,z\} \,/ i \neq j, \end{aligned} \tag{2.9}$$

what leads to a polarisation vector in the form

$$\overrightarrow{\mathcal{P}} = \overrightarrow{\mathcal{P}}^L + \overrightarrow{\mathcal{P}}^{NL} \tag{2.10}$$

$$\overrightarrow{\mathcal{P}}^L \equiv \epsilon_0 \chi^{(1)} \overrightarrow{\mathcal{E}} \tag{2.11}$$

$$\mathcal{P}^{NL}_x (\overrightarrow{r}, t) \equiv \epsilon_0 \int_{-\infty}^{\infty} dt_1 dt_2 dt_3 \mathcal{R}(t, t_1, t_2, t_3) \chi^{(3)}_{x;jkl} \mathcal{E}_j(t_1) \mathcal{E}_k(t_2) \mathcal{E}_l(t_3) + \mathcal{O}(\mathcal{E}^5). \tag{2.12}$$

Spatial dependence of the susceptibility tensor and the electric fields was not written explicitly in eqns. 2.9- 2.12. The reason is that they do depend on the coordinates in the same way in the spatially local materials. From now on this notation is adopted and only time or frequency variables will be specified to distinguish clearly the reciprocal spaces.

[2] Such an assumption makes sense only in the cases where the *group velocity dispersion* (GVD) is normal. In this regime, the CW's are stable solutions, so newly generated frequencies, e.g., from noise, do not experience the exponential intensity growth and they do not affect the system at the macroscopic scale.

2.2 Linear vs nonlinear waveguide modes

The modes of a waveguide (under our assumptions) satisfy a vectorial equation given by combining eqns. 2.5, 2.7, Fourier transform of eqns. 2.10-2.12 and the factorisation $\overrightarrow{\mathcal{E}}_\omega(x,y,z) = \overrightarrow{F}_\omega(x,y)e^{i\beta z}$, implying $\partial_z \to i\beta$, which reads,

$$\hat{\mathcal{B}}\overrightarrow{F}_{\perp,\omega} + \mu_0\omega^2\overrightarrow{\mathcal{P}}^{NL}_{\perp,\omega}\left(\overrightarrow{F}_\omega\right) = \beta^2\overrightarrow{F}_{\perp,\omega} + i\beta\overrightarrow{\nabla}_\perp F_{z,\omega}, \tag{2.13}$$

$$\left[\overrightarrow{\nabla}^2_\perp + k^2\epsilon_L\right]F_{z,\omega} + \mu_0\omega^2\mathcal{P}^{NL}_{z,\omega}\left(\overrightarrow{F}_\omega\right) = i\beta\overrightarrow{\nabla}_\perp\overrightarrow{F}_{\perp,\omega}, \tag{2.14}$$

$$\hat{\mathcal{B}} \equiv \overrightarrow{\nabla}^2_\perp - \overrightarrow{\nabla}_\perp(\overrightarrow{\nabla}_\perp\circ) + k^2\epsilon_L. \tag{2.15}$$

Here, $\overrightarrow{F}_\omega$ is the waveguide mode at the frequency ω. The *circle product* "$\circ$" is to be regarded as $(\hat{\mathcal{O}}_1\circ)\hat{\mathcal{O}}_2 \equiv (\hat{\mathcal{O}}_1\hat{\mathcal{O}}_2)$ and $k \equiv 2\pi/\lambda$. Let $\overrightarrow{F}_\omega = \overrightarrow{\Phi}_\omega$ and $\beta = \beta_L$ be the solutions of the above equation with $\overrightarrow{\mathcal{P}}^{NL}_\omega \equiv \overrightarrow{0}$. In this particular case, the transverse field eq. 2.13 can be re written in the eigenvalue form

$$\hat{\mathcal{M}}\overrightarrow{\Phi}_{\perp,\omega} = \beta^2\overrightarrow{\Phi}_{\perp,\omega}, \tag{2.16}$$

$$\hat{\mathcal{M}} \equiv \overrightarrow{\nabla}^2_\perp + \overrightarrow{\nabla}_\perp(\frac{\overrightarrow{\nabla}\epsilon}{\epsilon}\circ) + k^2\epsilon_L, \tag{2.17}$$

where the linear form of eq. 2.1, $\overrightarrow{\nabla}\left(\epsilon_L\overrightarrow{\mathcal{E}_\omega}\right) \equiv 0$, has been used.

Hence, for small nonlinearity, the modes $\overrightarrow{F}_\omega = \overrightarrow{\Phi}_\omega + \overrightarrow{\delta\Phi}_\omega$ are expected to have a propagation constant $\beta = \beta_L + \delta\beta_{NL}$ and eq. 2.13 takes the linearised form

$$\left[\hat{\mathcal{M}} - \beta_L^2\right]\overrightarrow{\delta\Phi}_{\perp,\omega} + \mu_0\omega^2\overrightarrow{\mathcal{P}}^{NL}_{\perp,\omega}(\overrightarrow{\Phi}_\omega) = \delta\beta_{NL}\left[2\beta_L\overrightarrow{\Phi}_{\perp,\omega} + i\overrightarrow{\nabla}_\perp\Phi_{z,\omega}\right]. \tag{2.18}$$

Note that, in the derivation of eq. 2.18 $|\overrightarrow{\mathcal{P}}_{\omega NL}(\overrightarrow{\Phi}_\omega)|$, $|\overrightarrow{\delta\Phi}_\omega|$ and $\delta\beta_{NL}$ are assumed to be of order $\mathcal{O}(s)$, whereas their products and $|\overrightarrow{\mathcal{P}}_{\omega NL}(\overrightarrow{\delta\Phi}_\omega)| \sim \mathcal{O}(s^2)$ (*smallness*, s, is a dummy parameter $\ll 1$). $\hat{\mathcal{M}}$ is not hermitian, however its eigenvectors, $\overrightarrow{\Phi}_{\perp,\omega}$, still form a biorthonarmal basis $\overrightarrow{\Phi}^{\{j\}}_{\perp,\omega}$, i.e. $\int_S \overrightarrow{\Psi}^{i^*}_{\perp,\omega}\overrightarrow{\Phi}^{j}_{\perp,\omega} = \delta_{ij}$, being $\overrightarrow{\Psi}^{m}_{\perp,\omega}$ the eigenstates of $\hat{\mathcal{M}}^\dagger$ and δ_{ij} de Kronecker tensor [Silvestre98]. The perturbation field $\overrightarrow{\delta\Phi}_\omega$ can then be expanded in the basis $\overrightarrow{\Phi}^{\{m\}}_\omega$, which automatically yields to

$$\delta\beta_{NL} = \frac{k^2}{\epsilon_0}\frac{\int_S \overrightarrow{\Psi}^{m^*}_{\perp,\omega}\overrightarrow{\mathcal{P}}^{NL}_\omega(\overrightarrow{\Phi}^{(m)}_\omega)}{\int_S \overrightarrow{\Psi}^{m^*}_{\perp,\omega}\left[2\beta_L\overrightarrow{\Phi}^{m}_{\perp,\omega} + i\overrightarrow{\nabla}_\perp\Phi^m_{z,\omega}\right]}. \tag{2.19}$$

If one considers an infinite homogeneous and isotropic nonlinear medium, the induced change of the refractive index through the field intensity will affect to the propagation constant (effective wavelength) of the spatial mode. However, symmetry considerations show that there is no privileged point such that the light should focus to or defocus from. Hence, the spatial profile remains unchanged and the mode profiles differ from the linear ones only by the wavenumber shift eq. 2.19, but not in their actual distribution, so $\delta\Phi_\omega = 0$. This approximation will be used later on in this chapter, nevertheless one should bare in mind that this is approximately correct only for waveguides with core sizes well above the light wavelength.

2.2.1 Weak guidance

The term $\overrightarrow{\nabla}\left[\overrightarrow{\nabla}\overrightarrow{\mathcal{E}}_w\right]$ in eq. 2.7 yields to a diffraction mixing the Cartesian components of the electric field. Lack of well established and easy to implement numerical algorithms taking into account this coupling in the nonlinear regime, limits the validity of the standard pulse propagation equations in nonlinear media to systems in which neglecting this term in eq. 2.7 can be justified. It is common to argue that $\overrightarrow{\nabla}(\overrightarrow{\nabla}\overrightarrow{\mathcal{E}}) \approx 0$ because of $\overrightarrow{\nabla}\overrightarrow{\mathcal{D}} = 0$, what implies that the refractive index does not experience very sharp jumps at the interfaces. For this reason, such an approximation receives the name of weakly guiding approximation, what reduces eq. 2.7 to the form of the Helmholtz equation

$$\left(\partial_z^2 + \overrightarrow{\nabla}_\perp^2\right)\overrightarrow{\mathcal{E}}_w = -\mu_0\omega^2\overrightarrow{\mathcal{D}}_w. \tag{2.20}$$

Although the above is also called scalar approximation, note that the only strictly *scalar* field[3] in optics is the plane wave of the infinite homogeneous and isotropic space, so assuming a scalar field straight away in eq. 2.7 just leads to the plane wave equation. Hence, scalar approximation means only that this vectorial term is neglected but a little bit of the vectorial nature of the modal fields survives in the formalism, since the transverse derivatives in the term $\overrightarrow{\nabla}^2\overrightarrow{\mathcal{E}}$ do not cancel out. Regarding the electric field, this approximation is in fact a *slowly varying polarisation* (SVP) approximation.

[3]We point out that the usage of the extended terminology *scalar field* in optics is physically misleading. Even if the electric field remains linearly polarised, its vectorial nature yields to the well known boundary conditions at the interfaces between two different media, which are different than those of a truly scalar field.

2.3 Pulses in silica fibres

The time response function of fused bulk silica accounting for the Raman effect is introduced in the functional form $\mathcal{R} = R(t-t_1)\delta(t_1-t_2)\delta(t-t_3)$ [Agrawal07], where two out of the three time intervals associated to the interaction of four fields are assumed to be instantaneous, whereas only one of them may be delayed. With this, Fourier transform of eq. 2.12 reads

$$\mathcal{P}^{(NL)}_{x,\omega} = \epsilon_0 \int_{-\infty}^{\infty} \frac{d\omega_1 d\omega_2}{4\pi^2} \tilde{R}(\omega_1-\omega_2)\chi^{(3)}_{x;jkl}\mathcal{E}_{j,\omega_1}\mathcal{E}^*_{k,\omega_2}\mathcal{E}_{l,\omega-\omega_1+\omega_2}. \tag{2.21}$$

In order to obtain a propagation equation for the spectral envelope of the electric field, the following factorisation is proposed,

$$\overrightarrow{\mathcal{E}}_{\omega} = \overrightarrow{F}_{\omega}(x,y)\tilde{A}_{\omega-\omega_0}(z)e^{i\beta_0 z}, \tag{2.22}$$

where $\overrightarrow{F}(x,y)$ is assumed here to be proportional to the linear mode profile (see section 2.3.2), $\tilde{A}_{\omega-\omega_0}(z)$ the slowly varying spectral envelope, ω_0 the reference frequency and $\beta_0 \equiv \beta(\omega_0)$. The polarisation then becomes

$$\mathcal{P}^{(NL)}_{x,\omega} = \epsilon_0 \int_{-\infty}^{\infty} \frac{d\omega_1 d\omega_2}{4\pi^2} \tilde{R}(\omega_1-\omega_2)\left[\chi^{(3)}_{x;jkl}F_{j,\omega_1}F^*_{k,\omega_2}F_{l,\omega-\omega_1+\omega_2}\right] \times \tilde{A}_{\omega_1-\omega_0}\tilde{A}^*_{\omega_2-\omega_0}\tilde{A}_{\omega-\omega_1+\omega_2-\omega_0}. \tag{2.23}$$

At this point of the formalism, a major conceptual and delicate approximation is done. It consists in assuming that the spatial distributions $\overrightarrow{F}_{\omega_i}$ remain relatively similar to each other across all the spectrum and hence they can be taken outside from the integral by assuming $\overrightarrow{F}_{\omega_i} \to \overrightarrow{F}_{\omega}$. Using the properties in eqns. 2.9, the term in square brackets of eq. 2.23 is expressed as

$$\begin{aligned}
&\chi^{(3)}_{x;jkl}F_jF^*_kF_l = \\
&\chi^{(3)}_{xxxx}|F_x|^2F_x + (1-\delta_{xj})\left\{\left[\chi^{(3)}_{x;xjj}+\chi^{(3)}_{x;jjx}\right]|F_j|^2F_x + \chi^{(3)}_{x;jxj}F_j^2F_x^*\right\} = \\
&\chi^{(3)}(1-\delta_{xj})\left[|F_x|^2F_x + \frac{2}{3}|F_j|^2F_x + \frac{1}{3}F_j^2F_x^*\right] = \chi^{(3)}\frac{2}{3}\left[|\overrightarrow{F}|^2F_x + \frac{1}{2}\overrightarrow{F}^2F_x^*\right].
\end{aligned} \tag{2.24}$$

The approximation $\overrightarrow{F}_{\omega_i} \to \overrightarrow{F}_{\omega}$ could be subject of severe objections when working

with wide spectral distributions such that those in SC. However, a careful look reveals that this approximation is valid if the relevant nonlinear effects are due to waves that remain spectrally close to the reference (usually pump) frequency, ω_0. In this way, the error is introduced by the frequency detuning, $\omega - \omega_0$, of the fields involved in the nonlinear interaction. In practise, even in the case of SC generation, most of these effects happen inside the spectrum of a soliton, being then the biggest source of error for the assumption above, the Raman induced frequency down-shift towards the infra-red part of the spectrum.

Reproducing eqns. 2.23 and 2.24 for the components y and z the nonlinear polarisation reads

$$\overrightarrow{\mathcal{P}}_{\omega}^{(NL)} = \epsilon_0 \chi^{(3)} \frac{2}{3} \left[|\overrightarrow{F}|^2 \overrightarrow{F} + \frac{1}{2} \overrightarrow{F}^2 \overrightarrow{F}^* \right] \int_{-\infty}^{\infty} \frac{d\omega_1 d\omega_2}{4\pi^2} \tilde{R}(\omega_1 - \omega_2) \times \tilde{A}_{\omega_1 - \omega_0} \tilde{A}^*_{\omega_2 - \omega_0} \tilde{A}_{\omega - \omega_1 + \omega_2 - \omega_0}, \tag{2.25}$$

and inserting it into the wave equation eq. 2.7, together with the factorisation 2.22 and applying the operator $\int_S \overrightarrow{F}^*_{\omega} \circ$ we get

$$\begin{aligned} &\int_S |\overrightarrow{F}_{\perp,\omega}|^2 \partial_z^2 \tilde{A} + \left\{ 2i\beta_0 \int_S |\overrightarrow{F}_{\perp,\omega}|^2 - \int_S \overrightarrow{F}^*_{\omega} \left[\overrightarrow{\nabla}_{\perp} F_z + \hat{z} \overrightarrow{\nabla}_{\perp} \overrightarrow{F}_{\perp,\omega} \right] \right\} \partial_z \tilde{A} = \\ &\left\{ \left(\beta_0^2 - \beta^2 \right) \int_S |\overrightarrow{F}_{\perp,\omega}|^2 + i[\beta_0 - \beta] \int_S \overrightarrow{F}^*_{\omega} \left[\overrightarrow{\nabla}_{\perp} F_z + \hat{z} \overrightarrow{\nabla}_{\perp} \overrightarrow{F}_{\perp,\omega} \right] \right\} \tilde{A} \\ &-\frac{2}{3} k^2 \chi^{(3)} \int_S \left[|\overrightarrow{F}_{\omega}|^4 + \frac{1}{2} |\overrightarrow{F}^2_{\omega}|^2 \right] \times \\ &\int_{-\infty}^{\infty} \frac{d\omega_1 d\omega_2}{4\pi^2} \tilde{R}(\omega_1 - \omega_2) \tilde{A}_{\omega_1 - \omega_0} \tilde{A}^*_{\omega_2 - \omega_0} \tilde{A}_{\omega - \omega_1 + \omega_2 - \omega_0}, \end{aligned} \tag{2.26}$$

where the linear eqns. 2.13 and 2.14 have been used to introduce the terms $\sim \beta, \beta^2$. When the waveguides cross sections are big enough, it is usually the case that $|F_z| << |F_{\perp}|$, so $\int_S |\overrightarrow{F}_{\perp,\omega}|^2 \approx \int_S |\overrightarrow{F}_{\omega}|^2$. Neglecting also the counter propagating beam, via the paraxial approximation $\partial_z^2 \tilde{A} \to 0$, eq. 2.26 is rewritten as

$$\partial_z \tilde{A} = -\frac{\left[\beta^2 - \beta_0^2\right] \int_S |\overrightarrow{F}_\omega|^2 + i[\beta - \beta_0] \int_S \overrightarrow{F}_\omega^* \left[\overrightarrow{\nabla}_\perp F_z + \hat{z}\overrightarrow{\nabla}_\perp \overrightarrow{F}_{\perp,\omega}\right]}{2i\beta_0 \int_S |\overrightarrow{F}_\omega|^2 - \int_S \overrightarrow{F}_\omega^* \left[\overrightarrow{\nabla}_\perp F_z + \hat{z}\overrightarrow{\nabla}_\perp \overrightarrow{F}_{\perp,\omega}\right]} \tilde{A} + i\gamma\mathcal{I} \tag{2.27}$$

$$\gamma \equiv \frac{2}{3}k^2\chi^{(3)} \frac{\int_S \left[|\overrightarrow{F}_\omega|^4 + \frac{1}{2}|\overrightarrow{F}_\omega^2|^2\right]}{2\beta_0 \int_S |\overrightarrow{F}_\omega|^2 - \int_S \overrightarrow{F}_\omega^* \left[\overrightarrow{\nabla}_\perp F_z + \hat{z}\overrightarrow{\nabla}_\perp \overrightarrow{F}_{\perp,\omega}\right]} \tag{2.28}$$

$$\mathcal{I} \equiv \int_{-\infty}^{\infty} \frac{d\omega_1 d\omega_2}{4\pi^2} \tilde{R}(\omega_1 - \omega_2) \times \tilde{A}_{\omega_1-\omega_0} \tilde{A}^*_{\omega_2-\omega_0} \tilde{A}_{\omega-\omega_1+\omega_2-\omega_0}. \tag{2.29}$$

Eq. 2.27 describes the nonlinear propagation of the slowly varying spectral envelope of the electric field in a waveguide with an arbitrary cross section (uniform along z), made of an amorphous material or cubic crystal. This equation could be solved numerically using well known algorithms, however it is presented in the literature (see e.g. [Agrawal07]) with two further simplifications. First, the spectrum is assumed to be such that the dependence of β with ω lets approximate $\beta^2 - \beta_0^2 \approx 2\beta_0\Delta\beta$, where $\beta = \beta_0 + \Delta\beta$, $\Delta\beta \equiv \sum_{m=1}^{\infty} \beta_m \left[\omega - \omega_0\right]^m / m!$ and $\beta_m \equiv \partial_\omega^m \beta(\omega)|_{\omega_0}$ are the so called *dispersion coefficients*. Second, the spatial modes are assumed to be slowly varying functions in the sense that $|\overrightarrow{\nabla}_\perp \overrightarrow{F}_\omega| << |\overrightarrow{F}_\omega|$, what is equivalent to the weakly guiding approximation (see section 2.2.1) and hence the terms $\sim \overrightarrow{\nabla}_\perp$ are disregarded[4]. With this, the generalised nonlinear Schrödinger equation (GNLSE) is recovered,

$$\partial_z \tilde{A} = i\Delta\beta\tilde{A} - \gamma\mathcal{I} \tag{2.30}$$

$$\gamma \approx \frac{k^2}{\beta_0}\frac{\chi^{(3)}}{2} \frac{\int_S \frac{2}{3}\left[|\overrightarrow{F}_\omega|^4 + \frac{1}{2}|\overrightarrow{F}_\omega^2|^2\right]}{\int_S |\overrightarrow{F}_\omega|^2}. \tag{2.31}$$

Applying the inverse Fourier transform, using $\hat{\mathcal{F}}^{-1}\left((\omega - \omega_0)^m \tilde{\Psi}_{\omega-\omega_0}\right) = (i\partial_t)^m \Psi(t,z)$, Ψ playing the role of $\tilde{A}$ and $\mathcal{I}$, the time domain representation of eq. 2.30 is

[4]Note the smallness of the terms $\sim \overrightarrow{\nabla}_\perp F_z$ at the subwavelength scale is not guaranted.

$$\partial_z A(z,T) = i\sum_{m=2}^{\infty}\frac{\beta_m}{m!}(i\partial_T)^m A(z,T) + i\gamma_0\left[1 + i\frac{\gamma_1}{\gamma_0}\partial_T + \sum_{m=2}^{\infty}\frac{\gamma_m}{\gamma_0}(i\partial_T)^m\right]\times$$
$$A(z,T)\int_{-\infty}^{\infty} T_1 R(T_1)|A(z,T-T_1)|^2, \tag{2.32}$$

where the change of variable $T \equiv \left[t - \frac{z}{V_g}\right]$ has been introduced to remove the first order time derivative from the linear operator, which is a velocity term with no physical influence for uniform fibres (constant cross section along z). Hence, T represents the time measured in the reference frame co-moving with $A(z=0,t)$ at its physical group velocity $V_g = 1/\beta_1$ in the lab frame. $\gamma_m \equiv \partial_T^m \gamma|_{\omega_0}$ and the terms with $m \geq 1$ account for the *nonlinear dispersion*. The most commonly used of these terms is the first order one, responsible for the optical *shock* waves developed over the characteristic time scale $\tau_{shock} \equiv \gamma_1/\gamma_0$. The response function of fussed silica glass was experimentally measured by [Stolen89] and introduced in the analytical form [Blow89]

$$R(t) = (1-f_R)\delta(t) + f_R h_R(t)$$
$$h_R(t) := \Theta(t)\frac{\tau_1^2+\tau_2^2}{\tau_1\tau_2^2}e^{-\frac{t}{\tau_2}}\sin\frac{t}{\tau_1}, \tag{2.33}$$

where the Dirac delta function $\delta(t)$ accounts for the electronic transitions and $h_R(t) \equiv \frac{\tau_1^2+\tau_2^2}{\tau_1\tau_2^2}\Theta(t)e^{-t/\tau_2}\sin(t/\tau_1)$ for the excited molecular vibration, which period and lifetime are given by $\tau_1 = 12.2$sf and $\tau_2 = 32$sf, respectively. The ratio between the two nonlinear interactions in $R(t)$ is given by the so called Raman fraction, $f_R \equiv 0.18$, and $\Theta(t)$ is the Heaviside step function, important to restore causality in the integral of eq. 2.32.

2.3.1 Temporal solitons and the NLS equation

When the pulse spectrum is narrow enough, all the higher order terms in the linear and nonlinear expansions of eq. 2.32 can be disregarded. Also, the associated wide temporal profile reduces Raman to an instantaneous effect, i.e., $h_R(t) \to \delta(t)$ and eq. 2.32 reduces to the well known NLS equation (NLSE),

$$\partial_A(z,T) = i\frac{\beta_2}{2}(i\partial_T)^2 A(z,T) + i\gamma|A(z,T)|^2 A(z,T), \tag{2.34}$$

where $\gamma \equiv \gamma_0$ and so will be assumed from now on. Temporal solitons in optical

fibres are known to exist in the frame of the NLSE for both focusing and defocusing nonlinear media [Hasegawa73b, Hasegawa73a]. They propagate with undistorted intensity and spectrum profiles because of the linear dispersion cancellation resulting from the interplay of the lowest order linear (GVD) and nonlinear (Kerr) effects. In the focusing case ($\gamma/\beta_2 > 0$) the lowest order (fundamental) solitons are the well known bright solitons [Hasegawa73b], which are unchirped, or transform limited, localised pulses

$$A_{bs}(z,t) = \sqrt{P_0} Sech\left(t\sqrt{\frac{\gamma P_0}{-\beta_2}}\right) e^{i\frac{\gamma P_0}{2}z}, \tag{2.35}$$

where $\sqrt{-\beta_2/\gamma P_0}$ is the temporal width T_0 and is related to the intensity *full width at half maximum* by $FWHM = 2\ln(1+\sqrt{2})T_0$. By increasing the soliton amplitude $\sqrt{P_0}$ by an integer factor N, eq. 2.35 describes an $N-th$ order soliton in its unchirped state, which temporal and spectral evolutions are periodic in z.

In the defocusing case ($\gamma/\beta_2 < 0$), the undistorted propagation happens for the also well known dark solitons [Hasegawa73a], which turn out to be a lower intensity dip laying on a chirped non localised background

$$\begin{aligned} A_{ds}(z,t) &= \sqrt{P_0}\left[\cos\phi\tanh\Theta - i\sin\phi\right] e^{i\gamma P_0 z}, \\ \Theta &\equiv \sqrt{\frac{\gamma P_0}{\beta_2}}\cos\phi\left[t - \sqrt{\gamma P_0\beta_2}\sin\phi z\right],\ \phi\in[-\pi/2,\pi/2]. \end{aligned} \tag{2.36}$$

In this case, the width of the soliton dip is $T_0 \equiv \sqrt{\frac{\beta_2}{\gamma P_0}}/\cos\phi$, which depends on the *greyness* phase, ϕ. T_0 takes the minimum value for the so called *black* soliton ($\phi = 0$), for which the intensity falls to zero at the centre of the dip, and it becomes infinite for the continuous wave limits $\phi \to \pm\pi/2$. Solitons with $0 < |\phi| < \pi/2$ are referred to as *grey* solitons.

2.3.2 A note on dimensions

In the context of temporal optics it is useful that $|A(z,t)|^2$ has the meaning of total amount of energy that flows through the fibre cross section per time unit. For that the dimensions of A are $[A(z,t)] = W^{1/2}$ and the function $\overrightarrow{F}_w$ is related to the linear fibre modes $\overrightarrow{\Phi}_w$ by

$$\overrightarrow{F}_w(x,y) \equiv \frac{\overrightarrow{\Phi}_w(x,y)}{P^{1/2}},\ P \equiv \frac{1}{2}\int_S \mathrm{Re}\left(\overrightarrow{\Phi}_w \times \overrightarrow{\mathcal{H}^*}_w\right)\hat{u}_z, \tag{2.37}$$

where P is the guided power, $\hat{u}_z$ is the unitary vector along the z-axis and hence the units $\left[\overrightarrow{\Phi}_w\right]$ =V/m. Taking into account that $P = \int_s I$, where the intensity $I \equiv \sqrt{\epsilon_L}\epsilon_0 c|\overrightarrow{\Phi}|^2/2$, and using $\beta \approx k\epsilon_L$, the nonlinear coefficient derived in eq. 2.31 reads in the recently developed and experimentally confirmed form [Shahraam Afshar09] (see eq. 2.54 for $\chi^{(3)}$)

$$\gamma \approx \omega\epsilon_0\chi^{(3)} \frac{\int_S \frac{2}{3}\left[|\overrightarrow{\Phi}_\omega|^4 + \frac{1}{2}|\overrightarrow{\Phi}^2_\omega|^2\right]}{\left[\int_S \mathrm{Re}\left(\overrightarrow{\Phi}_w \times \overrightarrow{\mathcal{H}^*}_w\right)\hat{u}_z\right]^2}. \tag{2.38}$$

Note that in this situation, P_0 in eqns. 2.35 and 2.36 has the meaning of peak and background power, respectively.

The propagation equation eq. 2.32 is many times normalised to the characteristic time, length and power scales in the sense that the substitutions $A \to A\sqrt{P_0}/N$, $z \to z/L_D$ and $T \to T/T_0$ have to be done in eq. 2.32, leading to

$$\partial_z A(z,T) = i\sum_{m=2}^{M} \frac{\beta_m}{T_0^{m-2}|\beta_2|m!}(i\partial_T)^m A(z,T) + i\left[1 + i\tau_{shock}\partial_T\right] \times$$
$$A(z,T)\int_{-\infty}^{\infty} dT_1 \mathcal{R}(T_1)|A(z,T-T_1)|^2, \tag{2.39}$$

where the shock and Raman time scales have also changed to $\tau_i \to \tau_i/T_0$, $L_D \equiv \frac{T_0^2}{|\beta_2|}$ is the so called dispersion length and M is the linear dispersion truncation order.

2.3.3 Lagrangian formalism

The action associated to the equation of motion eq. 2.39 must be of the form $S(\Psi, \partial_z\Psi, \partial_t^m\Psi)$, with $m : 1 \to M$ and $\Psi = A, A^*$. Hence, Euler-Lagrange equation is given in the form [Riley06]

$$\frac{\partial\mathcal{L}}{\partial\Psi} - \partial_z\frac{\partial\mathcal{L}}{\partial(\partial_z\Psi)} + \sum_{m=1}^{M}(-)^m\partial_t^m\frac{\partial\mathcal{L}}{\partial(\partial_t^m\Psi)} \equiv 0, \tag{2.40}$$

where the $\partial_t^m\Psi$ with $m : 0 \to M-1$ have prescribed values at $t \to \pm\infty$ [Courant66]. This formulation of the Lagrangian dynamics does not allow to construct an $\mathcal{L}$ such that eq. 2.40 reproduces simultaneously the equations for A and A^* with non conservative terms. This prevents the Raman interaction term from being accounted for in $\mathcal{L}$. Interestingly, the shock term in eq. 2.39 $\sim \partial_t(|\Psi|^2\Psi)$ can only be reproduced by eq. 2.40 accompanied by the terms $2|\Psi|^2\partial_t\Psi - \Psi^2\partial_t\Psi^*$. This yields to the Lagrangian

density

$$\mathcal{L} = \frac{i}{2}\left[A\partial_z A^* - A^*\partial_z A\right] - \frac{1}{2}\sum_{m\geq 2} c_m\left[A^*\partial_t^m A + (-)^m A\partial_t^m A^*\right] -$$
$$-\frac{1}{2}(1-f_R)|A|^4 + (1-\delta_{ds})(1-f_R)\frac{i}{\omega_0}|A|^2\left[A\partial_t A^* - A^*\partial_t A\right] \tag{2.41}$$

that in conjunction with eq. 2.40 gives the equation of motion

$$-i\partial_z A = \sum_{m=2}^{\infty} c_m\partial_t^m A + (1-f_R)|A|^2 A +$$
$$+(1-f_R)\frac{i}{\omega_0}\left\{\partial_t(|A|^2A) + (1-\delta_{ds})[4|A|^2\partial_t A - \partial_t(|A|^2A)]\right\}, \tag{2.42}$$

where $c_m \equiv \frac{i^m\beta_m}{T_0^{m-2}|\beta_2|m!}$. δ_{ds} is introduced to include the self-steepening term in the dissipative ($\delta_{ds}=1$) and conservative ($\delta_{ds}=0$) versions (subscript ds stands for "dissipative self-steepening"). In conventional pulse propagation equations $\delta_{ds}=1$ (see e.g. [Anderson83]). However optical shock waves have been experimentally proved to preserve energy along propagation [Wan07], suggesting $\delta_{ds}=0$, since they only exchange energy when overcoming other slower waves in the system. Because clarifying such an apparent discrepancy is beyond the scope of this thesis, both possibilities are accounted for. Speculatively, a possible common point between the two perspectives above could be find by noting that the conservative shock term reproduced by the Lagrangian of eq. 2.41 is the non-conservative one plus perturbations in the form of time derivatives of A, which are smoother than the derivatives of A^3,

$$4|A|^2A\partial_t A = \partial_t(|A|^2A) + 2|A|^2\partial_t A - A^2\partial_t A^* \approx \partial_t(|A|^2A) + \mathcal{O}(\partial_t A^1). \tag{2.43}$$

The Hamiltonian density of the system is readily obtained in the form

$$\mathcal{H} \equiv \pi\partial_z A + \pi^\dagger\partial_z A^* - \mathcal{L} = \frac{1}{2}\sum_{m\geq 2} c_m\left[A^*\partial_t^m A + (-)^m A\partial_t^m A^*\right] +$$
$$+\frac{1}{2}(1-f_R)|A|^4 + (1-\delta_{ds})(1-f_R)\frac{i}{\omega_0}|A|^2\left[A^*\partial_t A - A\partial_t A^*\right] \tag{2.44}$$
$$\pi \equiv \frac{\partial\mathcal{L}}{\partial(\partial_z A)} = -\frac{i}{2}A^*, \pi^\dagger \equiv \frac{\partial\mathcal{L}}{\partial(\partial_z A^*)} = \frac{i}{2}A. \tag{2.45}$$

Non-conservative dynamics associated to the propagation eq. 2.39 will introduce a Hamiltonian density variation along z. This can be calculated explicitly by substituting the equation of motion eq. 2.39 and its complex conjugate in the z-derivative of the Hamiltonian eq. 2.45, what leads to

$$\begin{aligned}\partial_z\mathcal{H} = &-\langle R_d \mid ic_m\partial_t^m\hat{\sigma_1} \mid R_d\rangle - \langle R_k \mid \hat{\sigma}_1 \mid R_k\rangle - \\ &-(1-\delta_{ds})\langle R_s \mid \hat{\sigma_1} \mid R_s\rangle - \delta_{ds}2\langle S_d \mid ic_m\partial_t^m\hat{\sigma_1} \mid S_d\rangle\end{aligned} \tag{2.46}$$

with

$$\mid R_d\rangle \equiv \begin{bmatrix} f_R[1+\frac{i}{\omega_0}\partial_t](AI) \\ \\ A \end{bmatrix} \tag{2.47}$$

$$\mid R_k\rangle \equiv \begin{bmatrix} f_R[1+\frac{i}{\omega_0}\partial_t]AI \\ \\ (1-f_R)|A|^2A \end{bmatrix} \tag{2.48}$$

$$\mid R_s\rangle \equiv \begin{bmatrix} f_R[1+\frac{i}{\omega_0}\partial_t](AI) \\ \\ (1-f_R)\frac{4i}{\omega_0}|A|^2\partial_t A \end{bmatrix} \tag{2.49}$$

$$\mid S_d\rangle \equiv \begin{bmatrix} (1-f_R)\frac{i}{\omega_0}\partial_t(|A|^2A) \\ \\ A \end{bmatrix} \tag{2.50}$$

$$\hat{\sigma}_1 \equiv \begin{bmatrix} 0 & 1 \\ 1 & 0 \end{bmatrix}, \quad I \equiv \int_{-\infty}^{\infty} dt' h_R(t') \left|A(t-t')\right|^2. \tag{2.51}$$

Eq.2.46 clearly shows the sources of dissipation in this effective model in the form of expected values of the operators $ic_m\partial_t^m\hat{\sigma_1}$ and $\hat{\sigma_1}$. The former gives the loss due to the interaction of a linear and a nonlinear effect and the latter due to two nonlinear effects. Raman effect is dissipative because of the presence of all the conservative terms, i.e., dispersion, Kerr and self-steepening with $\delta_{ds} = 0$ as one can see in the non vanishing expected values involving $\mid R_d\rangle$, $\mid R_k\rangle$ and $\mid R_s\rangle$, respectively. On the other hand, the non-conservative self-steepening term is so only because of the presence of linear dispersion, otherwise the expected value involving $\mid S_d\rangle$ vanishes. In practise, fibres are always dispersive and the Raman effect does not appear without Kerr. The actual value of δ_{ds} would determine whether $\mid R_s\rangle$ or $\mid S_d\rangle$ have to be considered or

not.

Appart from physical insight and motivation for further studies on shock waves, equations 2.46-2.51 provide a useful semi analytical test for convergence in numerical simulations. By computing at each step $H \equiv \int_{-\infty}^{-\infty} dt\mathcal{H}(t)$ the variation of the Hamiltonian along z, $\Delta_z H = (H^{(i)} - H^{(i-1)})/\delta z$, can be compared with the explicit variation eq. 2.46, evaluated with the instantaneous numerically computed fields.

2.4 Continuous wave beams

When the nonlinear interactions are considered for monochromatic fields and frequency conversion effects can be disregarded, the temporal response function becomes instantaneous (local in time) $\mathcal{R}(t,t_1,t_2,t_3) \propto \delta(t-t_1)\delta(t-t_2)\delta(t-t_3)$ [Agrawal07]. With this, eqns .2.9 and 2.12 give a nonlinear polarisation

$$\mathcal{P}^{NL}_{x,\omega} = \epsilon_0\chi^{(3)}\left\{|\mathcal{E}_{x,\omega}|^2\mathcal{E}_{x,\omega} + \frac{2}{3}|\mathcal{E}_{j,\omega}|^2\mathcal{E}_{x,\omega} + \frac{1}{3}\mathcal{E}^2_{j,\omega}\mathcal{E}^*_{x,\omega}\right\} = \epsilon_0\chi^{(3)}\frac{1}{3}\left\{2|\overrightarrow{\mathcal{E}}_\omega|^2\mathcal{E}_{x,\omega} + \overrightarrow{\mathcal{E}}^2_\omega\mathcal{E}^*_{x,\omega}\right\}, \tag{2.52}$$

which is equivalent to the substitution $\tilde{R}(\omega_1-\omega_2) \rightarrow 4\pi^2\delta(\omega-\omega_1)\delta(\omega-\omega_2)$ in eq. 2.21 and then dielectric constant matrix introduced in the constitutive relation eq. 2.5 read as

$$\epsilon_{kl} = \left[\epsilon_L + \frac{2}{3}\chi^{(3)}|\vec{\mathcal{E}}_\omega|^2\right]\delta_{kl} + \frac{\chi^{(3)}}{3}\mathcal{E}^*_k\mathcal{E}_l. \tag{2.53}$$

The nonlinear change of the refractive is assumed to be $\delta n_{NL} \equiv n_2 I$, where $I = \sqrt{\epsilon_L}\epsilon_0 c|\vec{\mathcal{E}}|^2/2$ is the intensity of the light and n_2 the so called nonlinar index. If $\delta n_{NL} << \sqrt{\epsilon_L}$ and we think of real fields in eq. 2.53, then

$$\chi^{(3)} = \epsilon_L\epsilon_0 c n_2. \tag{2.54}$$

Note that the Maxwell equations we started from, eqns. 2.1-2.4, assume the Fourier transform of the fields gives real quantities in time domain. Other approaches [Agrawal07] assume these quantities complex, and as a result the nonlinear susceptibility, $\chi^{(3)}$, is obtained scaled by a different factor (RHS of eq. 2.54 appears multiplied by 4/3).

2.4.1 Waveguide arrays: discrete NLS equation

In this section we introduce the coupled nonlinear equations used to study monochromatic fields in arrays of waveguides. These equations are used straight away in chapter 5 and generalised in chapter 6 to study the spatial coupling between solitons and plasmons.

The ansatz for the electric field is taken in the form

$$\overrightarrow{\mathcal{E}}_{\omega} = \sum_{n} \overrightarrow{F}_n(x,y)\tilde{A}_n(\omega,z)e^{i\beta z}, \tag{2.55}$$

where the subscript n refers to the nth core of the array, β_n is the propagation constant of its mode and β the the one of the whole array mode or supermode. Repeating the process that led to eqns. 2.30 and 2.31 (assuming therefor that β_n, β correspond to linear modes), but using instead the nonlinear polarisation eq. 2.52, one gets

$$\begin{aligned} 2i\beta\partial_z\left(\sum_n \tilde{A}_n \int_S \overrightarrow{F}^*_q \overrightarrow{F}_n\right) &= \sum_n \left[\beta^2-\beta_n^2\right]\tilde{A}_n \int_S \overrightarrow{F}^*_q \overrightarrow{F}_n - \\ -\frac{2}{3}k^2\chi^{(3)} \sum_{m,n,p} \int_S \Big\{ &\left[\overrightarrow{F}^*_m \overrightarrow{F}_n\right]\left[\overrightarrow{F}^*_q \overrightarrow{F}_p\right]\tilde{A}^*_m\tilde{A}_n\tilde{A}_p + \\ +\frac{1}{2}&\left[\overrightarrow{F}_m \overrightarrow{F}_n\right]\left[\overrightarrow{F}^*_q \overrightarrow{F}^*_p\right]\tilde{A}_m\tilde{A}_n\tilde{A}^*_p\Big\}. \end{aligned} \tag{2.56}$$

Assuming the separation between the waveguides yields to a *small* overlap between the modal distributions of neighbouring cores,

$$\int_S \overrightarrow{F}^*_i \overrightarrow{F}_j \approx \sum_{k=-\infty}^{\infty} \epsilon^{|k|}\delta_{i,j+k};\ |\epsilon| \ll 1 \tag{2.57}$$

eq. 2.56 can be rewritten as

$$\begin{aligned} \partial_z\tilde{A}_n = &-\frac{i}{2\beta}\left[\beta^2-\beta_n^2\right]\tilde{A}_n - i\sum_{j=1}^{\infty}\kappa^{(j)}\left[\tilde{A}_{n-j}+\tilde{A}_{n+j}\right] + i\gamma|\tilde{A}_n|^2\tilde{A}_n \\ &+i\gamma_s|\tilde{A}_n|^2\left[\tilde{A}_{n-1}+\tilde{A}_{n+1}\right] + i\frac{\gamma_v}{2}\tilde{A}_n^2\left[\tilde{A}^*_{n-1}+\tilde{A}^*_{n+1}\right] \end{aligned} \tag{2.58}$$

where

$$\kappa^{(j)} \equiv \frac{\left[\beta^2 - \beta_{n\pm j}^2\right]}{2\beta} \int_S \overrightarrow{F}_n^* \overrightarrow{F}_{n\pm j} \tag{2.59}$$

$$\gamma \equiv \frac{k^2\chi^{(3)}}{3\beta} \int_S \left[|\overrightarrow{F}_n|^4 + \frac{1}{2}|\overrightarrow{F}_n^2|^2 \right] \tag{2.60}$$

$$\gamma_s \equiv \frac{k^2\chi^{(3)}}{3\beta} \int_S |\overrightarrow{F}_n|^2 \overrightarrow{F}_n^* \overrightarrow{F}_{n+1} \tag{2.61}$$

$$\gamma_v \equiv \frac{k^2\chi^{(3)}}{3\beta} \int_S \overrightarrow{F}_n^2 \overrightarrow{F}_n^* \overrightarrow{F}_{n+1}. \tag{2.62}$$

If only nearest neighbour linear interaction is considered ($\kappa^{(j)} = 0, \forall j > 1$) and cross phase modulation (XPM) between the different waveguides is neglected ($\gamma_{v,s} = 0$), eq. 2.58 simplifies to

$$i\partial_z A_n = \kappa \left[A_{n-1} + A_{n+1}\right] + \gamma |A_n|^2 A_n \; n \in [1, N], \tag{2.63}$$

where $\kappa \equiv \kappa^{(1)}$ is the coupling constant of the N identical waveguides array and $A_n(z) \equiv \tilde{A}_n(z) exp(iz[\beta^2 - \beta_n^2]/[2\beta])$. This equation was first proposed by [Christodoulides88] and called the *discrete nonlinear Schrödinger* (DNLS) equation, because of its obvious similarity with eq. 2.34. The array is made planar (in chapter 5) by imposing the boundary conditions $A_n \equiv 0 \; \forall \; n \notin [1, N]$.

Note that, for non-identical cores $k^{(j)} \rightarrow k_n^{(j)}$, so there is no well defined coupling constant for the system, but the equations up to eq. 2.62 would still hold. However, when some of the considered modes is nonlinear, e.g., a spatial soliton (as in chapter 6), not even eq. 2.56 is valid, and the simple coupled equations are derived in a slightly different way.

Chapter 3

Continuum generation by dark solitons in optical fibres

This chapter explores the generation of continuum spectra seeded from dark solitons in fibres. The key ingredient is the resonant Cherenkov radiation emitted by several solitons, with different carrier frequencies, across the zero GVD frequency. The Raman effect, always present in silica fibres, turns out to play a key role in the radiation amplitude, enhancing or suppressing it depending on the fibre dispersion profile. The chapter is structured as follows. Section 3.1 introduces the dark solitons perturbed by the presence of a zero GVD frequency. Then, the resonance condition for the perturbed dark solitons is derived analytically in section 3.2, proving perfect match with numerical simulations. Calculation of the resonant radiation (RR) amplitude is the subject of section 3.3 and the influence of Raman effect in its strength is discussed only numerically. Raman nonlinearity was not taken into account for the derivation of the resonance condition, since the modelling did not show that this effect produced a substantial change in the RR frequency. Finally, the realistic continuum excitation by a dark soliton train is considered in section 3.4.

3.1 Perturbation of solitons and Galilean transformation

To study the Cherenkov radiation emitted from a soliton, it is enough to assume the propagation of the dimensionless electric field envelope, $A(z,t)$, is given by (simplified form of eq. 2.39)

$$-i\partial_z A + \frac{1}{2}\partial_t^2 A - |A|^2 A = -i\epsilon\partial_t^3 A, \tag{3.1}$$

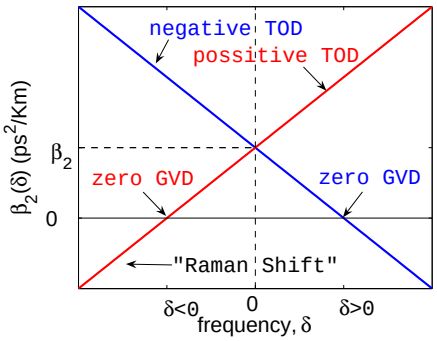

Figure 3.1: Dispersion profile introduced by the third order dispersion for positive (red) and negative (blue) ϵ. Horizontal dashed line marks the GVD coefficient, β_2, at the reference frequency ω_0.

where the perturbation to the NLSE in the right hand side accounts for the *Third Order Dispersion* (TOD), which is controlled here by the coefficient $\epsilon \equiv \frac{\beta_3}{6T_0|\beta_2|}$ and its main effect is to introduce a zero GVD frequency, as shown in fig. 3.1. The dispersion coefficients, $\beta_{2,3}$, are evaluated at the reference frequency, ω_0.

It is important to note that the solitons of the NLSE ($\epsilon = 0$ in eq. 3.1) given as a function of t and z, $F(z,t) \equiv A_{soliton}$, are at rest in the reference frame defined by $t \equiv \frac{1}{T_0}\left[T - \frac{z}{V_g}\right]$ (see section 2.3.1) because the variables (t,z) are treated independently or, what is the same, the soliton group velocity V_g is a constant parameter. Hence, this frame is rigid and it does not stay stationary with a soliton which parameters change during the propagation, what is expected due to various nonlinear effects associated with the RR, and so it turns out to be an inconvenient frame to work with when studying perturbation effects. When perturbations are small ($|\epsilon| << 1$), a shift in the soliton carrier frequency induces a shift in the wave number and group velocity, but $F(z,t)$ does not lose its solitonic behaviour. Assuming the soliton depth does not change, all the soliton parameters can be expressed as a function of the soliton frequency, so it can be the only variable to think of when considering the perturbed soliton evolution. We can dote our frame with some flexibility if we replace the set of variables (t,z) by (ξ,z), using the change of variable $\xi \equiv t - \alpha z$, where $\alpha \in \mathbb{R}$ is the free parameter. This is the so called Galilean transformation, which allows a reference frame linear velocity shift from V_g, to match the group velocity of the soliton with varying parameters. The discussion above motivates the ansatz to solve eq. 3.1 in the form

$$A(z,t) = \{F(\xi,z) + g(\xi,z)\}\, e^{ikz - i\delta_s t}, \tag{3.2}$$

where $F(\xi,z)$ is the soliton envelope, $g(\xi,z)$ the perturbation field, $\delta_s \equiv (\omega_s - \omega_0)T_0$ the soliton frequency shift from ω_0, and $k(\delta_s, |F(\xi,z)|) \equiv D_s(\delta_s) + q(|F|)$ the associated wave number shift. D_s accounts for the linear shift from β_0 due to δ_s, and q for the nonlinear contribution due to the soliton background power.

Substituting the ansatz eq. 3.2 into eq. 3.1 and assuming that $F(\xi,z)$ remains soliton despite the presence of TOD (equivalent to assume that the effect of the perturbation field $g(\xi,z)$ is to balance the distortion that the TOD would introduce in the soliton), yields to the equation of motion for the field $F(\xi,z)$

$$\partial_z F + i\frac{d}{2}\partial_\xi^2 F + iqF = i\,|F|^2\, F, \tag{3.3}$$

where $d \equiv 1 + 6\epsilon\delta_s$ is the GVD coefficient, and also gives the explicit expressions for the linear wave number and group velocity shifts,

$$D_s = \frac{1}{2}\delta_s^2 + \epsilon\delta_s^3 \tag{3.4}$$

$$\alpha = \delta_s + 3\epsilon\delta_s^2 = D_s^{'}. \tag{3.5}$$

The latter ones are consistent with the requirements made before ($D_s, \alpha = 0$ when $\delta_s = 0$) and are actually a consequence of the quasi-Galilean invariance of eq. 3.1, which if $\epsilon = 0$ takes the usual form, $D_s = \frac{\alpha^2}{2}$ and $\alpha = \delta_s$. Eq.3.3 is the NLSE[1] in a more general way than eq. 3.1, since it accounts for the soliton parameters shift due to the presence of the perturbation. The well known dark soliton solution of eq. 3.3 requires $d > 0$, so δ_s belongs to the normal GVD regime, and is given by [Kivshar97]

$$F = \sqrt{q}\,[\cos\phi \tanh\Theta - i\sin\phi] \tag{3.6}$$

$$\Theta \equiv \tau\cos\phi\sqrt{\frac{q}{d}}, \tau \equiv \xi - \sin\phi\sqrt{qd}z, \tag{3.7}$$

being $\phi \in [-\pi/2, \pi/2]$ the greyness parameter and $F(\phi)^* \equiv F(-\phi)$. The variable $\tau \equiv \xi - \sin\phi\sqrt{qd}z$ is now introduced to keep grey solitons at rest in our reference frame, since their velocities are also ϕ dependent.

The assumptions yielding to eq. 3.3 also give the linearised equation for the perturbation g, which is coupled with its conjugate complex g^*, and in the reference

[1]Note the change $F \to Fe^{-iqz}$, $q \neq q(z)$ removes the phase term from eq. 3.3, recovering the usual NLSE form.

frame defined by τ reads as

$$\partial_z |g\rangle + i\hat{L} |g\rangle + \mathcal{O}(\epsilon^2) = \epsilon\partial_\tau^3 |F\rangle , \tag{3.8}$$

where

$$\hat{L} \equiv \begin{bmatrix} \hat{W} & -F^2 \\ F^{*2} & -\hat{W}^* \end{bmatrix}, \tag{3.9}$$

$$\hat{W} \equiv i\epsilon\partial_\tau^3 + \frac{d}{2}\partial_\tau^2 + i\sin\phi\sqrt{qd}\partial_\tau + q - 2|F|^2 \tag{3.10}$$

and

$$|\Psi\rangle \equiv \begin{bmatrix} \Psi \\ \Psi^* \end{bmatrix} \leftrightarrow \Psi = F, g. \tag{3.11}$$

The calculation of the Cherenkov radiation frequency and amplitude is done from equation 3.8 in the next two sections.

3.2 Radiation frequency: resonance condition

To find the resonant radiation frequency, δ, from eq. 3.8 we need an ansatz for $g(\tau, z)$. The fact that it is treated as a small perturbation yields to our linearised model, in which several hypo-thetic perturbations with different frequencies would not interact to each other and would satisfy eq. 3.8 separately. For that, it is enough to consider, in the zero order approximation, the CW solution

$$|g\rangle = \begin{bmatrix} C_1 \\ {C_2}^* \end{bmatrix} e^{i\Omega\tau} + \begin{bmatrix} C_2 \\ {C_1}^* \end{bmatrix} e^{-i\Omega\tau} \equiv |g_+\rangle + |g_-\rangle , \tag{3.12}$$

where $\Omega \equiv \delta_s - \delta$ and $|g_\pm\rangle$ are the vectors oscillating like $e^{\pm i\Omega\tau}$. A contribution to the wave number ($\sim z$) was not included in the exponent of the plane wave because g has to be phase matched with F and this was already included in eq. 3.2. In this model, the extension of the perturbation in time domain is infinite and the soliton core is then of negligible extension. This is the typical scenario where asymptotic analysis is performed so the perturbation propagation is considered in the limits $\tau \to \pm\infty$, where the dark soliton tail approaches a CW such that

$$\lim_{\tau\to\pm\infty}\partial_\tau^m F = 0; \forall m > 0$$
$$|F_\infty|^2 \equiv \lim_{\tau\to\pm\infty}|F|^2 = q, \tag{3.13}$$

so eq. 3.8 becomes a homogeneous system of differential equations

$$\hat{L}_\infty\left[|g_+\rangle + |g_-\rangle\right] = |0\rangle\,, \tag{3.14}$$

where both terms need to be separately zero and the nontrivial solutions ($C_{1,2} \neq 0$) can be found (considering only, e.g., the term $\sim |g_+\rangle$) by solving

$$\begin{vmatrix} \mathcal{W}_\infty(\Omega) & -{F_\infty}^2 \\ {F_\infty}^{*2} & -\mathcal{W}_\infty(-\Omega) \end{vmatrix} \equiv q^2 - \mathcal{W}_\infty(\Omega)\mathcal{W}_\infty(-\Omega) = 0, \tag{3.15}$$

where the action of the operator $\hat{W}_\infty$ has been replaced by the eigenvalue $\mathcal{W}_\infty(\Omega) \equiv \epsilon\Omega^3 - \frac{d}{2}\Omega^2 - \sin\phi\sqrt{qd}\Omega - q$, and yields to the sixth order resonance condition

$$\left\{\epsilon\Omega^3 - \frac{d}{2}\Omega^2 - \sin\phi\sqrt{qd}\Omega - q\right\}\left\{\epsilon\Omega^3 + \frac{d}{2}\Omega^2 - \sin\phi\sqrt{qd}\Omega + q\right\} = -q^2. \tag{3.16}$$

The solution $\Omega = 0$ is a double root and the mathematical reason for it is the existence of non vanishing off-diagonal terms in eq. 3.15. Because these terms are precisely the soliton tails it is clear to understand their physical meaning. Indeed, the tails of the dark soliton are two non zero amplitude plane waves at the carrier frequency and of course they couple with themselves. Eq. 3.16 reduces then to fourth order

$$\left(\epsilon\Omega^2 - \sin\phi\sqrt{qd}\right)^2 = \frac{d}{2}\left(\frac{d}{2}\Omega^2 + 2q\right) \tag{3.17}$$

with solutions

$$\Omega = \pm\frac{1}{\epsilon\sqrt{2}}\left[2\sin\phi\sqrt{qd}\epsilon + \frac{d^2}{4} \pm \sqrt{\left(2\sin\phi\sqrt{qd}\epsilon + \frac{d^2}{4}\right)^2 + 4qd\epsilon^2\cos^2\phi}\right]^{\frac{1}{2}}. \tag{3.18}$$

Because d is positive (the soliton stays in the normal GVD regime), the square root in eq. 3.18 is real and its modulus bigger than $\left|2\sin\phi\sqrt{qd}\epsilon + \frac{d^2}{4}\right|$, so Ω has two real and two imaginary roots, with opposite signs. The purely imaginary roots have

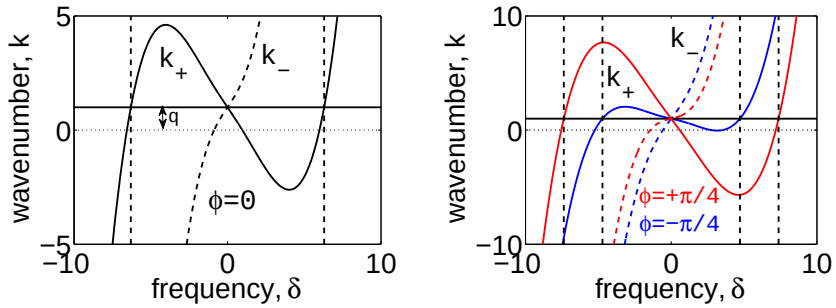

(a) (b)

Figure 3.2: Dispersion curves for dark soliton (black horizontal line) and the linear waves propagating on the two tails. Full curves correspond to k_+ (tail in which the radiation is observed) and dashed curves to k_- (tail in which only a little grey soliton is emitted, see fig. 3.5). The vertical dashed lines show the calculated resonant frequencies, according to eq. 3.18. Parameters: $q = 1$, $T_0 = 0.1$ps, $\epsilon = 1/12$, $\delta_s = 0$, $\phi = 0$ (left) and $\phi = \pm 0.25\pi$ (right)

the meaning of non radiative localised correction to the dip's profile [Karpman93], whereas the purely real ones correspond to the perturbation fields $g(\tau, z)$. From now on, we will only refer to the non zero real roots which are shifted from the soliton frequency by an equal amount $|\Omega|$.

An equivalent way of calculating the resonance condition is to include a nonzero perturbation wavenumber shift, k_r, in eq. 3.12, introducing the change $(\delta_s - \delta)\tau \rightarrow (\delta_s - \delta)\tau + k_{shift} z$ to reproduce eq. 3.16, and then solving the system of equations

$$\begin{cases} k_s = D_s + q = \epsilon\delta_s^3 + \frac{1}{2}\delta_s^2 + q \\ k_r = k_s + k_{shift} \equiv k_\pm = k_s - \epsilon\Omega^3 + \sin\phi\sqrt{qd}\Omega \pm \Omega\left[\frac{d^2}{4}\Omega^2 + qd\right]^{\frac{1}{2}} \end{cases} . \tag{3.19}$$

The phase matching condition $k_s = k_r \Leftrightarrow k_{shift} = 0$ leads the the resonance condition eq. 3.18. The resonances are the consequence of the intersection of the soliton dispersion with the one of the radiation on top of the CW background (see fig.3.2).

3.2.1 Effect of soliton greyness and frequency detuning

Fig.3.3 shows the Cherenkov roots for $\delta_s = 0$ along a period of the greyness phase, which provides some tunability for the resonant radiation. The effect of soliton de-

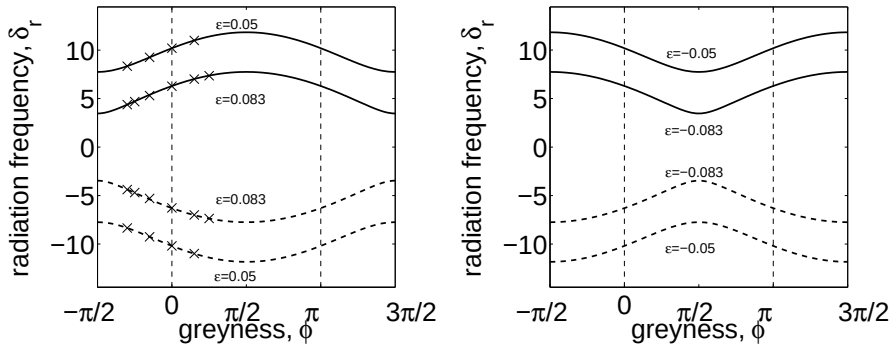

(a) (b)

Figure 3.3: Resonances of eq. 3.18 as a function of the greyness phase ($\phi \in \left[-\frac{\pi}{2}, 3\frac{\pi}{2}\right]$, $\epsilon = \frac{1}{12}$) for different positive (left) and negative (right) values of β_3. Full curves mark the most intense resonances whereas the weaker are on the dashed curves. The dashed vertical lines mark the black solitons (sin $=\equiv 0$). Soliton detuning from carrier was set to zero ($\delta_s = 0$). Crosses mark simulation results

tuning from the reference frequency can be seen in fig. 3.4, where δ_s varies along the normal dispersion regime. The roots fall to zero at the edge between normal and anomalous GVD, according with the fact that RR is not generated if $\beta_2 = 0$. However, both 3.3 and 3.4 show that the resonances are nonzero in the CW limit ($\phi = \pm\frac{\pi}{2}$), conversely to what one would expect, since higher order dispersion is known not to affect the CW solution of the NLSE and so there is no extra radiation generated by them. This will be understood in section 3.3, where the amplitude of the Cherenkov waves is calculated and found to be exactly zero for $\phi = \pm\frac{\pi}{2}$ (see eq. 3.60).

3.2.2 Numerical results

Direct simulation of eq. 3.1 with positive TOD, initialised with a seed satisfying periodic boundary conditions (PBC)

$$F_{seed}(\xi) = \mathrm{H}(\xi)F(\phi, \xi - \xi_0, z = 0) - [1 - \mathrm{H}(\xi)]\, F(-\phi, \xi + \xi_0, z = 0), \tag{3.20}$$

being $\mathrm{H}(\xi)$ the Heaviside step function, $\xi_0 > 100T_0$ and F given in eq. 3.6, gives the

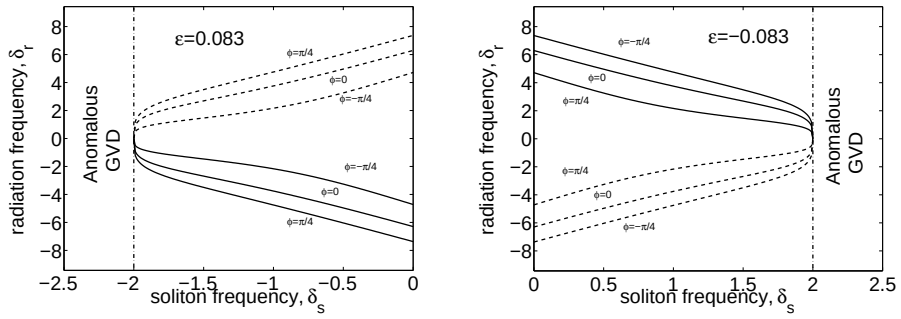

(a) (b)

Figure 3.4: Resonances of eq. 3.18 as a function of detuning, δ_s, for different ϕ values. $\beta_3 = 0.5ps^3/\text{Km}$ (left) and $\beta_3 = -0.5ps^3/\text{Km}$ (right). The dashed vertical lines mark the zero GVD point. The strongly emitted radiation is found along the full curves.

propagation picture shown in fig. 3.5.a. The temporal evolution shows the emission of radiation in both tails. In the leading edge, a lower amplitude grey soliton (bigger $|\phi|$ than the original dip) is emitted, but it is not considered in our analytics since we linearised the equation for the perturbation g (see eq. 3.8). In the trailing, the linear Cherenkov waves are seen to propagate on top of the soliton background generating fast oscillations in time domain as previously discussed in [Karpman93, Afanasjev96] which frequency components are given in eq. 3.18. The spectral features at $30L_D$ are shown in fig. 3.5d being the most relevant one the appearance of a sharp resonant peak in the anomalous dispersion regime. The agreement between simulations and resonance condition eq. 3.18 is also shown in this figure.

Changing the sign of ϵ in eq. 3.1 is equivalent to reverse the t axis so fig. 3.5 for $\epsilon < 0$ would be identical with the difference that the effects in the leading edge would occur in trailing instead and vice versa. For the same reason, spectral features would also be frequency reversed. Simulations with different greyness show the same features and the resonances found numerically are in excellent agreement with the theory (see fig. 3.3).

The cross-correlation frequency resolved optical gating (XFROG) spectrogram [Dudley06] in fig. 3.5b is used to make clear the relation between temporal and spectral features and it is calculated as

$$S(\delta,\xi) \equiv \left| \int_{-\infty}^{+\infty} d\xi' sech(\xi' - \xi) A(\xi) e^{-i\delta\xi} \right|^{0.1}, \tag{3.21}$$

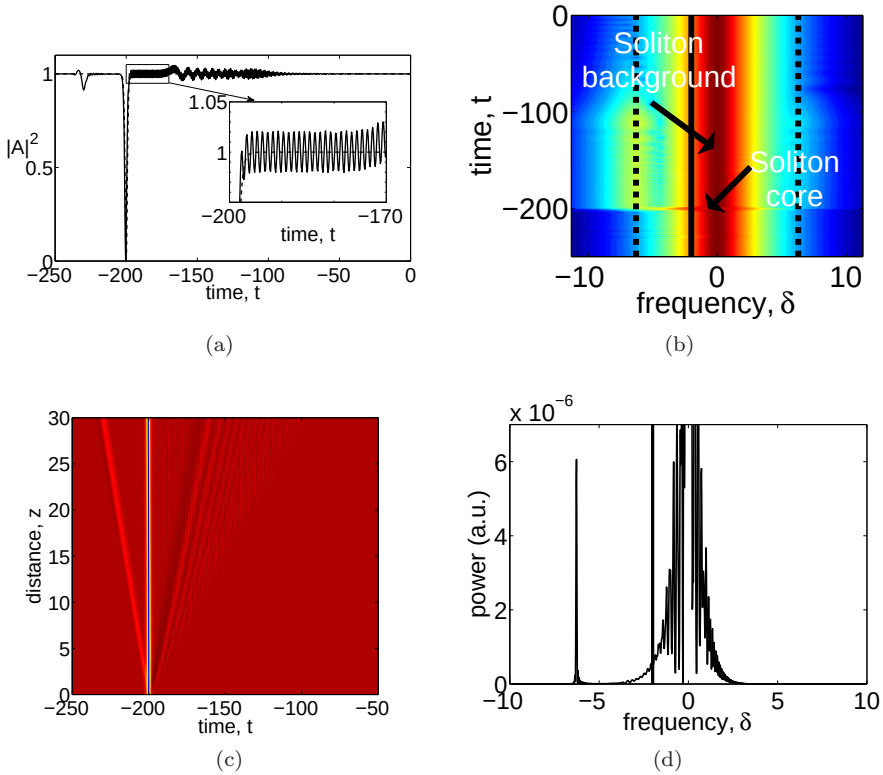

Figure 3.5: (c) Time domain evolution of a $T_0 = 100$fs black soliton along $30L_D$ of a fibre with $\epsilon = 1/12$. (a) is the final state of (c), which spectrum is shown in (d). (b) XFROG unifying (a) and (d). The zero GVD frequency is marked by the full black lines and theoretical predictions of the resonances (see eq. 3.18) are marked by the dashed lines.

where the power 0.1 is introduced to emphasise the fluctuations in the background intensity due to the radiation. Both real roots are seen to propagate on the same tail, as expected in eq. 3.19, although the intensity of the root in the normal GVD appears to be much smaller. Understanding the latter feature is one of the scopes of next section.

3.3 Radiation amplitude

According to fig. 3.5.a, the emission of radiation is assumed here to reach a steady state after the transient associated with the emission of the grey soliton in the opposite tail. This is in agreement with numerical simulations performed along a distance which is short enough to consider that the soliton parameters do not drift during the radiation emission. The model is based on a perturbative approach in the perturbation field coefficients. Breaking to first order the CW approximation done for the RR frequency in the previous section, the perturbation is taken in the form

$$g(\tau, z) = G_1(\tau, z)e^{i\Omega\tau} + G_2^*(\tau, z)e^{-i\Omega\tau}, \tag{3.22}$$

which contains the waves at the two resonant frequencies propagating on top of the same soliton tail and $\partial_\tau^m G_{1,2}^{(*)} \approx 0 \forall m > 1$. Substituting eq. 3.22 into eq. 3.8 gives

$$\begin{aligned} &\left\{\partial_z G_1 + \chi^+\partial_\tau G_1 + i\mathcal{W}^+ G_1 - iF^2 G_2\right\} e^{i\Omega\tau} + \\ &+ \left\{\partial_z G_2^* + \chi^-\partial_\tau G_2^* + i\mathcal{W}^- G_2^* - iF^2 G_1^*\right\} e^{-i\Omega\tau} = \epsilon\partial_\tau^3 F \equiv B(\tau), \end{aligned} \tag{3.23}$$

where the group velocity coefficients $\chi^\pm \equiv \partial_\Omega \mathcal{W}^\pm$ and $\mathcal{W}^\pm \equiv \mathcal{W}(\pm\Omega)$. The RHS of eq. 3.23, $B(\tau) \equiv \epsilon\partial_\tau^3 F(\tau, z)$, is the driving term for the perturbation growth. This term is not important for the radiation frequency calculation, but neglecting it yielded to arbitrary amplitudes $C_{1,2}$ in section 3.2. In other words, the soliton core is needed to fix the radiation amplitude. The driving term can be written as

$$\begin{aligned} B(\tau) &= B_+(\tau)e^{i\Omega\tau} + B_-(\tau)e^{-i\Omega\tau} \\ B_\pm(\tau) &\equiv \int_{-\infty}^{-\Omega} \frac{d(\Omega' - \Omega)}{2\pi} \widetilde{B}(\mp\Omega')e^{\pm i(\Omega' - \Omega)\tau} \end{aligned} \tag{3.24}$$

The resonant nature of the radiation (small spectral width) and the fact that Ω is large compared with the soliton spectral width let us assume that the functions $B_\pm(\tau)$

are slowly varying function compared to the terms $e^{\pm i\Omega\tau}$. This implies that most of the resonant radiation at the frequency Ω is excited by the Fourier components of the driving term, $\widetilde{B}(\Omega)$, around that frequency, what means that the sources for the RR at $\pm\Omega$, $B_{\pm}(\tau)$, can be approximately replaced by the whole source, $B(\tau) \equiv \int_{-\infty}^{+\infty} \frac{d\Omega'}{2\pi} \widetilde{B}(\Omega') e^{-i\Omega'\tau}$, since the only difference is the extent of the integral into a frequency region far detuned from $\pm\Omega$ that barely contributes to the radiation. Under these considerations eq. 3.23 becomes a system of coupled equations for G_1 and G_2

$$\partial_z |a\rangle + \hat{\chi}\partial_\tau |a\rangle + i\hat{L}|a\rangle = |B\rangle\,, \tag{3.25}$$

where

$$|a\rangle = \begin{bmatrix} G_1 \\ G_2 \end{bmatrix} \tag{3.26}$$

$$\hat{\chi} = \begin{bmatrix} \chi^+ & 0 \\ 0 & \chi^- \end{bmatrix} \tag{3.27}$$

$$\hat{L} = \begin{bmatrix} \mathcal{W}^+ & -F^2 \\ F^{*^2} & -\mathcal{W}^+ \end{bmatrix} \tag{3.28}$$

$$|B\rangle = \begin{bmatrix} B \\ B^* \end{bmatrix} e^{-i\Omega\tau}. \tag{3.29}$$

Simulations in section 3.2 showed that only one of the roots was of relevant magnitude. Our aim now is to understand why one of them is much stronger than the other and to obtain an approximate equation for the former one.

3.3.1 Equations for the two resonant waves

To solve eq. 3.25 we take advantage from the bi-orthogonality relations satisfied by the eigenvectors of $\hat{L}_\infty$, $|z_\pm\rangle$, and $\hat{L}^\dagger_\infty$, $|v_\pm\rangle$, i.e., $\langle z_m | v_n\rangle = \delta_{mn}$ (m and n are symbolic representation for $+$ and $-$), which share the eigenvalues

$$\begin{array}{c} \lambda_+ = 0 \\ \lambda \equiv \lambda_- = \mathcal{W}^+_\infty - \mathcal{W}^-_\infty \end{array}\,, \tag{3.30}$$

where the resonance condition $\left|\hat{L}_\infty\right| \equiv q^2 - \mathcal{W}^-_\infty \mathcal{W}^+_\infty = 0$ (see eq. 3.15) implies $\mathcal{W}^+_\infty \mathcal{W}^-_\infty = q^2$. For the following calculations it is useful to know that the eigenvectors

$$|z_\pm\rangle \equiv \frac{1}{\mathcal{W}^{\pm^2}_\infty - q^2} \begin{bmatrix} F^2_\infty \\ \mathcal{W}^\pm_\infty \end{bmatrix},\ |v_\pm\rangle \equiv \begin{bmatrix} -F^2_\infty \\ \mathcal{W}^\pm_\infty \end{bmatrix} \tag{3.31}$$

satisfy properties

$$\begin{array}{c} \langle z_\pm \, | z_\pm \rangle = \frac{q^2+\mathcal{W}_\infty^{\pm 2}}{[\mathcal{W}_\infty^\pm \lambda]^2}, \; \langle z_\pm \, | z_\mp \rangle = \frac{-2}{\lambda^2} \\ \langle z_m \, | v_n \rangle = \delta_{mn}, \; \langle v_m \, | v_n \rangle = q^2 + \mathcal{W}_\infty^m \mathcal{W}_\infty^n \\ |z_\pm\rangle = \frac{1}{\mathcal{W}_\infty^{\pm 2} - q^2} \begin{bmatrix} -1 & 0 \\ 0 & 1 \end{bmatrix} |v_\pm\rangle \end{array} . \tag{3.32}$$

Using any of the two resonant frequencies, $\pm\Omega$, to evaluate the scalar products one finds that $\langle z_m \mid z_n \rangle \sim \mathcal{O}(\epsilon^4)$, because $\Omega = \pm 1/2\epsilon + \mathcal{O}(1)$.

We proceed by introducing the expansion $|a\rangle = U(\tau, z)\,|z_+\rangle + D(\tau, z)\,|z_-\rangle$ in eq. 3.25 to obtain

$$\begin{array}{l} \partial_z \left[U\,|z_+\rangle + D\,|z_-\rangle\right] + \hat{\chi}\partial_\tau \left[U\,|z_+\rangle + D\,|z_-\rangle\right] + i\hat{L}_\epsilon \left[U\,|z_+\rangle + D\,|z_-\rangle\right] + \\ iD\left[\mathcal{W}_\infty^+ - \mathcal{W}_\infty^-\right]|z_-\rangle = |B\rangle\,, \end{array} \tag{3.33}$$

where

$$\hat{L}_\epsilon \equiv \hat{L} - \hat{L}_\infty = \begin{bmatrix} -2\left(|F|^2 - q\right) & -F^2 + F_\infty^2 \\ F^{*^2} - F_\infty^{*^2} & 2\left(|F|^2 - q\right) \end{bmatrix}, \tag{3.34}$$

which, when projected onto the vectors $\langle v_\pm|$, using properties in eq. 3.32, gives the two coupled equations for the amplitudes U and D,

$$\begin{array}{l} \partial_z U + \partial_\tau U \,\langle v_+|\,\hat{\chi}\,|z_+\rangle + \partial_\tau D\,\langle v_+|\,\hat{\chi}\,|z_-\rangle + iU\,\langle v_+|\,\hat{L}_\epsilon\,|z_+\rangle + \\ iD\,\langle v_+|\,\hat{L}_\epsilon\,|z_-\rangle = \langle v_+\,|B\rangle \end{array} \tag{3.35}$$

$$\begin{array}{l} \partial_z D + \partial_\tau U \,\langle v_-|\,\hat{\chi}\,|z_+\rangle + \partial_\tau D\,\langle v_-|\,\hat{\chi}\,|z_-\rangle + iU\,\langle v_-|\,\hat{L}_\epsilon\,|z_+\rangle + \\ iD\,\langle v_-|\,\hat{L}_\epsilon\,|z_-\rangle + iD\left[\mathcal{W}_\infty^+ - \mathcal{W}_\infty^-\right] = \langle v_-\,|B\rangle\,. \end{array} \tag{3.36}$$

The expansion of $|a\rangle$ can be expressed through eqns. 3.26 and 3.31 in the more explicit form

$$\begin{bmatrix} G_1 \\ G_2 \end{bmatrix} = \frac{U}{\mathcal{W}_\infty^{+^2} - q^2} \begin{bmatrix} F_\infty^2 \\ \mathcal{W}_\infty^+ \end{bmatrix} + \frac{D}{\mathcal{W}_\infty^{-^2} - q^2} \begin{bmatrix} F_\infty^2 \\ \mathcal{W}_\infty^- \end{bmatrix}, \tag{3.37}$$

which together with eqns. 3.35 and 3.36 tell us about the relative strength between U and D, as described below. Indeed, the strongly radiating root is the one spectrally located in the anomalous dispersion regime, so its frequency is $sign(\epsilon)\Omega$ (because $\Omega \equiv \delta_s - \delta$). Mathematically, because $\Omega \approx 1/2\epsilon$, $\lambda \sim \mathcal{O}(1/\epsilon^2)$ and it becomes large

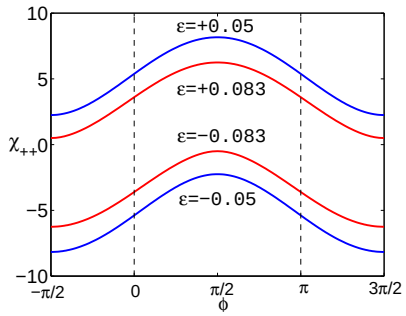

Figure 3.6: Inverse group velocity coefficient of eq. 3.40.

enough for eq. 3.36 to show that $D \approx \frac{B}{\lambda} \sim \mathcal{O}(\epsilon^3)$ (after neglecting all the terms containing derivatives or $\sim \hat{L}_\epsilon$). Considering that the scalar product (U,D constants now)

$$\langle a \mid a \rangle = |U|^2 \langle z_+ \mid z_+ \rangle + |D|^2 \langle z_- \mid z_- \rangle + U^* D \langle z_+ \mid z_- \rangle + + U D^* \langle z_- \mid z_+ \rangle \tag{3.38}$$

is of order $g^2 \sim \mathcal{O}(\epsilon^2)$, that all the brackets are $\sim \mathcal{O}(\epsilon^4)$, and $D \sim \epsilon^3$), proves that $U \sim 1/\epsilon$ (otherwise the order of g is not reached) and so $|U| >> |D|$, what implies that the second term in the RHS of eq. 3.37 can be neglected and then eq. 3.35 can be simplified, neglecting the terms $\sim D$, to

$$\partial_z U + \hat{\chi}_{++} \partial_\tau U + i \hat{L}_{\epsilon++} U = B_+, \tag{3.39}$$

and its coefficients are

$$\hat{\chi}_{++} \equiv \langle v_+ \mid \hat{\chi} \mid z_+ \rangle = 3\epsilon\Omega^2 - d\Omega \frac{q^2 + \mathcal{W}_\infty^{+2}}{q^2 - \mathcal{W}_\infty^{+2}} - \sin\phi \sqrt{qd} \tag{3.40}$$

$$\hat{L}_{\epsilon++} \equiv \langle v_+ \mid \hat{L}_\epsilon \mid z_+ \rangle = 2\left[q - |F|^2\right] \frac{q^2 + \mathcal{W}_\infty^{+^2}}{q^2 - \mathcal{W}_\infty^{+^2}} + \frac{2\mathcal{W}_\infty^+}{q^2 - \mathcal{W}_\infty^{+^2}} \mathbb{R}\left\{ F_\infty^{*^2} \left[F_\infty^2 - F^2 \right] \right\} \tag{3.41}$$

$$B_+ \equiv \langle v_+ \mid B \rangle = 2\epsilon q^2 \frac{\cos^4\phi}{d^{\frac{3}{2}}} \frac{1 - 2\sinh^2\Theta}{\cosh^4\Theta} \left[F_\infty^{*^2} - \mathcal{W}_\infty^+ \right] e^{-i\Omega\tau}. \tag{3.42}$$

The magnitude of the coefficients can be seen in figs. 3.6, 3.7 and 3.8.

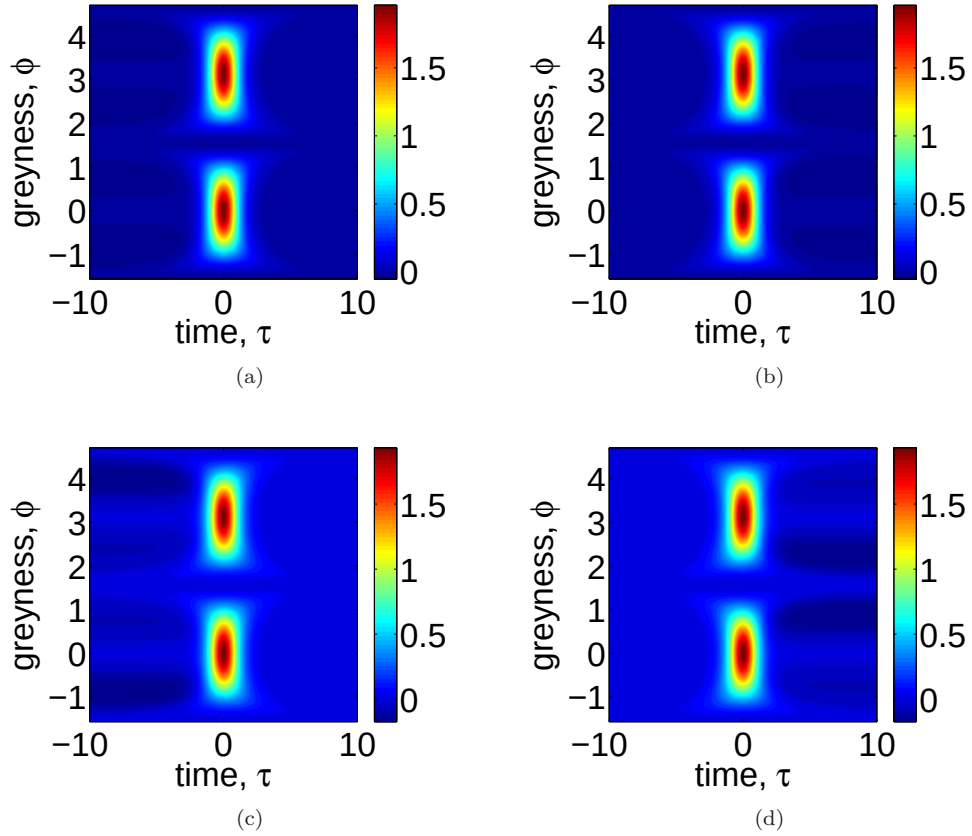

Figure 3.7: Potential coefficient of eq. 3.41. $\epsilon > 0 (> 0)$ in left (right) column and $|\epsilon| = 0.05$ (0.083) in top (bottom) row.

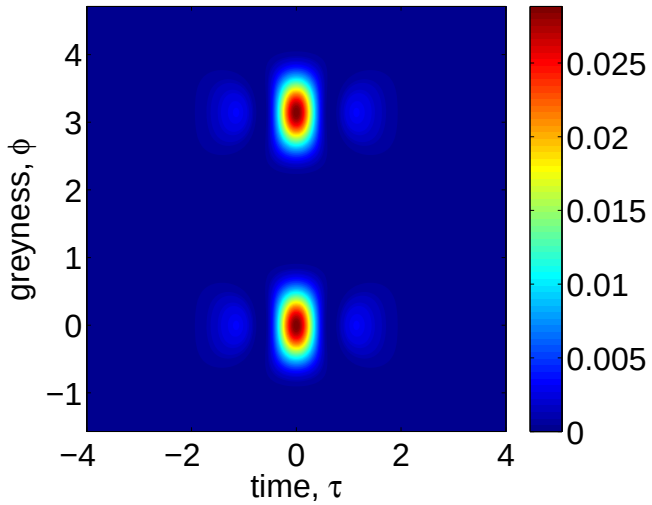

Figure 3.8: Modulus square of the driving coefficient with $\delta_s = 0$ and $q = 1$.

3.3.2 Ratio between the spectral resonant peaks

After neglecting the terms $\sim D$ in eq. 3.37, the relative strength between the resonant peaks is given by the modulus of the ratio between the components of the vector $|z_+\rangle$,

$$R \equiv \left|\frac{G_1}{G_2}\right|^2 = \frac{q^2}{\mathcal{W}_\infty^{+^2}}. \tag{3.43}$$

Fig. 3.9a shows that the predicted ratio dramatically increases when $|\epsilon|$ becomes smaller and it is in excellent agreement with the simulation results (dots). The reason for this big ratio is simply that $\beta(\Omega)$ tends to zero when $|\epsilon|$ is small, as shown in fig. 3.9b. It turns out that the strong radiation oscillates at the frequency $\Omega = sign(\epsilon)|\Omega|$ and it always lies in the anomalous GVD region, according to figs.3.5b,d and to the figures shown later on in this chapter.

3.3.3 Amplitude of the stronger RR root

The general solution of eq. 3.39 is found in the integral form

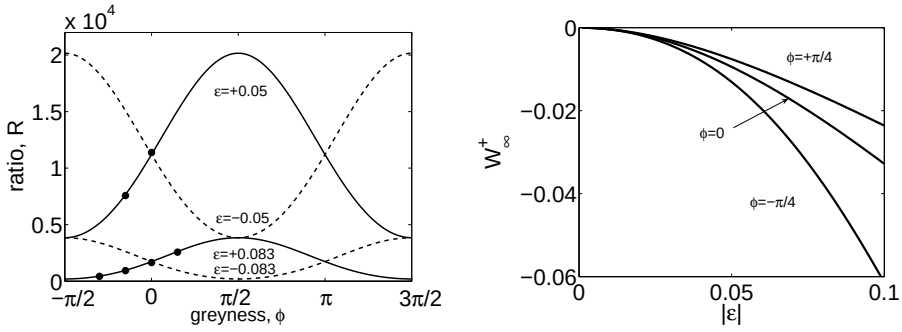

(a) (b)

Figure 3.9: (a) Intensity ratio of the two spectral peaks for different values of TOD coefficient, ϵ, as a function of greyness phase, ϕ. Curves correspond to the ratio predicted by eq.3.43 and black points to the numerical modelling results. (b) $\mathcal{W}_{\infty}^{+}$ as a function of $|\epsilon|$ for several values of ϕ.

$$U(\tau, z) = \frac{e^{-iS(\tau)}}{\hat{\chi}_{++}} \int_{\tau - \hat{\chi}_{++} z}^{\tau} dx B_{+}(x) e^{iS(x)}, \tag{3.44}$$

with

$$S(\tau) \equiv \frac{1}{\chi_{++}} \int d\tau L_{\epsilon++} = \frac{1}{\hat{\chi}_{++}} \frac{2}{q^2 - \mathcal{W}_{\infty}^{+2}} \left\{ \left[q^2 + \mathcal{W}_{\infty}^{+2} \right] \cos\phi \sqrt{qd} \tanh\Theta + \mathcal{W}_{\infty}^{+} \left[\tau q^2 - \int d\tau \mathrm{Re}\left(F_{\infty}^{*2} F^2 \right) \right] \right\} \tag{3.45}$$

and

$$\int d\tau \mathrm{Re}\left(F_{\infty}^{*2} F^2 \right) = \tau q^2 \cos^2(2\phi) - q^{\frac{3}{2}} \sqrt{d} \tanh\Theta \cos\phi \cos(2\phi) + 4 q^{\frac{3}{2}} \sqrt{d} sign(\cos\phi) sign(\epsilon) \ln(\cosh\Theta) \sin^2\phi \cos\phi. \tag{3.46}$$

$-\hat{\chi}_{++}$ is the radiation inverse phase velocity in the reference frame defined by τ, which is consistent with the fact that $\hat{\chi}_{++}$ and ϵ have the same sign and also implies the condition $|\hat{\chi}_{++} z| > |\tau|$, restoring causality in the integral of eq. 3.44, which is nonlocal in time and extends from the soliton dip to the radiation wave front. The asymptotic values of the amplitude are

$$\lim_{z\to\infty,\tau\to-sign(\epsilon)\infty} U(\tau,z) = 0 \tag{3.47}$$

$$\lim_{z\to\infty,\tau\to sign(\epsilon)\infty} U(\tau,z) = sign(\epsilon)\frac{e^{-iS(sign(\epsilon)\infty)}}{\hat{\chi}_{++}} I \tag{3.48}$$

with

$$I \equiv \int_{-\infty}^{\infty} d\tau B_+(\tau)\, e^{iS(\tau)} \tag{3.49}$$

and

$$S(\tau\to sign(\epsilon)\infty) = \frac{|\epsilon|}{\epsilon}\frac{2\sqrt{qd}\cos\phi}{\chi_{++}[q^2-\mathcal{W}_\infty^{+2}]}[q^2+q\mathcal{W}_\infty^+\cos 2\phi+\mathcal{W}_\infty^{+2}]. \tag{3.50}$$

Equations 3.47 and 3.48 state that the resonant radiation travels on top of the trailing (leading) tail for positive (negative) ϵ, in agreement with numerics (see fig.3.5). Because for the radiation tail $\mathcal{W}_\infty = \mathcal{O}(\epsilon^2) << q$, eqns. 3.40, 3.41 and 3.42 may be simplified to

$$\hat{\chi}_{++} \approx 3\epsilon\Omega^2 - d\Omega - \sin\phi\sqrt{qd} \tag{3.51}$$

$$\hat{L}_{\epsilon++} \approx 2\left[q - |F|^2\right] \tag{3.52}$$

$$B_+ \approx \epsilon(\partial_\tau^3 F)F_\infty^{*^2} e^{-i\Omega\tau} = 2\epsilon q^2 \frac{\cos^4\phi}{d^{\frac{3}{2}}}\frac{1-2\sinh^2\Theta}{\cosh^4\Theta}F_\infty^{*^2}e^{-i\Omega\tau}, \tag{3.53}$$

which let us rewrite eqns. 3.45-3.50 as

$$S(\tau) \approx \frac{2\sqrt{qd}\cos\phi}{\hat{\chi}_{++}}\tanh\Theta \tag{3.54}$$

$$S(\tau\to sign(\epsilon)\infty) \approx \frac{|\epsilon|}{\epsilon}\frac{2\sqrt{qd}\cos\phi}{\chi_{++}} \tag{3.55}$$

$$U_\infty \equiv \lim_{z\to\infty,\tau\to sign(\epsilon)\infty} U(\tau,z) = \frac{|\epsilon|}{\hat{\chi}_{++}} I e^{-iS_\infty}, \tag{3.56}$$

$$I \equiv F_\infty^{*2}\int_{-\infty}^{\infty} d\tau\partial_\tau^3 F e^{i[S(\tau)-\Omega\tau]}. \tag{3.57}$$

By realising that the driving term is a localised function in τ, the tanh inside $S(\tau)$ can be approximated by its argument and eq. 3.57 becomes the Fourier transform of the driving at the frequency $\widetilde{\Omega}$. The asymptotic amplitude finally reads

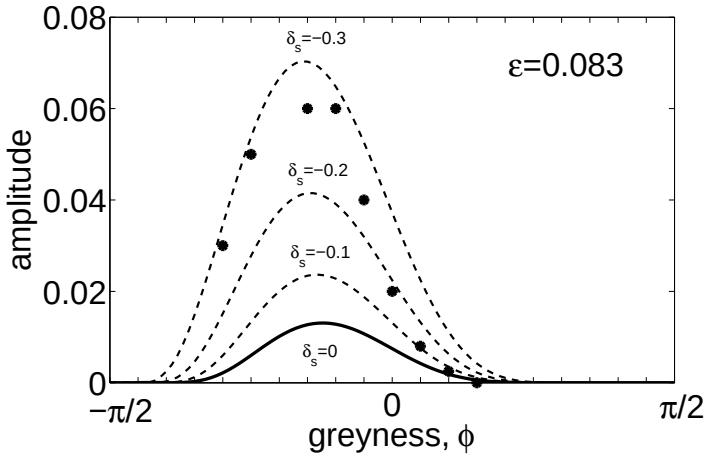

Figure 3.10: Amplitude $q - |A|^2$ as a function of greyness, ϕ, for several soliton detuning values, δ_s. Curves correspond to theoretical predictions (from eq.3.60) and dots to numerical modelling with initial values $q = 1$, $\epsilon = 1/12$ and $\delta_s = 0$.

$$U_\infty \approx \frac{\pi|\epsilon|\sqrt{d}\widetilde{\Omega}^3}{\hat{\chi}_{++}} F_\infty^{*2} Csch\left(\frac{\pi\widetilde{\Omega}}{2\sqrt{q/d}\cos\phi}\right) e^{-iS_\infty}, \tag{3.58}$$

where

$$\widetilde{\Omega} \equiv \frac{2q\cos^2\phi}{\hat{\chi}_{++}} - \Omega. \tag{3.59}$$

With all the developed above, the asymptotic expression for the perturbation field in eq. 3.22 reads

$$g_\infty \approx -\frac{\pi|\epsilon|\sqrt{d}\widetilde{\Omega}^3}{\hat{\chi}_{++}} e^{-iS_\infty} Csch\left(\frac{\pi\widetilde{\Omega}}{2\sqrt{q/d}\cos\phi}\right) e^{i\Omega\tau}. \tag{3.60}$$

g_∞ does not depend on time, what means that the perturbation is a nondispersive or superfluid wave packet. However, this is a consequence of the assumption made in eq. 3.22 that $\partial_\tau^m G \approx 0\ \forall m > 1$, which automatically prevents a GVD term $\sim \partial_\tau^2 G$ from appearing in eq. 3.25. Hence it is, in principle, true only up to first order approximation, since the amplitude U is associated to the superfluid eigenvector, i.e., the one with the zero eigenvalue in the spectrum of $\hat{L}_\infty$ (and $\hat{L}_\infty^\dagger$).

Fig.3.10 shows the amplitude of the soliton background oscillationsdue to radiation (see inset of fig. 3.5a) as a function of ϕ and $\epsilon > 0$. The dots correspond to the

simulation results with $\delta_s = 0$ as input, whereas the lines show the analytical results derived from eq. 3.58, for different values of soliton frequency detuning, $\delta_s = 0$. Several important features of fig. 3.10 are discussed below.

The functional behaviour of the amplitude eq. 3.60 as a function of greyness is well reproduced by the simulations and it can be understood as follows. The radiation frequencies, solution of eq. 3.18, are plotted in fig. 3.4 as a function of soliton background detuning, for different values of ϕ and $\epsilon > 0$. Note that grey solitons with $\phi < 0$ will radiate stronger than $\phi > 0$ because their backgrounds are spectrally closer to their roots and the efficiency of energy transfer will be therefor higher. However, when $|\phi|$ increases towards the CW limit, the spectral content of the frequency in resonance decreases. These two effects compete for $\phi < 0$, resulting in the typical optimisation curve shape seen in fig. 3.10, where the maximum amplitude is achieved by a greyness of $\phi \approx -\pi/8$.

Regarding the absolute value of the amplitude, fig. 3.10 shows that the agreement between the theory and the modelling depends strongly on the soliton background shift, δ_s. Although the initial value in simulations is $\delta_s = 0$, we indeed expect a little shift of this parameter along the propagation. The soliton greyness is also expected to change during propagation, however the dependence of the amplitude with greyness showed in fig. 3.10 suggests that the effect of a little drift in ϕ is much smaller than the one of a little change of δ_s, so we do not consider it in the discussion. We focus below in the origin of the soliton frequency shift and its influence on the strength of the Cherenkov radiation.

Dark solitons keep the resonant radiation extended on top of one tail so the linear waves mix with the background. Therefor, for positive (negative) TOD the frequency of g is smaller (bigger) than the soliton carrier and averages down (up) the soliton background frequency δ_s. The spectrum is in any case moved towards the zero GVD, increasing the energy efficiency transfer to the RR and its amplitude [Milián09]. Due to this, the discrepancy between theory and modelling will be bigger when the strength of the emitted radiation is bigger too. In fig. 3.10, the maximum δ_s required to match the numerical results (at $\phi \approx -\pi/8$) is of $\delta_s \sim -0.26$, which is a small fraction of the spectral distance, Δ, between the initial soliton carrier and the zero GVD frequency $\Delta \equiv \delta_{GVD} - \delta_s = -2$, $\delta_s \approx \Delta/8$ (the case of $\epsilon < 0$ is mirror image in ϕ axis). This explains qualitatively the discrepancy between the predicted curve at $\delta_s = 0$ and the modelling. How to estimate quantitatively the background frequency shift is still an opened problem that we did not face here.

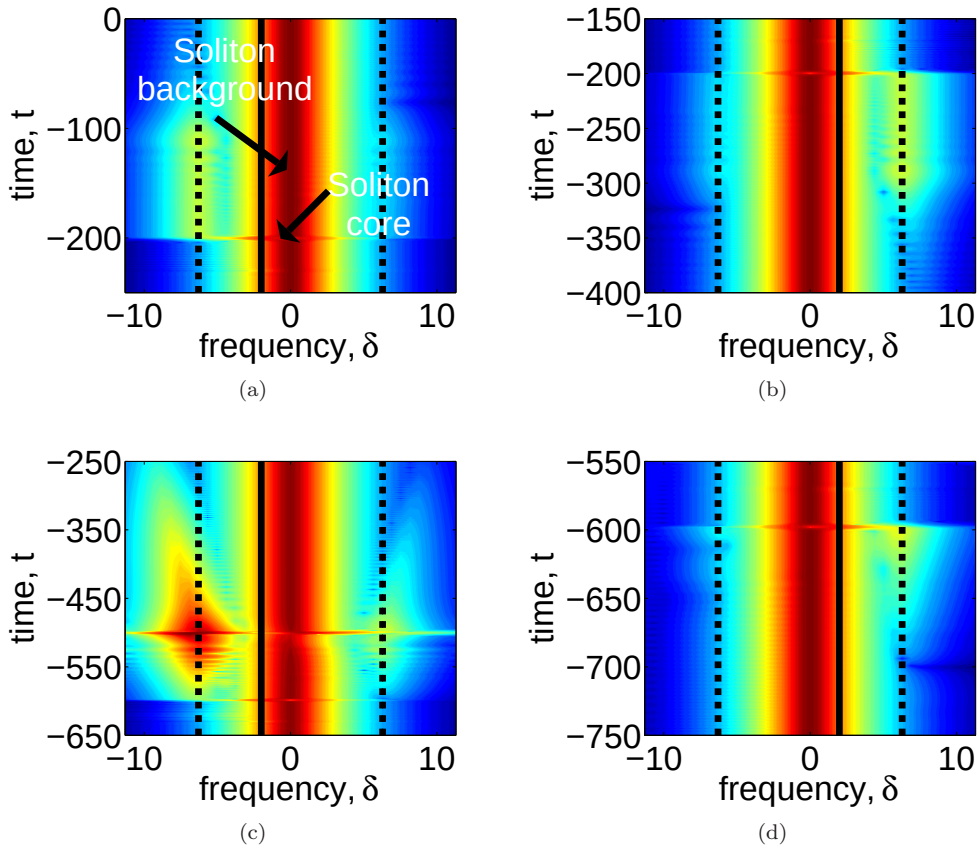

Figure 3.11: Black solitons after propagating $30L_D$ with TOD perturbation only (top) and with Raman on (bottom). $\epsilon > 0 (< 0)$ in the left (right) figures. Solid lines mark the zero GVD and dashed the predicted resonant frequencies.

3.3.4 Raman effect

When the Raman term is taken into account, eq. 3.1 takes the form of eq. 2.39 with $M = 3$ and $\tau_{shock} = 0$,

$$-i\partial_z A + \frac{1}{2}\partial_t^2 A + i\epsilon\partial_t^3 A = A\int_{-\infty}^{+\infty} dt' R(t')|A(t-t')|^2, \tag{3.61}$$

where the Raman response function is the one in eq. 2.33 with $\tau_1 = 12.2/T_0(fs)$ and $\tau_2 = 32/T_0(fs)$. Its main effect can be seen for black solitons in fig. 3.11

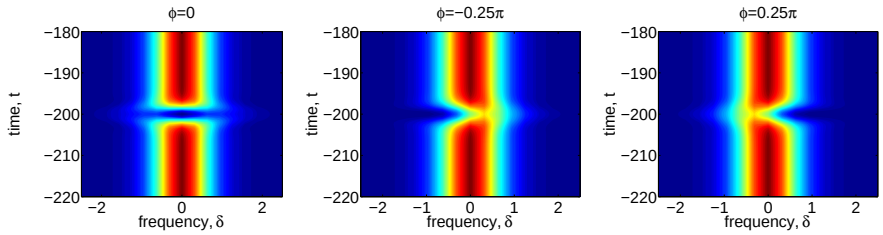

(a) (b) (c)

Figure 3.12: XFROG diagrams of unperturbed (a) black and (b,c) grey solitons with $\phi = \pm 0.25\pi$.

and is to change the intensity of the resonant radiation (not the frequency), being both radiation peaks dramatically amplified for positive TOD coefficient ($\epsilon > 0$) and almost suppressed for negative TOD ($\epsilon < 0$). This proofs that the Raman scattering decreases the soliton frequency, moving it towards the zero GVD if $\epsilon > 0$, enhancing the efficiency of energy transfer from the soliton to the RR. The opposite happens if $\epsilon < 0$. The spectral asymmetry introduced by Raman effect for the different signs of ϵ was experimentally measured by [Weiner89].

In physical grounds and according to the second law of thermodynamics [Sears75], inelastic interactions (such as Raman) between optical solitons (of any kind) and mater vibrations (phonons) are expected to occur in a way in which the energy flows from the optical state to the phonons [Saleh11a]. This is simply because the optical solitons are coherent (ordered) states whereas the phonon vibrations are incoherent or basically noise (disordered). If disorder is to increase in the light-matter system, one could intuitively predict that *ordered energy* is converted into *disordered emery*, that is, the phonons energy increases at the expense of the soliton energy, whose decrease induces an average frequency down- or red-shift. A soliton blue shift can only occur, according to this idea, if the classical analogue photon number [Blow89] is not conserved. Indeed, soliton blue-shift in lossy (plasmonic) systems has been recently observed [Saleh11b].

Grey solitons also respond to Raman effect differently, depending on the sign of ϕ, as discussed now. The stationary reference frame introduced in setcion 3.1 moves with the physical (lab frame) group velocity given by

$$V_{Grey}(\delta, \phi, q; \epsilon) = \frac{V_0}{1 + \frac{V_0 T_0}{L_D}[D'_s + \sin\phi\sqrt{qd}]}, \tag{3.62}$$

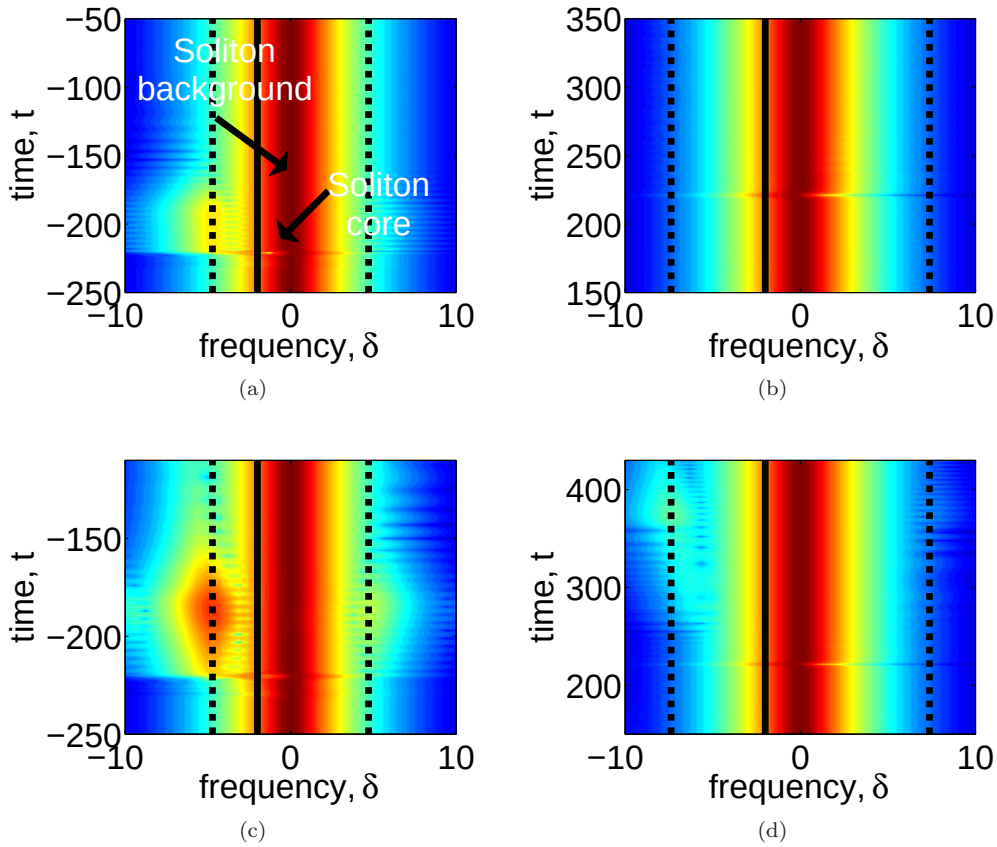

Figure 3.13: Solitons after propagating $30L_D$. (a) $\phi = -\frac{\pi}{4}$ and (b) $\phi = \frac{\pi}{4}$ under positive TOD perturbation only. (c) and (d) show, respectively, the Raman amplification ($\epsilon > 0$) for the radiation emitted in (a) and (b).

where the constant $V_0 \equiv 1/\beta_1(\delta_s) > 0$ is the group velocity of the unshifted black soliton. Although solitons with greyness of opposite sign have equal intensity profiles and background frequencies, their spectrum centre of mass shifts from δ_s differently (see figs. 3.12b,c), leading to their different velocities. Note by eq. 3.62 that the slower one always has positive phase ϕ, regardless the sign of ϵ.

TOD and Raman effects perturb grey solitons qualitatively in the same way as they do for black solitons. However, as seen in fig. 3.13 the sign of the greyness phase introduces important differences. For $\epsilon > 0$, the faster one ($\phi < 0$) radiates always

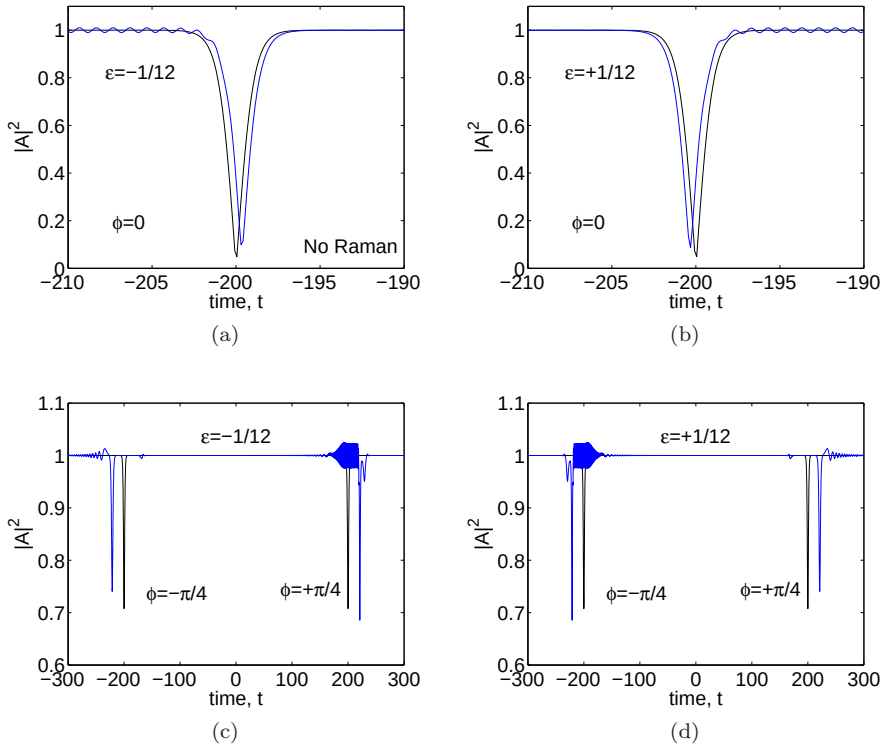

Figure 3.14: Perturbation of black (top) and grey (bottom) solitons under TOD only after propagation distance of $30L_D$ in fibres with the different sign of ϵ.

stronger and the opposite occurs when ϵ is negative. In terms of energy transfer it is clear from figs. 3.4.a and 3.3.a that it should occur in this way because the roots are closer in frequency domain for the faster soliton. This is the opposite of what one would naively expect, since the soliton which radiates stronger has its spectral centre of mass moved away from the zero GVD point and the efficiency of the energy transfer would be expected to decrease. However, this argument does not apply here since there is no shift in the background carrier δ_s. The greyness phase represents an internal degree of freedom with its particular physics.

Grey soliton velocity depends on both δ_s and ϕ, see eq. 3.62, which are modified by TOD and Raman at the same time. On the one hand, the two effects induce a frequency shift. Raman redshifts δ_s (see fig. 3.11) and TOD induces a shift because of the radiation being extended on top of the CW background. In fact, the radiation averages up (down) δ_s for $\epsilon < 0$ ($\epsilon > 0$). On the other hand, there is the greyness shift.

Fig.3.14 shows the initial (black) and final (blue) states of dark solitons after $30L_D$ with different input ϕ and perturbed under TOD only, which is seen to induce a shit $\phi \to \pm\pi/2$ under $\pm|\epsilon|$ perturbation. Perhaps the reason behind it is as follows. The RR soaks away the soliton spectral component in resonance, creating an asymmetry in the dark soliton spectrum around the dip resembling the typical spectral asymmetry of grey solitons (see fig. 3.12). Actually, in terms of dark soliton spectra, $\epsilon > 0$ ($\epsilon < 0$) induces a $\phi < 0$ ($\phi > 0$) type defect. Two effects could be simultaneously associated to the creation of such defect. First, the soliton throws it away in the form of a $\phi < 0$ ($\phi > 0$) grey soliton for $\epsilon > 0$ ($\epsilon < 0$). According to eq. 3.62, for positive (negative) ϵ this low amplitude soliton is faster (slower) than the original one, conversely to radiation and hence they must propagate on top of opposite background tails, as all the simulations confirm. Second, the soliton spectrum stability recombines internal frequencies to compensate for this defect. If most of them come from frequencies further detuned from the zero GVD frequency than δ_s, then the soliton spectrum induces to itself the greyness shift consistent with figs. 3.14a-d.

Raman effect is shown in fig. 3.15 and always slows down the solitons, regardless their initial greyness and ϵ. According to eq. 3.62, it implies, together with the red-shift, that Raman always induces the shift $\phi \to +\pi/2$.

The picture explained above is expected to hold in the cases where TOD is of important magnitude, that is for black solitons and the dark ones with $\phi > 0$ when $\epsilon < 0$ and vice versa. In the cases greyness has the same sign as TOD, the nonradiative corrections to the soliton dip (imaginary roots of eq. 3.18) may introduce their own ϕ-shifts. In fact, the initially $\phi = -\pi/4$ soliton in fig. 3.15c does not seem to evolve according to the previous explanation.

3.4 Continuum generation in the realistic excitation

Higher order dark solitons that decay, under the presence of higher order effects, into a train of fundamental dark solitons (as for bright solitons), each with different amplitude, width, carrier frequency and phases, do not exist. However, a train of dark solitons with these features can be generated, as proposed and observed in [Rothenberg91, Rothenberg92], by the interference of two suitably delayed (bright) pulses in the normal dispersion regime. The different amplitude and carrier frequencies in this case are due to the strongly chirped state of the whole pulse. Hence, if higher order effects are present in the system and their characteristic lengths are bigger than

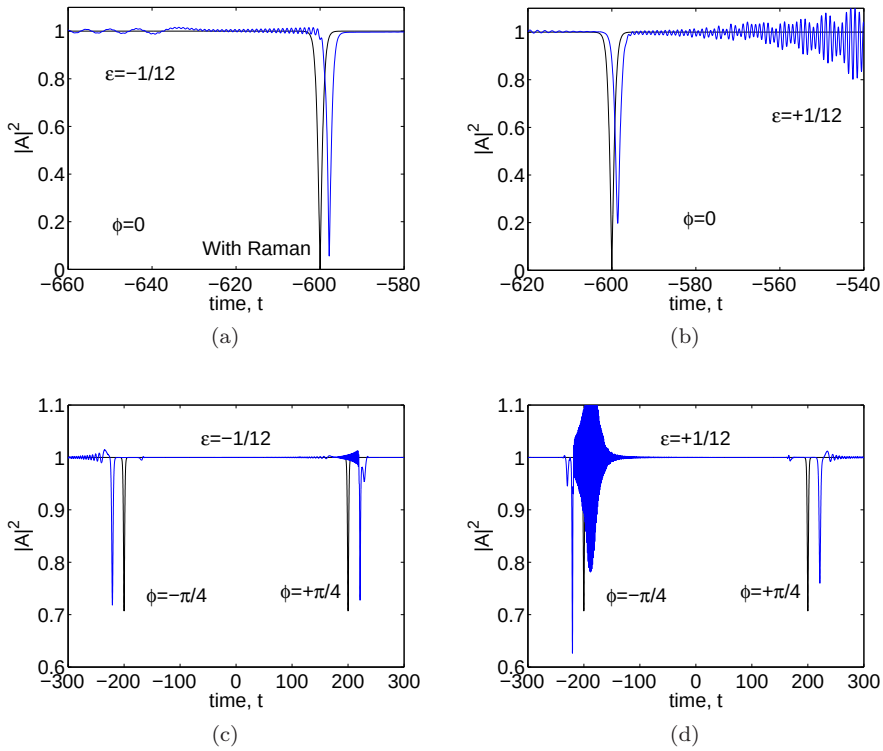

Figure 3.15: Perturbation of black (top) and grey (bottom) solitons under TOD and Raman after propagation distance of $30L_D$ in fibres with the different sign of ϵ.

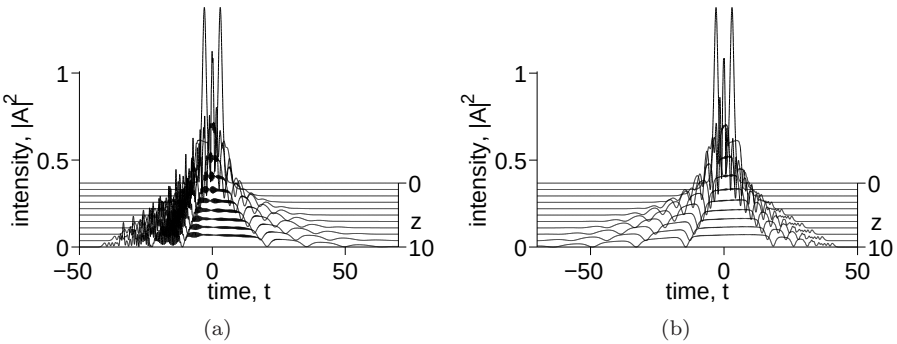

Figure 3.16: (a) Temporal evolution of the dark soliton train under Raman scattering and positive TOD. Here, $\epsilon = 0.0217$ and initial condition is $A = \sqrt{10}[sech(t-3) + sech(t+3)]$, with $T_0 = 100$fs. (b) is the same as (a), but $\epsilon = -0.0217$

$L_D = \frac{T_0^2}{|\beta_2|}$, the train will be generated before the higher order ones play a significant role. Fig.3.16 shows the evolution in time domain under Raman scattering and TOD. When $\epsilon > 0$, fig. 3.16a, the solitons start radiating and a continuum spectra is generated. Note that the solitons generated in the train tend to be black [Rothenberg91]. The ones radiating are the ones found for $t < 0$, which are the fast ones and hence spectrally closer to the zero GVD frequency, therefor expected to radiate stronger than the slow ones, found at $t > 0$. On the contrary, if $\epsilon < 0$, fig. 3.16b, Raman enhances the stability of the train because of the radiation suppression.

Figs.3.17a,b show the corresponding spectral evolution of the dark soliton train in fig. 3.16. As expected, when $\epsilon > 0$, there is a much stronger transfer of energy to the anomalous GVD region than in the $\epsilon < 0$ case. Absence of Raman scattering yields to the spectra in figs. 3.17c,d, which final states are compared with those with Raman in figs. 3.17e,f.

3.5 Conclusions: optimal supercontinuum

Cherenkov radiation is efficiently emitted buy dark solitons close to a zero GVD frequency with positive TOD, due to the Raman effect. Frequency and amplitude of the radiation is controlled by the soliton parameters, i.e., background amplitude, q, frequency, δ_s and greyness, ϕ. The latter one, can be easily controlled in realistic experiments with dark soliton trains by introducing a relative amplitude and phase between the input delayed bright pulses [Rothenberg91]. Besides, it plays a critical role in the radiation properties, since it provides a tuning in the continuum in such a way that spectral content is enhanced at the expense of the emitted radiation intensity, and vice-versa (see figs. 3.3a, 3.4a and 3.10 altogether). Regarding the spanning of the continuum, possibly the most crucial parameter is the number of dark solitons in the train that radiate efficiently (similar to the bright soliton order N), which is expected to be around half of them (see 3.16) and can be arranged from initial conditions (see e.g., [Finot06]). Thus, the problem of how to generate an optimised continuum, with the desired balance between spectral width and power, may be easily solved from the work developed here and remains opened for the future.

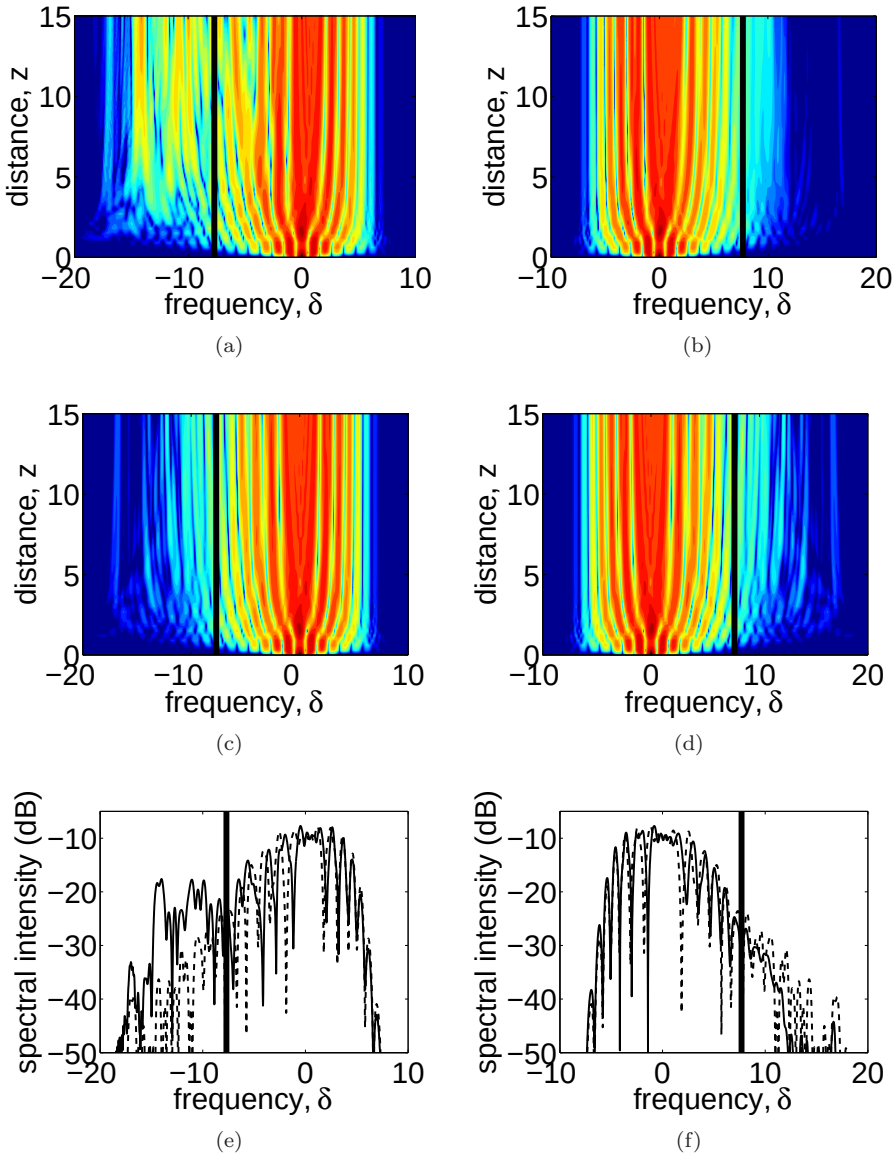

Figure 3.17: (a) and (b) are the spectral evolution of the dark soliton train in figs..3.16(a) and (b), respectively. (c) and (d) correspond to the absence of Raman effect and the output spectra with (full) and without (dashed) Raman are compared in (e) and (f). TOD is positive for the left column and negative for the right one.

Chapter 4

Polychromatic Cherenkov radiation and continuum generation in tapered fibres

In this second chapter about continuum spectra, we focus on bright solitons, which are extensively studied in the context of SC generation. As mentioned in chapter 1, the Cherenkov radiation associated to bright solitons in SC experiments is usually of very low intensity and highly monochromatic [Skryabin10], being necessary the use of input pulses with a peak power of the order of $\sim$ 10kW to achieve a big spectral broadening, which is constituted by the contribution of tens of solitons, each with their associated resonant radiation spectral peak. Here it is numerically investigated the spectral broadening of the Cherenkov wave emitted from a single fundamental bright soliton, for which the use of a tapered fibre becomes necessary.

Tapered optical waveguides with dispersion and nonlinear response varying along the waveguide length have been already considered for many applications, which include pulse compression [Travers07, Gérôme07], supercontinuum generation [Kudlinski06,Falk05], radiation trapping [Travers09], control of the soliton self frequency shift (SSFS) [Pant10, Judge09, Judge10] and blue-shift [Stark11b], for creating the effective amplification [Davoyan10] and parabolic pulses [Latkin07].

In most of the above cases the prime role of the taper is to keep the solitons energy and control their durations, while other effects follow from it. It is known that in SC generation, solitons in the spectral range of the anomalous GVD lose a little fraction of their energy into the dispersive waves emitted into the range of normal GVD [Skryabin10]. This emission is the so called Cherenkov radiation, which intensity is exponentially sensitive to the detuning of the soliton from the zero GVD

frequency [Biancalana04].

In this chapter it is demonstrated, merely by means of numerical simulations, that a single fundamental soliton in a tapered fibre can develop a spectrally broad tail of the intense polychromatic Cherenkov radiation, forming a homogeneous continuum. Conversely to the applications above, the effect presented here requires the soliton to lose a significant fraction of its energy. This becomes possible, because tapering provides conditions for maintaining small spectral gap between the Raman shifting pulse and the zero GVD point, thus efficiency of the Cherenkov radiation remains high over long propagation distances.

The text below is structured as follows. The first part, section 4.1 introduces the Cherenkov radiation for bright solitons. Some properties of the tapers studied here are described in 4.2. Section 4.3 focuses on the first zero GVD point ($\epsilon > 0$) and 4.4 on the second one ($\epsilon < 0$). It is observed that depending on the input pulse power and tapering, the radiation can be emitted either as a train of pulses or as a wide and strongly chirped pulse. In the latter case, the radiation can be compressed using a piece of fibre with suitably designed dispersion profile, as explained in section 4.5.

4.1 Bright solitons and Cherenkov radiation

Resonance condition for bright solitons in the proximity of a zero GVD can be found by following exactly the same procedure of chapter 3 [Biancalana04]. Briefly, eq. 3.1 with the negative sign for the GVD term $\sim \partial_t^2$ together with the ansatz eq. 3.2 yields to eq. 3.3 with $d = -1 + 6\epsilon\delta_s$, $d < 0$ yielding to anomalous GVD, which bright soliton solution is

$$F = \sqrt{2q}Sech(\sqrt{\frac{2q}{-d}}\xi). \tag{4.1}$$

Also, same expression for eq. 3.8 is recovered, however the asymptotic analysis yields to the operator $\hat{L}_\infty$ having zero off-diagonal terms and the null determinant condition $\mathcal{W}_\infty(\Omega)\mathcal{W}_\infty(-\Omega) = 0$ ($\Omega \equiv \delta_s - \delta$), where $\mathcal{W}_\infty(\Omega) \equiv \epsilon\Omega^3 - \frac{d}{2}\Omega^2 + q$, is the third order polynomial

$$q = \frac{d}{2}\Omega^2 - \epsilon\Omega^3. \tag{4.2}$$

The only real root of eq. 4.2, δ_r, is located in the normal GVD regime at a separation from the zero GVD frequency such that $|\delta_r - \delta_{zGVD}| \gtrsim 2|\delta_s - \delta_{zGVD}|$. Condition eq. 4.2 has the meaning of phase matching between the soliton with propagation constant $k_s \equiv \beta_0 + \beta_1(\omega - \omega_0) + \frac{1}{2}\gamma P_0$ and the linear waves (on top of zero background,

since bright soliton tails decay to zero), with $k_l \equiv \beta_0+\beta_1(\omega-\omega_0)+\sum_{j=2}^{J}\beta_j(\omega-\omega_0)^j/j!$, where β_0, β_1 are, respectively, the propagation constant and the inverse group velocity of the linear fibre mode at ω_0. This matching reads

$$\frac{\gamma P_0 L_D}{2} = \frac{-1}{2}(\omega-\omega_0)^2 T_0^2 + \epsilon(\omega-\omega_0)^3 + L_D \sum_{j\geq 4}\frac{\beta_j}{j!}(\omega-\omega_0)^j, \tag{4.3}$$

which is equivalent to eq. 4.2 with the arbitrary parameter $\delta_s = 0$, $q = \gamma P_0 L_D/2$ plus the sum over j, which accounts now for the whole linear fibre dispersion. An example of the phase matching diagram, analogue to fig. 3.2, is shown in fig. 4.1c. The straight horizontal line is the soliton dispersion at the input wavelength $\lambda_0 = 2\pi c/\omega_0 = 800nm$, and the cubic curve the dispersion of the linear fibre modes, around the first zero GVD point ($\epsilon > 0$).

Figs.4.1a,b show typical Cherenkov radiation emission by a fundamental bright soliton under perturbation of TOD and Raman effects. Raman effect quickly shifts the soliton spectrum away from the zero GVD point, and thereby suppresses transfer of energy from the soliton to the radiation. Hence the Cherenkov spectrum remains weak and narrow band (centred around $\lambda \approx 760$nm) due to the critical dependence of the radiation amplitude with $|\omega_s - \omega_{zGVD}|$ [Biancalana04, Skryabin10]. Grey lines in fig. 4.1c represent k_s of the red shifting soliton after some propagation and show how the resonant radiation frequency shifts away from the zero GVD point ($d^2k_l/d\lambda^2 \equiv 0$).

4.2 Tapered fibres

Reproducing the derivation of the GNLSE in chapter 2 for fibres with varying cross section along z, assuming that this variation is smooth enough so reflections and losses are negligible, one obtains the adiabatic GNLSE [Travers09, Judge09], which is equivalent to eq. 2.32 but with slowly varying coefficients. Neglecting the nonlinear dispersion, it reads

$$-i\partial_z A(z,t) = \sum_{j\geq 2}^{J}\frac{\beta_j(z,\omega_0)}{j!}(i\partial_t)^j A(z,t) + \gamma(z)A(z,t)\int_{-\infty}^{+\infty} dt' R(t')\left|A(z,t-t')\right|^2. \tag{4.4}$$

z-variations of β, and its ω derivatives, are accounted for through the GVD and higher order dispersion coefficients only. This provides a reasonable approximation, since in the tapers considered below the relative changes of $\beta_{0,1}$ along the relevant lengths are $\sim 1\%$, while $\beta_{2,3}$ for a fixed frequency can vary by $\sim 50\%$ and more, as

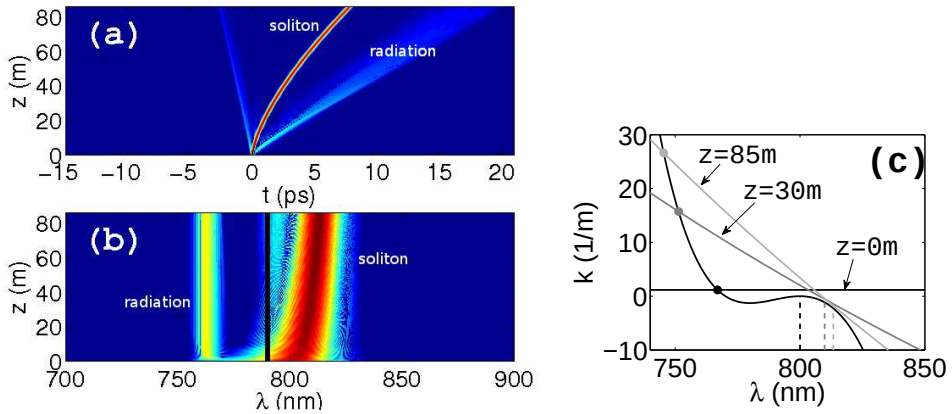

Figure 4.1: Radiation emission by a fundamental soliton in a uniform fibre. Propagation distance is $z \approx 85$m and $\gamma \approx 0.072$/W/m at the pump wavelength $\lambda_0 = 800$nm. (a) time domain and (b) spectral dynamics. The zero GVD wavelength, $\lambda_{zGVD} = 790$nm, is marked by the black line and the fibre radius is $r \approx 1.29\mu$m. (c) Matching between the soliton spectrum (straight lines) and the linear modes (curve) for selected propagation distances. The thick dots mark the resonant radiation wavelength and the dashed lines the instantaneous soliton carrier.

shown in fig. 4.2.

The linear fibre mode profiles, $\overrightarrow{E}, \overrightarrow{H}$, have been used to compute the nonlinear fibre parameter, γ (given in eq. 2.38),

$$\gamma = \epsilon_0^2 \omega_0 c \frac{\epsilon \int\int dxdy\; n_2(x,y) \frac{2}{3} \left[\left| \overrightarrow{E} \right|^4 + \frac{1}{2} \left| \overrightarrow{E}^2 \right|^2 \right]}{\left[\int\int dxdy \mathrm{Re} \left\{ \overrightarrow{E} \times \overrightarrow{H^*} \right\} \hat{u}_z \right]^2}, \tag{4.5}$$

where ϵ is the dielectric permittivity of glass at ω_0, $\hat{u}_z$ is the unitary vector along the z axis, x and y are the transverse coordinates, $n_2 = 2.6 \times 10^{-20} m^2$/W the nonlinear index of silica glass, and c the speed of light in vacuum, which permittivity is ϵ_0.

Using numerical data for silica strands with the core radius varying in steps of 0.1μm, we have interpolated the dispersion coefficients, β_j (up to $J = 11$), and nonlinearity, γ. Initial conditions for modelling eq. 4.4 have been taken in the form $A(z = 0, t) = \sqrt{P_0} sech\,(t/T_0)$ (see eq. 2.35), where $T_0 = 30$fs is the initial soliton width, the peak power is $P_0 = N^2 |\beta_2| / \gamma T_0^2$ and N is the soliton order.

Fig.4.3 shows the dispersion, $D = -2\pi c \beta_2 / \lambda^2$, and nonlinearity, γ, around the pump wavelengths used around the two zero GVD points, which are considered separately in the next two sections.

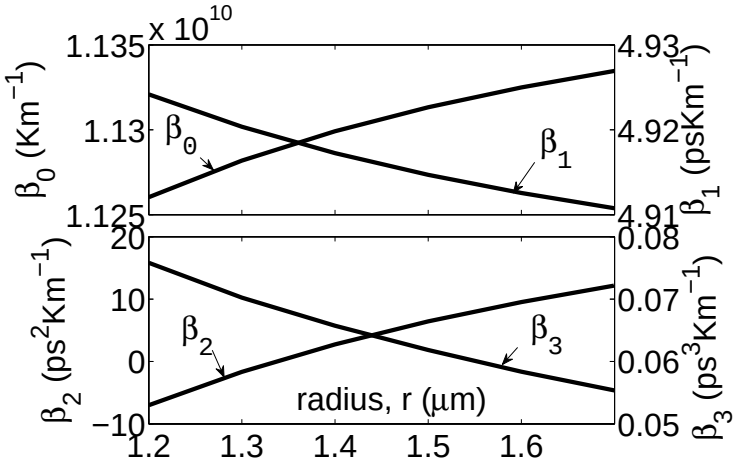

Figure 4.2: Variation of the first four dispersion coefficients evaluated at $\lambda_0 = 800$nm as a function of the fibre radius.

4.3 Cherenkov continuum with positive TOD

Replacing the uniform fibre in fig. 4.1 by a taper with the increasing radius, gradually shifts the zero GVD point ($d^2k_l/d\lambda^2 \equiv 0$) towards smaller frequencies, see fig. 4.3a, and detuning between the spectrally shifting soliton and the zero GVD can be arranged to remain relatively small. Figs.4.4a,b show the radiation emission in this case. The boost in the radiation intensity is obvious, but, importantly, its spectrum broadens significantly and forms the 50nm wide and homogeneous continuum, see fig. 4.4b. Note, that by the conservation of energy, the intense radiation emitted by a soliton creates the radiation pressure on the soliton and thereby changes its frequency (spectral recoil effect) [Akhmediev95]. Typical dispersion, D, considered here (fig. 4.3a) yields to blue shifted radiation, and hence the recoil on the soliton from the emission process shifts the soliton frequency further to the red, which adds up to the frequency shift produced by the Raman effect [Skryabin10]. The recurrent recoils and the enhanced Raman shift due to the smallness of $|\beta_2|$ [Gordon86] result in a redder soliton in the tapered case, what is favourable for spreading the radiation spectrum over a wider range.

Changes of the soliton detuning from the zero GVD point along the fibre length is the key feature controlling spectral content and efficiency of the Cherenkov radiation. Fig.4.5 shows the propagation along three different tapers of length $z \approx 17$m in which the initial conditions are identical to those in figs. 4.1 and 4.4, but the zero

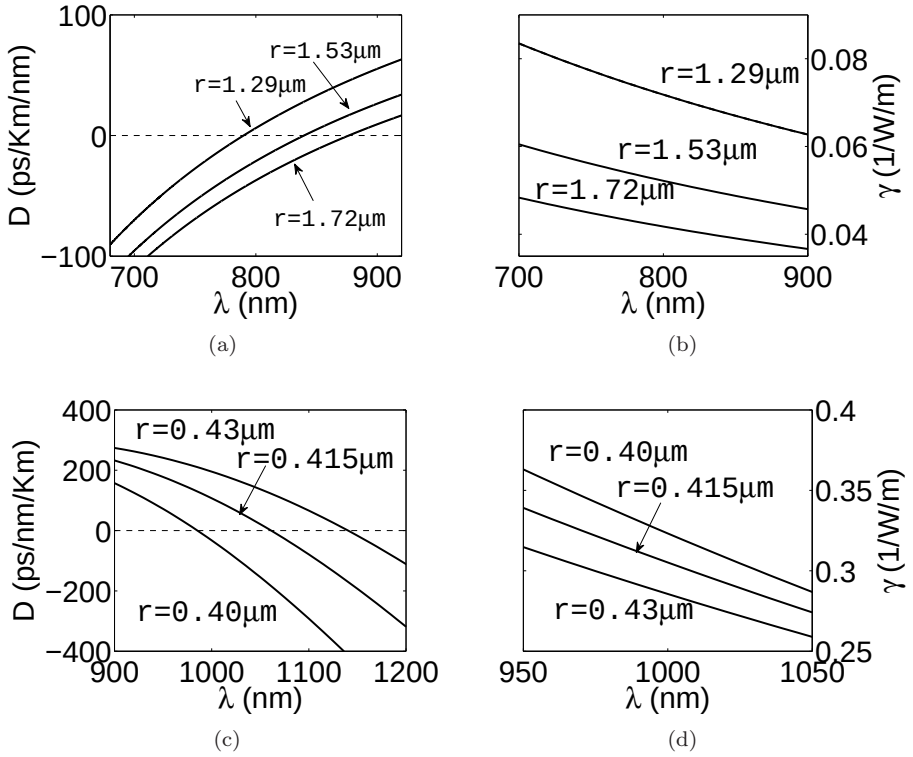

Figure 4.3: (a,c) Dispersion and (b,d) nonlinearity for several fibre radii. Values shown are around the lower (a,b) and higher (b,d) zero GVD wavelengths, for which the pumps are taken at $\lambda_0 = 800$nm and $\lambda_0 = 1000$nm, respectively. For the lower zero GVD, the smallest radius corresponds to the initial conditions of figs. 4.1, 4.4 and 4.5 and the other two, in increasing order, to the final cross sections of figs. 4.4 and 4.7(b), respectively.

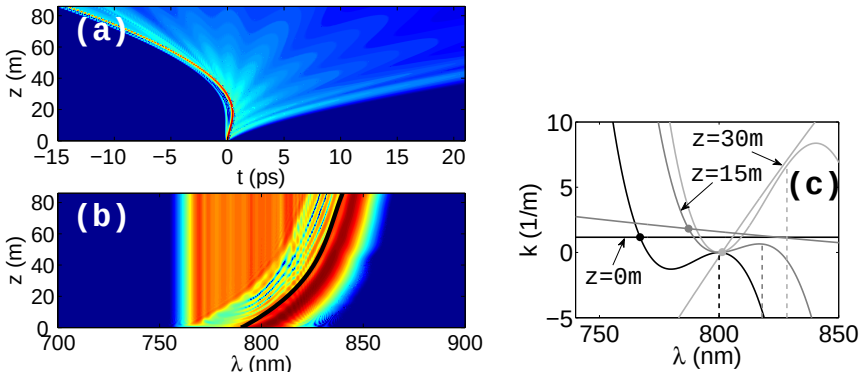

Figure 4.4: Radiation emission by a fundamental soliton in a tapered fibre. Initial conditions and fibre length are identical to those of fig. 4.1. The final radius is $r \approx 1.53\mu$m and the zero GVD wavelength is marked by the black line (see also fig. 4.6b).

GVD point and fibre radius achieve three different final values, shown in fig. 4.6. Fig.4.5a corresponds to the geometry, which shifts the zero GVD towards redder frequencies at the rate which is faster than the soliton self-frequency shift. In this case, there is a periodic increase and decrease of the detuning of the soliton from the zero GVD point, and therefore intensity of the Cherenkov radiation is modulated in time. This modulation happens because the recoil on the soliton from the intense radiation temporarily accelerates the net red shift of the soliton frequency, and hence leads to the drop in the radiation emission. With the weakening recoil, the detuning between the soliton and the zero GVD point starts to narrow again, which amplifies the radiation and the cycle is repeated. By slightly increasing the rate of tapering, as in figs. 4.5b,c, we can ensure that the zero GVD point moves fast enough, so that it catches up not only with the bare soliton self-frequency shift, but also with the addition from the recoil contribution. Then the latter does not adversely impact the radiation intensity as much and the modulations smooth over giving a homogeneous plateau in the spectrum and a strongly chirped radiation pulse in time domain. In this case, however, most of the soliton energy is transferred to the radiation over shorter propagation distances.

Note that the polychromatic Cherenkov radiation effect is somehow similar to the linear effect of the rainbow storage [Tsakmakidis07] in a metamaterial core waveguide. In both cases a continuous range of frequencies is *extracted* from a light pulse and slowed down, being the extraction controlled by the waveguide width. In the rainbow

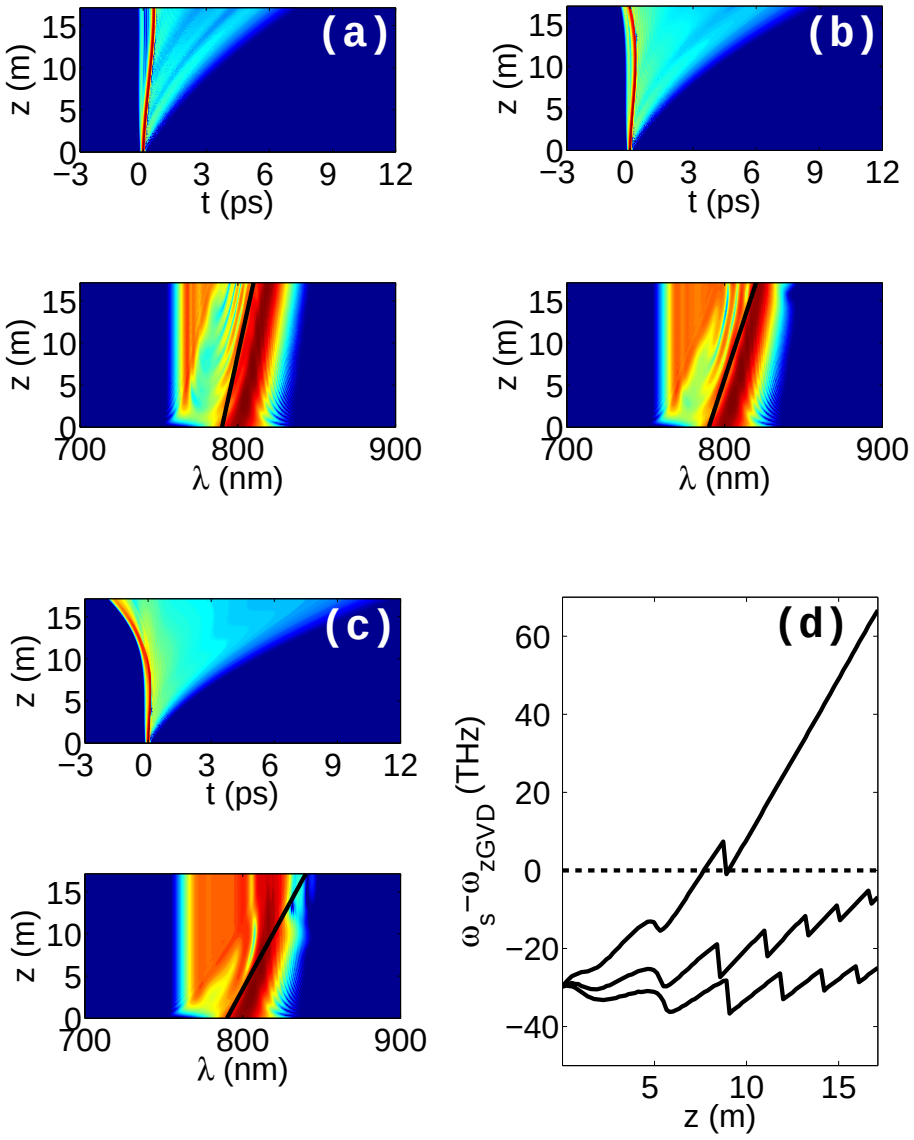

Figure 4.5: Fundamental soliton along $\sim$ 17m of several tapered fibres. The fibre in (a) keeps constant in average the soliton detuning with the zero GVD wavelength (as in fig. 4.4), whereas those in (b) and (c) increase λ_{zGVD} and r faster (see figs. 4.6a,b), showing single pulse emission. The detuning in frequency is monitored in (d) for the three cases, corresponding the bottom line to (a) a the top one to (c).

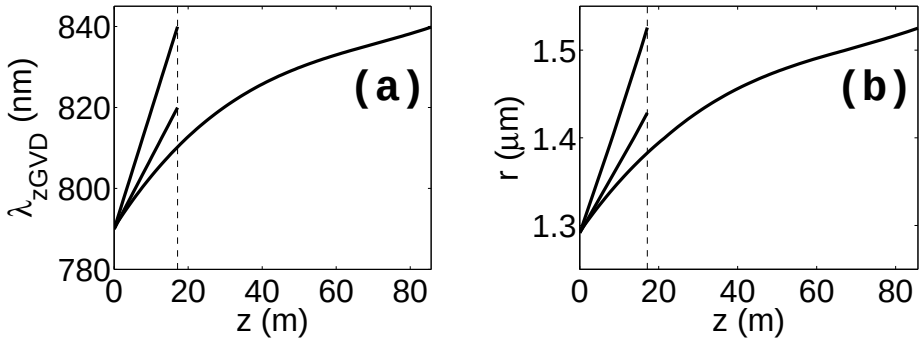

Figure 4.6: (a) and (b) show, respectively, the variation of the zero GVD wavelength and radius along z corresponding to the tapers in fig. 4.4b (lines up to $z = 85$m) and 4.5a-c (lines up to $z = 17$m only).

effect all the frequency components are gradually slowed down at the same time, coupling each of them to a slower modes of the tapered waveguide. In our case, the frequency to extract is selected by the Cherenkov resonance, which slows down progressively as the waveguide radius increases.

4.3.1 Higher order solitons

Increasing the initial power beyond the power corresponding to the $N = 2$ soliton in a uniform fibre, the pulse breaks up into several solitons, with most of the power absorbed by the firstly ejected soliton, which duration is reduced well below the input pulse one [Dudley06, Skryabin10]. Fig.4.7a shows the $N = 5$ input conditions for $\lambda_0 = 800$nm in a uniform fibre with $\lambda_{zGVD} = 795$nm and 4m length. Fig.4.7b shows dynamics of the same input pulse, but in a tapered fibre which radius and zero GVD wavelength are plotted in fig. 4.8. The radiation emission in the tapered case is much larger and splitting of the input pulse into fundamental solitons is largely suppressed, so that the dynamics we observe is similar to the single soliton excitation shown in figs. 4.4 and 4.5a,b, but the radiation tail is more powerful, the associated continuum much broader and it develops over a shorter length scale. When $N \geq 2$ sharp spectral gaps appear (see fig. 4.7b at $\lambda \approx 800$nm) which correspond to a train of pulses in time domain. They arise because the $\sim N^2$ times higher spectral content of the resonant frequency in the initial Nth order soliton spectrum yields to a bigger boost of energy into the Cherenkov radiation and hence to a stronger recoil effect [Akhmediev95], that quickly detunes the soliton from λ_{zGVD}.

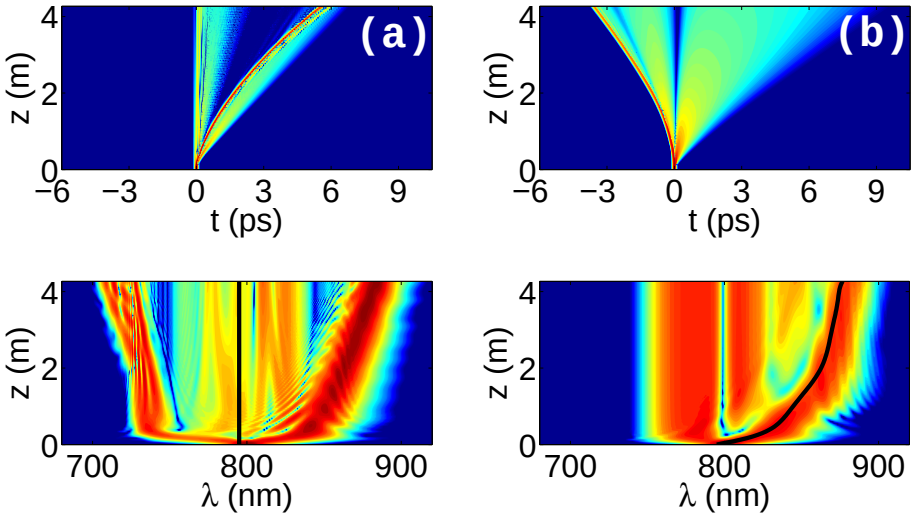

Figure 4.7: Fifth order solitons propagating in (a) non tapered and (b) tapered fibres along $z \approx 4$m. Black lines mark the zero GVD wavelengths, which start in both cases at $\lambda_{zGVD} = 795$nm.

Temporal and spectral modulation of the radiation is seen to be small in figs. 4.5b,c, and the Cherenkov band broadens continuously. Figs.4.5a and 4.4b present some modulation and fig. 4.7b shows clear discrete jumps in the radiation spectrum. These continuous or discrete spectral development of the radiation is analogue to that of the radiation in uniform fibres, when it is trapped by a soliton or bounces with it [Skryabin10], respectively, depending on their relative power. The important difference between these effects in uniform and tapered fibres is that, whereas in the former the soliton collides back with the emitted radiation, erasing the Cherenkov spectral history, in the latter the emitted radiation propagates away from the soliton despite the Raman effect (see fig. 4.4a) and its frequency will add up into the spectrum formed by the subsequently emitted Cherenkov waves.

4.4 Cherenkov continuum with negative TOD

When the soliton spectrum is close to the second zero GVD wavelength the slope $dD/d\lambda$ changes from positive to negative, as shown in fig. 4.3c. To simulate the emission of dispersive waves emission at the second zero GVD wavelength, a fibre

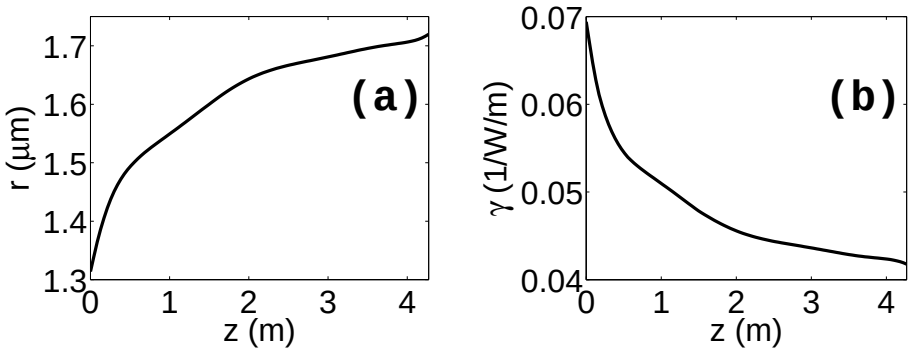

Figure 4.8: (a) Zero GVD wavelength and (b) radius of the taper in fig. 4.7b.

with $\lambda_{zGVD} = 1050$nm, $r \approx 425$nm, and $\gamma \approx 0.31$/W/m at the pump wavelength, $\lambda_0 = 1\mu$m is considered.

Physically, the most relevant difference from the $dD/d\lambda > 0$ case is that Raman red shift and spectral recoil shift push the soliton spectrum in opposite directions so they cancel to each other in uniform fibres [Gorbach07], as in fig. 4.9a. In this situation, a polychromatic radiation tail filling the spectral gap between the soliton and the radiation can be easily generated by smoothly decreasing the fibre cross section, what increases ω_{zGVD} and ω_r. Figs.4.9b, 4.9c and 4.9d show the evolution of the spectral steady state in $z = 40L_D \approx 76.7$cm along tapers with linearly interpolated ω_{zGVD}. Comparison between figs. 4.9b and 4.9c shows how the bandwidth is increased by increasing the $\lambda_{zGVD}(z)$ slope whilst keeping the taper length to $20L_D$, whereas the bandwidth remains the same when the taper length is increased to $40L_D$ but the final λ_{zGVD} value is fixed, as in figs. 4.9c and 4.9d. This happens because the spectral recoil and Raman shift are balanced so the soliton does not experience sudden jumps in ω_s, what makes the radiation to be broadened continuously, implying that the bandwidth depends mainly on the initial and final values of $\lambda_{zGVD}(z)$ and not on the taper length. Matching between soliton and radiation along the evolution of fig. 4.9 is explicitly shown in fig. 4.10a for $z = 0, 40L_D$ and in 4.10b for the final states of the tapered fibres. An important observation here is that the spectral recoil effect is eventually stronger than Raman effect in the proximity of the zero GVD, yielding the former one to the soliton blue shift seen in figs. 4.9b-d (and 4.10b), effect that has been reported in recent experiments [Stark11b].

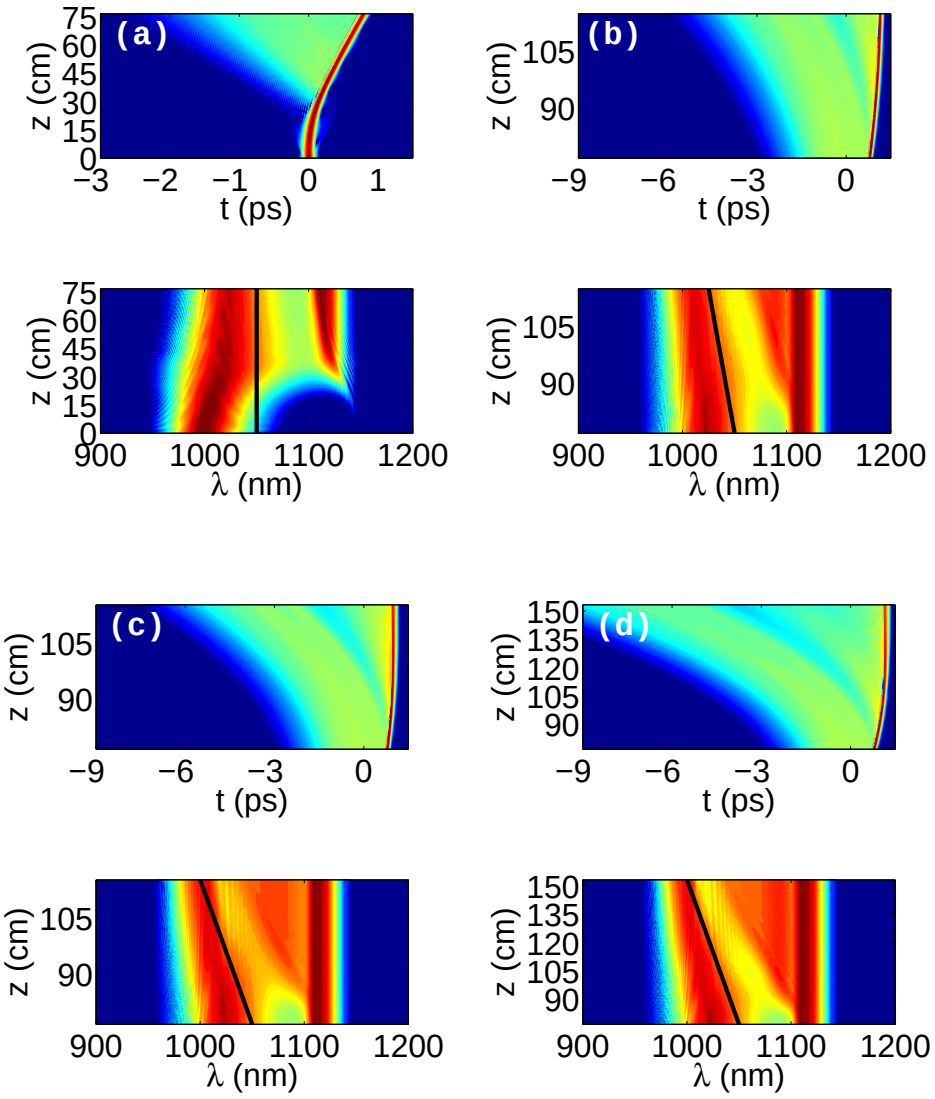

Figure 4.9: Fundamental soliton propagating close to the second zero GVD wavelength. 4.9a shows the first $40L_D$ in a non tapered fibre with $\lambda_{zGVD} = 1050$nm ($r = 424.9$nm), where the soliton reaches the Raman self frequency shift cancellation state. Further propagation is shown by tapering the fibre from $z = 40L_D$ to reach the final values of (b) $\lambda_{zGVD}(60L_D) = 1025$nm ($r = 415.3$nm), (c) $\lambda_{zGVD}(60L_D) = 1000$nm ($r = 405.6$nm) and (d) $\lambda_{zGVD}(80L_D) = 1000$nm.

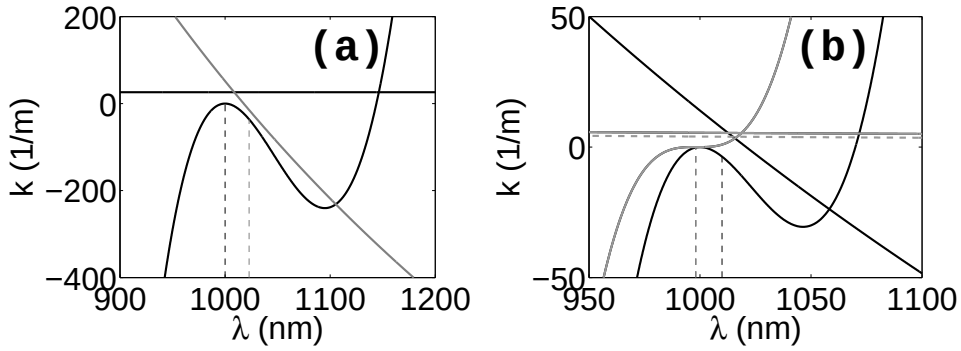

Figure 4.10: Matching between soliton (straight lines) and linear waves (curves) propagation constants. (a) corresponds to initial (horizontal) and final (inclined) conditions of fig. 4.9a. (b) shows matching at the end of the evolution in 4.9b (black) and 4.9c,d (grey). The horizontal dashed line corresponds to the lower power soliton at $z \approx 1.5m$ of 4.9d. Soliton instantaneous carrier is marked by the vertical dashed lines.

4.5 Compression of the radiation pulses

When the resonant radiation is emitted continuously a single pulse is formed and it can be efficiently compressed by a suitably designed fibre which dispersion compensates the non trivial chirp of the multicolour tail. As an example, we consider the compression of the final field of fig. 4.4b ($z = 200L_D$). The phase space of the Cherenkov tail is shown in fig. 4.11a through the spectrogram function, computed as $S(\omega-\omega_0,t) = |\int_{-\infty}^{\infty} dt' A(t'/T_0)Sech([t'-t]/T_0)e^{-i(\omega-\omega_0)t}/T_0|^2$, from where a simple polynomial fitting gives us the chirp in the form $t(\omega-\omega_0) = \sum_{j=1}^{J} C_{j-1}(\omega-\omega_0)^{j-1}$ (dashed curve). Compression is achieved if all the linear waves in the tail overlap in a given time, t_{ref}, after certain fibre length, Δz, what implies that the inverse group velocity of each of these waves needs to satisfy $\beta_1(\omega-\omega_0) = -\left[t(\omega-\omega_0) - t_{ref}\right]/\Delta z$. Substituting in this expression the polynomial expansions of $\beta_1(\omega-\omega_0) \equiv \sum_{j=1}^{J} \beta_j(\omega-\omega_0)^{j-1}/\left[j-1\right]!$ and $t(\omega-\omega_0)$, and comparing term by term results in the following expression for the dispersion coefficients of the fibre

$$\beta_j(ps^j/Km) = -\frac{[j-1]!}{\Delta z(Km)}\left[C_{j-1}(ps^j) - t_{ref}(ps)\delta_{j1}\right], \tag{4.6}$$

where $j : 1 \rightarrow J$ and δ_{jk} is the Kronecker symbol. Note that there is an infinite number of linear fibres satisfying the compression condition eq. 4.6 because the β_j's can be modified by setting different values of Δz and t_{ref}. By choosing $t_{ref} = 0$ps

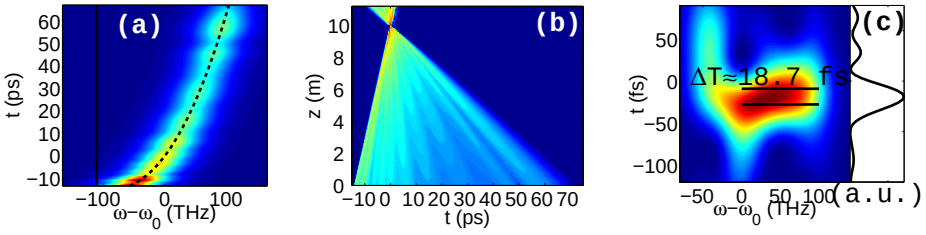

Figure 4.11: (a) Cherenkov radiation spectrogram corresponding to the final field of fig.2b. Vertical line marks the zero GVD frequency and the dashed line the polynomial fit $t(\omega - \omega_0)$. The compression in time domain is shown in (b) and the spectrogram of the compressed state is in (c).

and $\Delta z = 10$m the linear dispersion of the compression fibre is approximately given by $\beta_2 = -36.16ps^2/\text{Km}$, $\beta_3 = -0.48ps^3/\text{Km}$, $\beta_4 = 17 \times 10^{-2}ps^4/\text{Km}$ and $\beta_5 = 10^{-5}ps^5/\text{Km}$ at the pump frequency. The compression occurs as shown in fig. 4.11b and the resulting pulse has a width $\Delta T = 18.7$fs, which is shorter than the input soliton of $T_0 = 30$fs (see fig. 4.11c). This could find applications in ultra short pulse generation from a polychromatic Cherenkov tail.

4.6 Conclusions: further optimisation

The effect shown numerically in section 4.3 are the result of a simple numerical optimisation of the optical fibre, according to the input pulse parameters, which is done automatically by the numerical code. The latter is programed to keep the soliton carrier at a fixed distance from the moving zero GVD frequency, readjusting linear and nonlinear parameters at each step. Generation of polychromatic Cherenkov radiation provides a method to flatten the SC spectra, often desired for some applications (see e.g., [Vukovic10]). Besides, the low power required lets operate the laser source at higher repetition rates, useful in real time measurements.

On the contrary, effects in 4.4 happen easily, being the only requirment that the zero GVD frequency is blue-shifted with propagation, hence recoil effect yields to the soliton blue-shift [Stark11b]. However, some taper designs may be used around the second GVD wavelength ($\beta_3 < 0$) to optimise spectral extension towards the IR. An interesting problem is the one of maximising the soliton red-shift that moves close to the zero GVD [Judge09]. This requires a compromise between the soliton and zero GVD spectral distance, because smallness of $|\beta_2|$ enhaces red-shift [Gordon86], but

also induces soliton power depletion through the emission of radiation. Moreover, if the soliton has trapped some of its radiation at the long-wavelength side, further IR extension is expected. Note that, a soliton can only trap its own radiation through the second GVD wavelength in a tapered fibre that modifies the soliton-radiation relative group velocity. Trapping accross this point in a uniform fibre must invlove more than one soliton, i.e., a soliton can only trap radiation that has been emitted by a different soliton that is closer to the zero GVD [Chapman10].

Chapter 5

Nonlinear switching in subwavelength semiconductor on metal plasmonic waveguides

The aim of this chapter is to demonstrate numerically the nonlinear switching in planar arrays of two and three coupled plasmonic waveguides. Nonlinear switching is known as the state in which, above the threshold power, the light stops being transferred from one waveguide to another and most of it stays in the initially excited waveguide. This effect has led to flourish of activities related to discrete optical solitons [Aceves96, Lederer08] dominantly focused, until recently, on waveguides with cross sections significantly larger than the light wavelength.

The plasmonic waveguides considered here are AlGaAs semiconductor wires placed on top of silver substrate, hence surface plasmon polaritons (SPP's) at the metal-semiconductor interfaces provide tight confinement of electromagnetic energy. As a consequence, the nonlinear response is shown to boost with respect to the waveguides placed on top of glass substrate, which use only total internal reflection (TIR) guidance, and hence the switching can be achieved with much lower power levels. This enhancement of the nonlinearity by the metal has been already shown in the context of metal nanowires by [Ye10]. The strong vectorial nature of the plasmonic modes requires modelling tools that allow for solving vectorial Maxwell equations, which can be done in 2 and 3D by using the finite element analysis (FEA) [Szabo91], implemented in Comsol.

This type of plasmonic waveguides have been proposed recently [Krasavin10] and studied in the linear regime only. The importance of accounting for the Ohmic losses introduced by the metal will require an optimal choice of the waveguide parameters in order to demonstrate the nonlinear switching along a propagation distance of a loss length [Milián11]. The two photon absorption (TPA) losses are avoided here by the choice of the AlGaAs semiconductor because, conversely to silicon, it can be arranged for the Telecom wavelength $\lambda = 1550$nm, used here, to be just below the half band gap [Aitchison97].

The chapter is structured as follows. Section 5.1 is devoted to theoretical and numerical analysis of the two and three waveguides arrays, using the coupled waveguides equations derived in chapter 2. The concept of linear SPP waves is briefly introduced in section 5.2. 5.3 discusses the linear and nonlinear properties of the modes in terms of wavelength and waveguides geometry. Finally, section 5.4 presents the numerical results of the 3D propagation simulations in the optimal arrays, where the nonlinear switching is shown.

5.1 Nonlinear coupled oscillator model

The systems of two and three coupled waveguides are analysed theoretical and numerically in this section, using the nonlinear oscillator model provided by the DNLSE (eq. 2.63), assuming that the individual waveguides are single mode, so the N-waveguides array has N linear modes.

5.1.1 Directional coupler

In the particular case of two coupled waveguides, also called directional coupler [Jensen82], eq. 2.63 reads

$$\begin{aligned} -i\partial_z A_1 &= \kappa A_2 + \gamma |A_1|^2 A_1 \\ -i\partial_z A_2 &= \kappa A_1 + \gamma |A_2|^2 A_2, \end{aligned} \tag{5.1}$$

which analytical solutions are found in the form $A_{1,2} = a_{1,2} e^{i\phi_{1,2}(z)}$ ($a_{1,2}, \phi_{1,2} \in$ Re), giving

$$\begin{aligned}
&\sin(\phi_2-\phi_1)=0\\
&\dot{\phi}_1=\kappa\frac{a_2}{a_1}e^{i(\phi_2-\phi_1)}+\gamma|a_1^2|\\
&\dot{\phi}_2=\kappa\frac{a_1}{a_2}e^{-i(\phi_2-\phi_1)}+\gamma|a_2^2|.
\end{aligned}\tag{5.2}$$

Because the first equation implies $\phi_2(z)-\phi_1(z)=m\pi, m=0,\pm1,\pm2,...$ the last two reduce to

$$\dot{\phi}_2-\dot{\phi}_1=\kappa[\frac{a_1}{a_2}-\frac{a_2}{a_1}]\cos(m\pi)+\gamma[a_2^2-a_1^2]=0,\tag{5.3}$$

which can be rearranged as

$$[a_2^2-a_1^2][a_1+\frac{\kappa}{\gamma a_2}\cos(m\pi)]=0\tag{5.4}$$

and the three solutions are

$$a\equiv a_1=\pm a_2, \phi\equiv\phi_{1,2}=q_\pm z\equiv[\pm\kappa+\gamma a^2]z\tag{5.5}$$

$$a\equiv a_1=\frac{\kappa}{\gamma a_2}, \phi\equiv\phi_{1,2}=q_s z\equiv[\gamma a^2+\frac{\kappa^2}{\gamma a^2}]z,\tag{5.6}$$

where the total mode power is $P\approx a_1^2+a_2^2$. Solutions in eq. 5.5 are the symmetric, $\Psi_+(z)$, and antisymmetric, $\Psi_-(z)$, modes of the linear coupler, plus the wavenumber shift, γa^2, accounting for nonlinearity induced phase shift. In the linear regime, their relative phase rotates over an angle 2π along a propagation distance equal to π/κ, being half that distance the so called coupling length $L_c\equiv\pi/(2\kappa)$, along which the power is transferred from one waveguide to another. The coupling constant, defined in eq. 2.59 for $j=1$, reads

$$\kappa=\frac{\left[\beta_s^2-\beta_0^2\right]}{2\beta_s}\int_S\overrightarrow{F}^*_{1s}\overrightarrow{F}_{2s}=\frac{\left[\beta_a^2-\beta_0^2\right]}{2\beta_a}\int_S\overrightarrow{F}^*_{1a}\overrightarrow{F}_{2a},\tag{5.7}$$

where β_0, β_s, β_a are the propagation constants of the single channel, Ψ_+, Ψ_- modes, respectively. Eq. 5.5 implies that $\int_S\overrightarrow{F}^*_{1s}\overrightarrow{F}_{2s}=-\int_S\overrightarrow{F}^*_{1a}\overrightarrow{F}_{2a}$ and then $\kappa=\frac{1}{2}(\beta_s-\beta_a)$, or $\kappa=\frac{1}{2}\mathrm{Re}(\beta_s-\beta_a)$ [Agrawal08] if there are losses in the system, as considered from now on.

The soliton-like solution eq. 5.6 does not exist below $P_s=2\kappa/\gamma$ ($a_1=a_2=\sqrt{\kappa/\gamma}$). Above $P=P_s$, most of the soliton amplitude localises in one waveguide (see

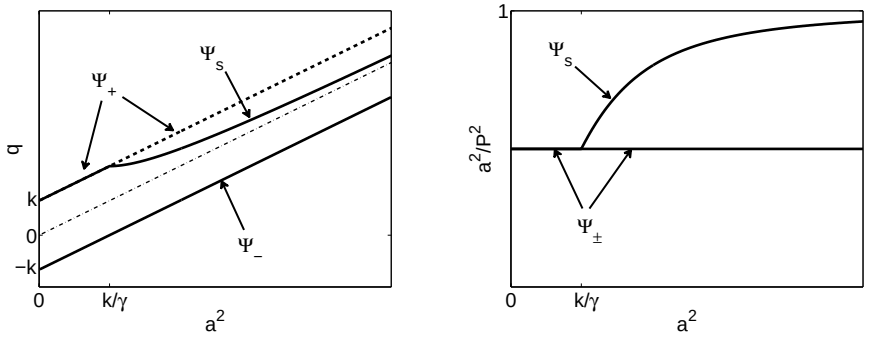

(a) (b)

Figure 5.1: (a) Phases of the directional coupler nonlinear solutions and (b) power ratio between the two channels as a function of the power in the channel that retains most of the light in the soliton case.

fig. 5.1b) and thus its phase asymptotically tends to that of the single waveguide mode $\gamma a^2 = \gamma P$ (see fig. 5.1a), compensating then for the split $\pm\kappa$ introduced by the linear coupling. This solution appears at a local bifurcation from the $\Psi_+(z)$-branch [Wiggins90] (see fig. 5.1), and thus it is associated to the instability of the symmetric mode. Hence, threshold power, P_{th}, for Ψ_s excitation, when pumping only one channel, can be easily calculated by stability analysis of $\Psi_+(z)$ under small perturbations. The system eq. 5.1 can be rewritten in terms of the superposition $A_\pm \equiv \frac{1}{2}[A_1 \pm A_2]$ $(A_{1,2} > 0)$, as

$$\begin{aligned} -i\partial_z A_+ &= +\kappa A_+ + \gamma\left\{A_+[|A_+|^2 + 2|A_-|^2] + A_+^* A_-^2\right\} \\ -i\partial_z A_- &= -\kappa A_- + \gamma\left\{A_-[|A_-|^2 + 2|A_+|^2] + A_-^* A_+^2\right\}. \end{aligned} \tag{5.8}$$

Substitution of $A_+ = \Psi_+ + \epsilon_+$ and $A_- = \epsilon_-$ in the system above results in uncoupled equations for the perturbations, satisfying the antisymmetric ones

$$-i\frac{d}{dz}\begin{bmatrix} \epsilon_- \\ \epsilon_-^* \end{bmatrix} = \begin{bmatrix} -\kappa + 2\gamma|\Psi_+|^2 & \gamma\Psi_+^2 \\ -\gamma\Psi_+^{2*} & \kappa - 2\gamma|\Psi_+|^2 \end{bmatrix}\begin{bmatrix} \epsilon_- \\ \epsilon_-^* \end{bmatrix}. \tag{5.9}$$

Null determinant condition gives the two solutions for the power $|A_+|^2 = \kappa/(3\gamma)$, κ/γ. The physical meaning, if any, of the former solution is not understood here, but the latter one yields to the well known result that the symmetric mode becomes unstable when the power in one channel is above the bifurcation in fig. 5.1, $a^2 = \kappa/\gamma$, corresponding also to the point $q_- = 0$ (see eq. 5.5). The single channel

excitation can be regarded as a superposition of the symmetric and antisymmetric modes with equal power. Hence, if exciting only channel 1 in a way that $|A_{\pm}|^2 = \kappa/\gamma$, $|A_1|^2 = |A_+ + A_-|^2 = 2\kappa/\gamma + 1/2|A_1|^2$ and then the power needed to observe the presence of the soliton is $P_{th} \equiv |A_1|^2 = 4\kappa/\gamma = 2\pi/(L_c\gamma)$. The waveguide where the field is launched in experiences an increase of the refractive index over the typical distance given by the nonlinear length, $L_{NL} \equiv 1/(\gamma P)$, so the light is trapped by this waveguide and the beating between the linear modes (coupling) is minimized. However, this is possible only because L_{NL} is substantially smaller than the beat length, since $L_{NL} \leq L_c/(2\pi)$ for input powers $P \geq P_{th}$. The threshold nonlinear phase shift associated to suppression is then given by the inverse nonlinear length,

$$\phi_{NL}^{th} \equiv \gamma P_{th} = 4\kappa = 2\pi/L_c. \tag{5.10}$$

5.1.2 Three channel system

For three waveguides, eq. 2.63 with the ansatz $A_j = a_j e^{iqz}$ results in the algebraic system,

$$\begin{bmatrix} \gamma a_1^2 & \kappa & 0 \\ \kappa & \gamma a_2^2 & \kappa \\ 0 & \kappa & \gamma a_3^2 \end{bmatrix} \begin{bmatrix} a_1 \\ a_2 \\ a_3 \end{bmatrix} = q \begin{bmatrix} a_1 \\ a_2 \\ a_3 \end{bmatrix}. \tag{5.11}$$

The amplitudes of the three modes with $\gamma = 0$, $A_{+,0,-} = [A_1, A_2, A_3]$, are found to be $A_{\pm} \equiv \frac{a_0}{2}[\pm 1, \sqrt{2}, \pm 1]$, $A_0 \equiv \frac{a_0}{\sqrt{2}}[+1, 0, -1]$, with their corresponding wavenumbers $q_{\pm} = \pm\sqrt{2}\kappa$, $q_0 = 0$. In this model, only the modes $A_{\pm}$ have interacting channels and their wavenumber difference introduces the beat length $L_c^{(3)} \equiv \pi/(2\sqrt{2}\kappa) = \pi/\mathrm{Re}(\beta_1 - \beta_3)$, where β_1, β_3 are the biggest and smallest linear propagation constants $\beta_j = \beta_0 + q_j$, where β_0 is the one of a single channel. According to this oscillator model, $\mathrm{Re}(\beta_1 - \beta_3) = \sqrt{2}\mathrm{Re}(\beta_s - \beta_a)$, what happens to be in good agreement with realistic arrays which waveguide separation is large enough (see sec. 5.4.2). The complete set of nonlinear modes of this system could not be found analytically, so numerical solutions of eq. 5.11 where sought. Their phases, q, vs total mode power, P, are plotted in fig. 5.2a. For low powers, linear shift of the nonlinear phase $dq/dP = \gamma/2$ is observed, which is expected because the power in the waveguide with more light is $P/2$. The presence of two global bifurcation points [Wiggins90], Σ and Π, gives a total of seven solutions.

Classification of the nonlinear modes, Γ, can be done taking into account the self-focusing nature of the nonlinear equations, $\kappa/\gamma > 0$. Indeed, the wavenumber

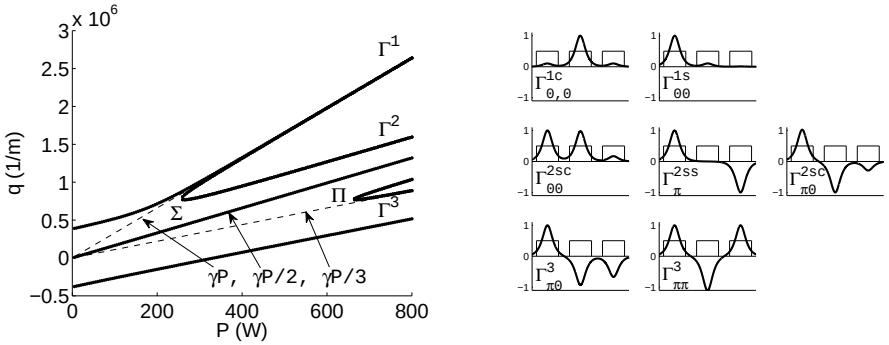

(a) (b)

Figure 5.2: (a) Phases of the three waveguides array solutions as a function of the total mode power. Numerical values are taken from the three waveguides array of section 5.4, $\kappa \approx 2.73 \times 10^5 m^{-1}$, $\gamma \approx 3300/\mathrm{W/m}$. The bifurcation points Σ and Π arise at $P \approx 260\mathrm{W}$ and 665W, respectively. (b) Normalised mode profiles at $P = 800\mathrm{W}$, sorted by decreasing q, from left to right and top to bottom. Each row is associated to one asymptotic slope.

of any mode has to tend, as $P \to \infty$, to that of a single waveguide with the power P, $P/2$ or $P/3$ depending on whether the power is asymptotically concentrated in one (Γ^1 modes), two (Γ^2) or three (Γ^3) channels. The three possible asymptotes of the wavenumbers are shown in fig. 5.2a and the mode profiles at $P = 800\mathrm{W}$ are shown in fig. 5.2b. In the case of Γ^1, there are two different families of modes. The ones with $q \gtrsim \gamma P$ concentrate most of the power in the central channel, c, and the phase difference between waveguides is 0 between channels left-centre and 0 between centre-right, so that they are identified as Γ^{1c}_{00} modes. The other Γ^1 family ($q \lesssim \gamma P$), arises from bifurcation point Σ and are Γ^{1s}_{00}, because the power is localised on a side channel, s. The other five modes, in decreasing q order, are Γ^{2sc}_{00} (arising from Σ), Γ^{2ss}_{π} (with zero power in the central channel), $\Gamma^{2sc}_{\pi 0}$ and $\Gamma^{3}_{\pi 0}$ (both arising from Π), and $\Gamma^{3}_{\pi\pi}$.

Modes Γ^{1c}_{00}, Γ^{2ss}_{π}, $\Gamma^{3}_{\pi\pi}$ exist in the linear limit as $A_{+,0,-}$, respectively. It is atright forward to see from eq. 5.11 that $\Gamma^{2ss}_{\pi} = a_0[1, 0, -1]e^{qz}, q = \gamma a_0^2 = \gamma P/2$. The other two are not stright forward to find, however, by imposing the condition $A_1 = A_3 \neq A_2$, one finds that

$$q = \frac{\gamma P}{3} + \frac{2\kappa}{3}\left[\frac{A_2^2 + A_1^2}{A_1 A_2}\right], \; A_1 A_2 = \pm \frac{\kappa P}{2q - \gamma[A_1^2 + A_2^2]}, \tag{5.12}$$

where the signs $+, -$ stand for the sign of the product $A_1 A_2$, corresponding to Γ^{1c}_{00}, $\Gamma^{3}_{\pi\pi}$, respectively. The two equations above give an expression for q,

$$q_{\pm} = \frac{\gamma}{3}\frac{P \mp 2[A_1^2 + A_2^2]^2/P}{1 \mp 4[A_1^2 + A_2^2]/[3P]}, \tag{5.13}$$

which does not give the analitical form of the curves $q(P)$ in fig. 5.2a, but its asymptotic dependences, as $P \to \infty$, are $q_+ = \gamma P$, when $A_2^2 \to P$ in Γ_{00}^{1c}, and $q_- = \gamma P/3$, when $A_1 = -A_2 = A_3 = P/3$ in $\Gamma_{\pi\pi}^{3}$, according to the assymptotic behavior predicted above.

Note the different nature of the bifurcations in the cases of two and three waveguides. In the former case, new solutions appear from existing branches and move away from them (in q) as $P \to \infty$. In the latter, however, the new solutions appear from (P,q) points apparently unrelated with the existing solutions, and then move towards the original branches as $P \to \infty$.

The appearance of the purely nonlinear modes at the bifurcations is the key feature for the switching effect shown in section 5.4.

5.2 Linear surface plasmon polariton waves

When an external electric field excites a material in a way that the movement of the electron cloud can be regarded to as freely moving electrons, a surface current is said to be generated. Under this situation the real part of the electric permittivity ϵ_m, $\mathrm{Re}(\epsilon)$, remains negative for frequencies below the critical value (plasma frequency) $\omega_c = 4\pi N e^2/m_e - 1/\tau^2$, where N, e and m_e are the volume density[1], electric charge and mass of the free electrons, respectively. τ is the typical time scale over which their motion is damped and introduces $\mathrm{Im}(\epsilon) \neq 0$ [BornWolf]. Above the plasma frequency, $\omega > \omega_p$, the material behaves as a dielectric, below, $\omega < \omega_p$, presents metallic properties and these are the interesting ones here.

In a single interface scenario between a semi-infinite metal ($\mathrm{Re}(\epsilon) < 0$) and and a semi-infinite dielectric ($\mathrm{Re}(\epsilon) > 0$), the linear propagation of the electric field eq. 2.7 in each zone reduces to the well known Helmholtz equation, in virtue of $\overrightarrow{\nabla}\,\overrightarrow{\mathcal{E}} = 0$,

$$\left(\partial_z^2 + \overrightarrow{\nabla}_\perp^2\right)\overrightarrow{\mathcal{E}} + k^2\epsilon_L\overrightarrow{\mathcal{E}} = 0, \tag{5.14}$$

where ϵ_L is a linear permittivity. Eq.5.14 limits the existence of SPP waves to the transverse magnetic (TM) case, meaning that the magnetic excitation vector, $\overrightarrow{\mathcal{H}}_w$, remains perpendicular to the direction of propagation [Maier07]. If z is associated

[1]Densities are assumed to be large, so the classical Maxwell equations can still be used.

with propagation, the y-axis is perpendicular to the interface between the dielectric ($y > 0$) and metallic ($y < 0$) media, and the x-axis is parallel to it, then the nonzero electromagnetic components of the complex fields are $\mathcal{H}_x$, $\mathcal{E}_y$, $\mathcal{E}_z$,

$$\begin{array}{ll} \mathcal{E}_y^d(y) = \mathcal{E}_{yo} e^{i\beta z} e^{-k_d y}, & \mathcal{E}_y^m(y) = \frac{\epsilon_d}{\epsilon_m} \mathcal{E}_{yo} e^{i\beta z} e^{k_m y} \\ \mathcal{E}_z^d(y) = -i\frac{k_d}{\beta} \mathcal{E}_{yo} e^{i\beta z} e^{-k_d y}, & \mathcal{E}_z^m(y) = i\frac{k_m \epsilon_d}{\beta \epsilon_m} \mathcal{E}_{yo} e^{i\beta z} e^{k_m y} \\ \mathcal{H}_x^d(y) = -\frac{\omega}{\beta} \epsilon_0 \epsilon_d \mathcal{E}_{yo} e^{i\beta z} e^{-k_d y}, & \mathcal{H}_x^m(y) = -\frac{\omega}{\beta} \epsilon_0 \epsilon_d \mathcal{E}_{yo} e^{i\beta z} e^{k_m y} \end{array} , \tag{5.15}$$

where the super-indices d, m denote dielectric and metal regions respectively, the propagation constant is $\beta \equiv k\sqrt{\epsilon_m \epsilon_d/(\epsilon_m + \epsilon_d)}$, and the decay coefficient in each medium is $k_{d,m} \equiv \sqrt{\beta^2 - k^2 \epsilon_{d,m}}$. Note that $k_{d,m}/\beta = \sqrt{1 - (\epsilon_m + \epsilon_d)/\epsilon_{m,d}}$, so the strongest component in the dielectric (metal) side is $\mathcal{E}_{y(z)}$.

In this chapter, however, we do not deal with the 1D geometry. Each waveguide has a rectangular cross section that lies on the $\hat{XY}$ plane (see inset of fig. 5.4b) and it is characterized by the width, w, along the x-axis (parallel to the metal interface) and a height, h, along the y-axis. They are separated from each other by a distance d, chosen to be above the cut off for all the linear modes (see fig. 5.4c). The z direction, perpendicular to the cross sections, is associated with propagation. Using $\overrightarrow{\nabla}\overrightarrow{\mathcal{D}} \equiv 0$ with $\overrightarrow{\mathcal{D}} = \epsilon_0 \epsilon_L \overrightarrow{\mathcal{E}}$, it is clear that

$$0 \equiv \overrightarrow{\nabla}\overrightarrow{\mathcal{D}} = \epsilon_0 \epsilon_L \overrightarrow{\nabla}\overrightarrow{\mathcal{E}} + \epsilon_0 \overrightarrow{\nabla}\epsilon_L \overrightarrow{\mathcal{E}} \rightarrow \overrightarrow{\nabla}\overrightarrow{\mathcal{E}} = -\frac{\overrightarrow{\nabla}\epsilon_L}{\epsilon_L}\overrightarrow{\mathcal{E}} \tag{5.16}$$

and hence eq. 2.7 is readily transformed into the eigenvalue equation

$$\hat{\mathcal{L}}_{2D}\overrightarrow{\mathcal{E}} = \beta^2 \overrightarrow{\mathcal{E}}, \tag{5.17}$$

with

$$\hat{\mathcal{L}}_{2D} \equiv \left[k_0^2 \epsilon_L + \overrightarrow{\nabla}_\perp^2 + \overrightarrow{\nabla}\left(\frac{\overrightarrow{\nabla}\epsilon_L}{\epsilon_L} \circ \right) \right], \tag{5.18}$$

being the circle product defined as $(F\circ)\, G \equiv (FG)$. In what follows, this equation is solved numerically in 2D using Comsol to compute the linear modes of the waveguide arrays, which linear and nonlinear properties are discussed below.

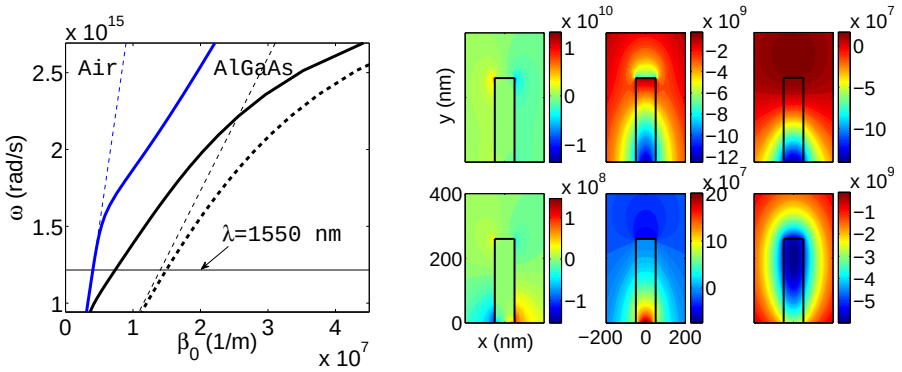

(a) (b)

Figure 5.3: (a) Dispersion of a single waveguide surrounded by air (solid blue) and placed on top of metal (solid black). The one-dimensional plasmon at the AlGaAs-silver interface (black dashed) is also plotted together with the air and AlGaAs light lines (straight dashed blue and black, respectively). (b) Real (top) and imaginary (bottom) components (x,y,z from left to right) of the electric field mode profile at $\lambda = 1550$nm. Waveguide dimensions are $w = 100$nm and $h = 260$nm.

5.3 Properties of the plasmonic modes

The relevant properties of the waveguide modes involved in the design of the arrays to observe the switching are discussed briefly below, separating the linear from the nonlinear ones. Why some particular values of w and h are chosen here will be clarified in section 5.4.

5.3.1 Linear properties

Fig.5.3a shows the numerically computed dispersion $\omega(\beta_0)$ for an AlGaAs waveguide placed on top of silver (black solid curve) or completely surrounded by air (blue solid line), together with the 1D plasmon at the silver-AlGaAs interface (black dashed curve), $\omega/\beta_0 = c\sqrt{(\epsilon_m + \epsilon_{sc})/(\epsilon_m \epsilon_{sc})}$, where ϵ_{sc} is the relative permittivity of the semiconductor and the dispersion of the silver is taken into account as in [Rakic98]. A notorious feature of the plasmonic mode dispersion is that its effective index is below the semiconductor index for $\omega \lesssim 2.210^{15}$Hz ($\lambda \gtrsim 860$nm) and above it otherwise. Indeed, for large wavelengths the semiconductor waveguide is barely seen by the plasmonic mode and it approaches the dispersion for the 1D plasmon at the air-silver interface.

At the Telecom wavelength, $\lambda = 1550$nm, the relative electric permittivities of

the AlGaAs, silver and air are assumed to be $\epsilon_{sc} = 12.1$, $\epsilon_m = -103.33 - 8.2i$ and $\epsilon_{air} = 1$, respectively. The waveguide in fig. 5.3 does not support the purely total internal reflection (TIR) guided mode, being the guidance possible only because of the metal substrate. Indeed, the metal pulls the light towards the interface (see fig. 5.3b), increasing the mode index and reducing its effective wavelength, thus decreasing the cut-off frequency for TIR guidance, happening along the x direction, from $\omega_0 \approx 1.510^{15}$Hz ($\lambda \approx 1260$nm) to $\omega \approx 0.910^{15}$Hz ($\lambda \approx 2100$nm). The Cartesian components of the mode profile plotted in fig. 5.3b show its pronounced SPP nature along $\hat{y}$, with the predominant component being perpendicular to the metal substrate (see eqns. 5.15).

Fig.5.4a shows the real effective index, $n_{eff} \equiv \mathrm{Re}(\beta_0)/k$, of an $h = 260$nm waveguide as a function of its width, w (and the cut-off at $w = 280$nm for the same waveguide placed on glass substrate). The large effective indices correspond to modes highly confined at the metal interface, thus with propagation length, $L_{loss} \equiv 1/\mathrm{Im}(\beta_0)$, limited to $\sim 10\mu$m, as fig. 5.4b shows. Same figure shows coupling length for two waveguides, L_c, as a function of separation, d, for the $w = 100$nm case, being $d \lesssim 485$nm necessary for the beating to occur before the power is substantially dumped by the loss length. In the three waveguides ($w = 100$nm, $h = 260$nm) array, existence of all three linear modes requires $d \gtrsim 200$nm.

5.3.2 Nonlinear properties

The nonlinear coefficient γ of a single channel has been computed from the linear mode profiles, using eq. 2.38

$$\gamma = \epsilon_0^2 \omega_0 c \frac{\epsilon_{sc} \int\int dxdy\; n_2(x,y) \frac{2}{3} \left[\left| \overrightarrow{\mathcal{E}} \right|^4 + \frac{1}{2} \left| \overrightarrow{\mathcal{E}}^2 \right|^2 \right]}{\left[\int\int dxdy \mathrm{Re} \left\{ \overrightarrow{\mathcal{E}} \times \overrightarrow{\mathcal{H}^*} \right\} \hat{u}_z \right]^2}, \tag{5.19}$$

where $n_2 \simeq 1.5 \times 10^{-17} m^2/\mathrm{W}$ for AlGaAs[2]. It is shown in fig. 5.5a as a function of the waveguide width, w, and height, h. For the range of heights shown here, it has the maximum values for $w \in [120, 130]$nm which correspond to the optimum modal confinement. Narrower waveguides fail to keep the light inside and the wider ones spread the mode over the larger area.

A precisely calculated γ is important for an accurate prediction of the threshold power for the directional coupler, given in eq. 5.10 and shown as a function of d

[2]Note the widely used silicon has, apart from a strong TPA, the smaller nonlinear index $n_2 \simeq 4 \times 10^{-18} m^2/\mathrm{W}$.

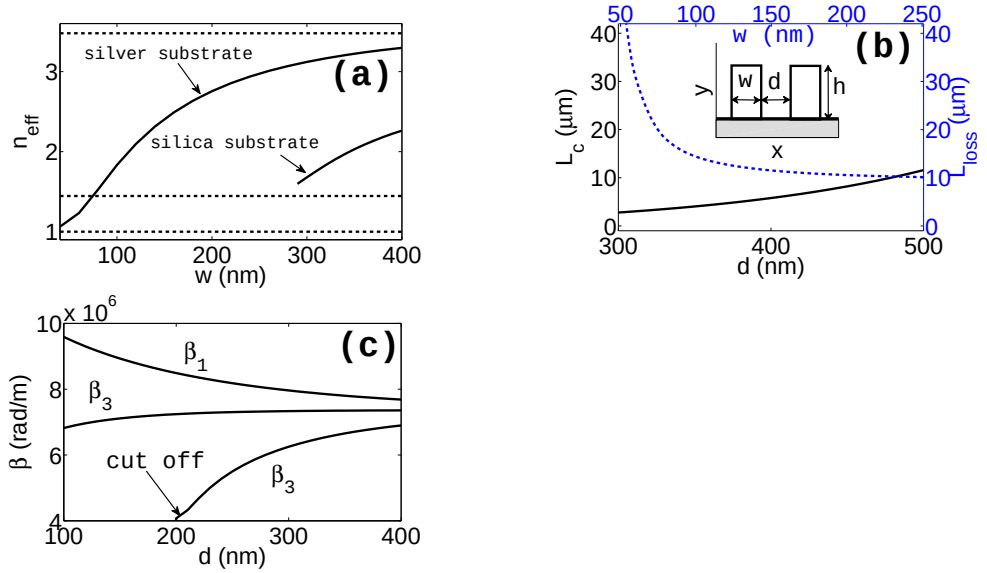

Figure 5.4: (a) Effective index of the single semiconductor on metal and semiconductor on silica wires as a function of the waveguide width, w, for $h = 260$nm. Dashed horizontal lines mark (from bottom to top) the refractive indices of air, glass and semiconductor, respectively. (b) Loss length (dashed blue) in a single waveguide on metal substrate as a function of the waveguide width, w. Coupling length (full line) for two coupled waveguides as a function of the separation distance, d, and $w = 100$nm. (c) Propagation constants of the three waveguides array linear modes as a function of separation.

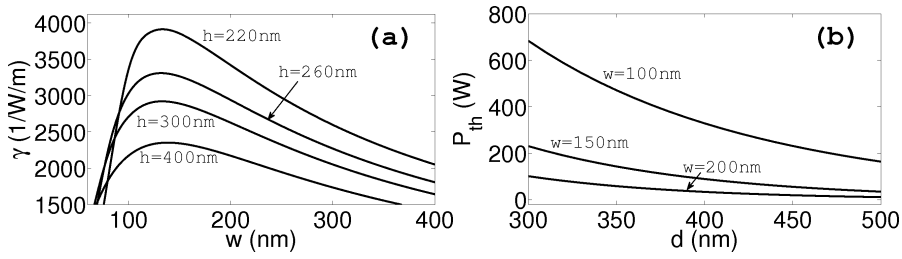

Figure 5.5: (a) Nonlinear parameter γ and (b) P_{th} as a function of d, calculated for several widths and $h = 260$nm.

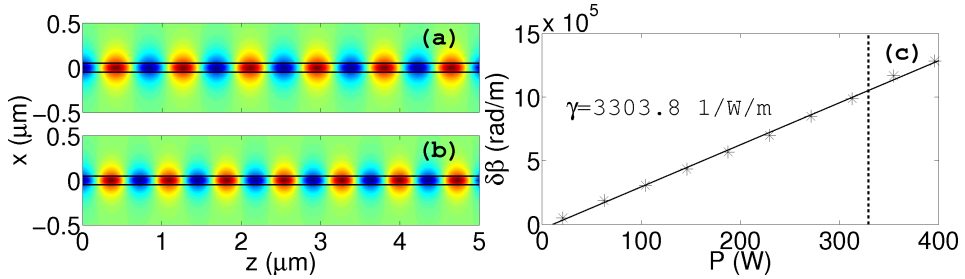

Figure 5.6: Evolution of $\mathrm{Re}(\mathcal{E}_y)$ in a single waveguide with $w = 100$nm and $h = 260$nm. (a) is the linear regime and (b) is the nonlinear one (with $P = 396$W). (c) shows the nonlinear phase shift as a function of P, the slope of the straight line gives γ and the dashed vertical line marks P_{th}.

for different w values in fig. 5.5b. The derivation of eq. 2.38 (see chapter 2) is based on a perturbation approach [Shahraam Afshar09] and its value at $P \approx P_{th}$ might be different from the one predicted by this formula. Also, the mode profile may have changed significantly from the linear one, yielding even a correct formula to some significant error. For this reason, γ was explicitly computed by measuring the nonlinear phase shift, $\phi_{NL} \equiv \gamma P = \beta_{NL} - \beta_0$, in single channel simulations ($w = 100$nm, $h = 260$nm) done with different input powers, P, as shown in fig. 5.6. Fig.5.6a,b show examples of propagation with $P = 20$W, 396W, from which the fitting in fig. 5.6c gives $\gamma \approx 3300$/W/m, which is larger than the value of ~ 3000/W/m given by eq. 2.38.

5.3.3 Comparison with "on glass" waveguides

The advantage of the metal substrate, in comparison to silica glass ($\epsilon_s = 2.01$) substrate is obvious when comparing the nonlinear coefficients of fig. 5.5 and fig. 5.7. In the latter case, the nonlinear coefficient is shown for several geometries and its global maximum is achieved at $\gamma \approx 920$/W/m, for a waveguide with $w \approx 200$nm and $h \approx 380$nm.

5.4 Nonlinear switching: numerical results

The numerical results corresponding to 3D propagation simulations are presented here. First, the directional coupler parameters are optimised to observe the switching effect over the propagation distance, and then the third waveguide is added, keeping

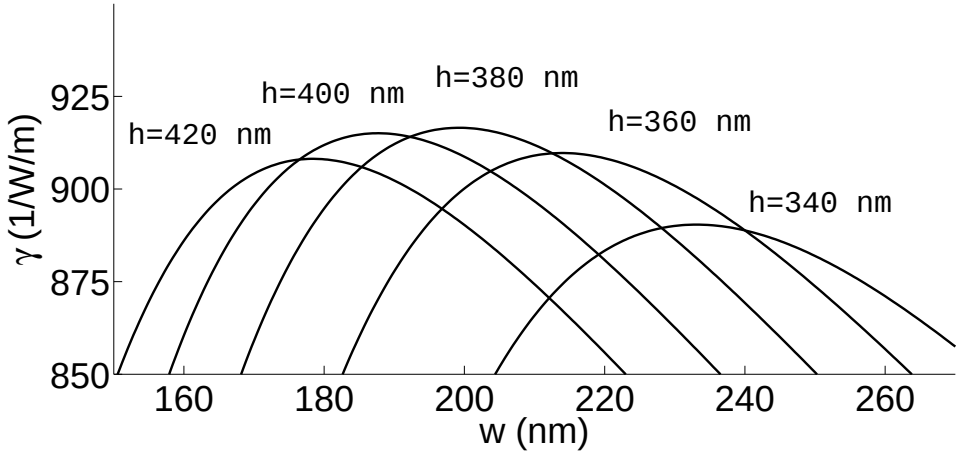

Figure 5.7: Nonlinear coefficient γ for an AlGaAs waveguides on silica glass as a function of the width, w, and height, h.

the same geometry parameters, to show the nonlinear switching when exciting the array in either the central or a side channel.

Before proceeding, it has to be mentioned that the silver domain, which requires very small mesh elements (to sample properly the electric field decay) and a substantial amount of RAM memory in the NL simulations, has been replaced by the Leontovich's standard impedance boundary condition (IBC) [Senior95], applied at the interface with the metal. Its equation is given by

$$\overrightarrow{u_y} \times \left[\overrightarrow{u_y} \times \overrightarrow{\mathcal{E}}\right] = Z\overrightarrow{u_y} \times \overrightarrow{\mathcal{H}}, \tag{5.20}$$

where $\overrightarrow{u_y}$ is the unitary vector perpendicular to the interface and $Z \equiv \sqrt{\mu_0\mu_m/(\epsilon_0\epsilon_m)} \approx [1.4 + 35i]\,\pi 10^{-6}\Omega$ the intrinsic impedance of the silver (for $\mu_m = 1$). This is a first order in the metal refractive index boundary condition and it is valid under the assumption that the complex refractive index of the metal $n_m \approx \sqrt{\epsilon_m} = 0.4 - 10.17i$ is such that $|n_m| \gg 1$. Moreover it is derived from the linear Helmholtz equation. After it has shown to reproduced almost identical results as the simulations done with silver domain in the 2D computation of the linear modes, it has been implemented for the 3D simulations below.

5.4.1 Two waveguides: optimisation of the array geometry

To observe the switching in a realistic set-up, which is limited by the big metal losses, the array parameters must be chosen to accomplish $L_{NL} < L_c < L_{loss}$ for input powers $P \geq P_{th}$. The first part of the inequality has been already discussed in section 5.1.1 and is automatically accomplished above P_{th}. However, the second inequality requires tuning of the array geometry and the primary objective here is to achieve a big propagation distance L_{loss}, big ratio $R \equiv L_{loss}/L_c \gtrsim 2$, reasonably low P_{th} and a small size of the device.

Thus, the optimisation of the array is as follows. For a fixed waveguide height $h = 260$nm (fabrication limitations), the natural choice for w would be the one that maximises γ in fig. 5.5a ($w \approx 120$nm). Indeed, both R and L_{loss} are improved by decreasing w slightly ($w = 100$nm), because of the bigger propagation distance (see fig. 5.4b) and the smaller L_c, associated to the smaller effective index (mode spreads out of the waveguide). However, this increases a bit the P_{th}. Note that increasing the width from $w = 120$nm by an amount which leads to the same decrease of γ reduces the propagation distance and increases L_c (because the mode with larger n_{eff} is more confined inside the waveguide), what worsens R. This could be an option if the starting R was big enough, since this decreases P_{th} (see fig. 5.5b) but the device would also increase in size. One could think of improving R by keeping w and h constant with γ maximised and tune d, increasing L_c and reducing P_{th}. However, this option yields to an increase of the separation between waveguides, d, enlarging again the size of the device and its smallness remains a priority. Figs.5.4b and 5.5b show that L_c and P_{th} follow opposite trends as d increases. For the chosen single waveguide, with $w = 100$nm and $h = 260$nm, separation was fixed to $d = 400$nm, what gives a relatively low $P_{th} \approx 330$W and a good ratio $R \approx 2.78$.

Fig.5.8 shows the norm of the electric field, $|\overrightarrow{\mathcal{E}}|$, along a loss length ($L_{loss} = 16.1\mu$m) in the optimised coupler. The array is excited in the channel at $x = 0$nm, with its linear mode, and oscillations of the light in the linear regime (top row of fig. 5.8) occur over the predicted coupling length $L_c = 5.785\mu$m. Just above the threshold power, $P_{th} = 330$W, the loss less nonlinear modelling in 5.8d shows clear signatures of the Ψ_s mode, plus small power transfer over a distance $\sim 3.3\mu$m$< L_c$. In the presence of loss (5.8e), the switching is expected to be survive a length $z_{sw} \equiv \frac{1}{2} L_{loss} \ln\left(\frac{P}{P_{th}}\right)$; $P \geq P_{th}$, so power should rise up to $P \approx 2.44$kW. This is too high for the modelling conditions here, but the higher input $P = 520$W already shows switching over the length of $\sim 4\mu$m, as can be seen from plot (f), where the guided power is calculated through the integral of the Poynting's vector $\int dxdy \mathrm{Re}[\overrightarrow{\mathcal{E}} \times \overrightarrow{\mathcal{H}}^*]\hat{u}_z/2$.

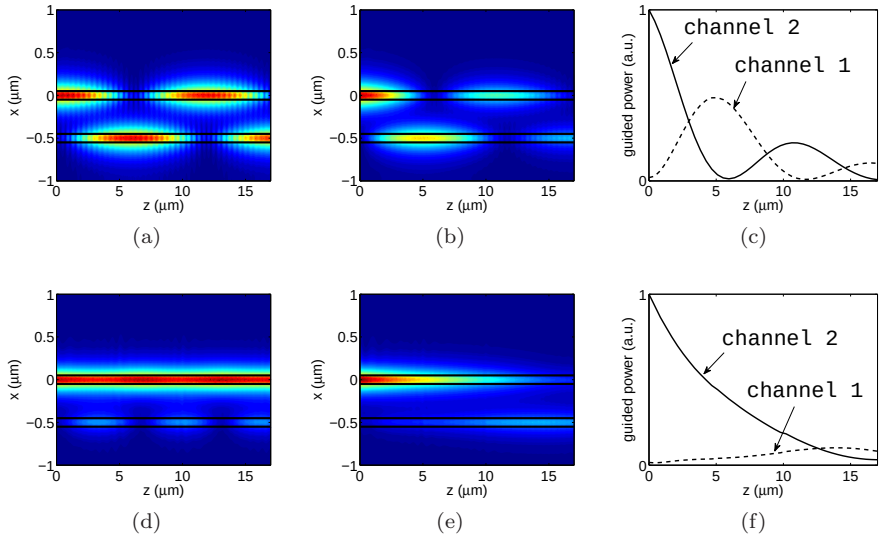

Figure 5.8: Linear (up) and nonlinear (down) propagation in a two waveguides array in the absence (a,d) and presence (b,e) of loss along 17μm. The input power for nonlinear simulations with (without) loss is $P = 520$W ($P = 333$W) and it is launched in the channel at $x = 0$nm. $|\vec{\mathcal{E}}|$ is plotted at the $y = 0^{+}$nm plane, corresponding to the semiconductor region in the vicinity of the interface. (c,f) Variations of the normalised power flow in the semiconductor wires. Array dimensions are $w = 100$nm, $h = 260$nm, $d = 400$nm.

5.4.2 Three waveguides

The array of three waveguides is simply made by adding one waveguide to the directional coupler, keeping the same values of w, h and d. One important reason for this is that the estimated $P_{th} = 330$W to be launched in one channel is enough to excite the Γ^1 modes, since fig. 5.2a (done for the specific parameters of the array here) shows this is above the bifurcation point Σ, at $P \approx 260$W.

In this case, linear modelling in figs. 5.9 and 5.10 shows good agreement with the predicted $L_c^{(3)} \equiv \pi/\mathrm{Re}(\beta_1 - \beta_3) = 4\mu\mathrm{m}$[3]. Note $[L_c/L_c^{(3)}]^2 = 2.1 \approx 2$, as the model in section 5.1.2 predicts, thus the chosen distance $d = 400$nm is not only appropriate for the existence of the three linear modes (see fig. 5.4c), but also for the suitability of the DNLS model.

Central channel excitation with $P = 333$W ($> P_{th}$) in fig. 5.9d shows a light distribution in the three waveguides according to the one of the Γ_{00}^{1c} mode. It could be argued, in principle, that this modelling is not a clear proof of the switching, since such mode already exists below the bifurcation Σ and the small oscillations resemble the linear ones in fig. 5.9d. However, the side excitation with the same input P, in fig. 5.10d, presents the Γ_{00}^{1s} profile, which does not exist at all below bifurcation and small oscillations do not resemble any more the ones in fig. 5.10a.

Figs. 5.11 and 5.12 show in 3D the linear and nonlinear modelling with loss of figs. 5.9 and 5.10, respectively. The input face ($z = 0$) shows the field distribution corresponding to the single waveguide linear mode, used to excite the arrays in all the modelling presented in this last section.

5.5 Conclusions

The arrays of two and three waveguides considered in this chapter represent four and nine port systems, respectively. In the absence of losses it is evident from figs. 5.8(a,d) and 5.10(a,d) how the output power of a fixed length device can be collected from any of the waveguides by modifying the input power. Moreover, the plasmonic modes supported by the waveguides due to the metal substrate permits the reduction of the device size well below the sub wavelength scale and reducing the threshold power to few hundred's of Watts [Milián11]. However, the Ohmic losses introduced by the

[3]Note the linear modelling in fig. 5.10a does not show that all the power comes back to the initial channel after a distance of $4L_c^{(3)} = 16\mu$m. This is simply because the simulations solve the full Maxwell equations, and hence there is a strictly nonzero second neighbour interaction, accounted for by the coefficient $\kappa^{(2)}$ in eqns. 2.58-2.59, which leads to nonzero elements in the top-right and bottom-left corners of the matrix in the model eq. 5.11. This is not shown explicitely here because it is not of special relevance for the present work.

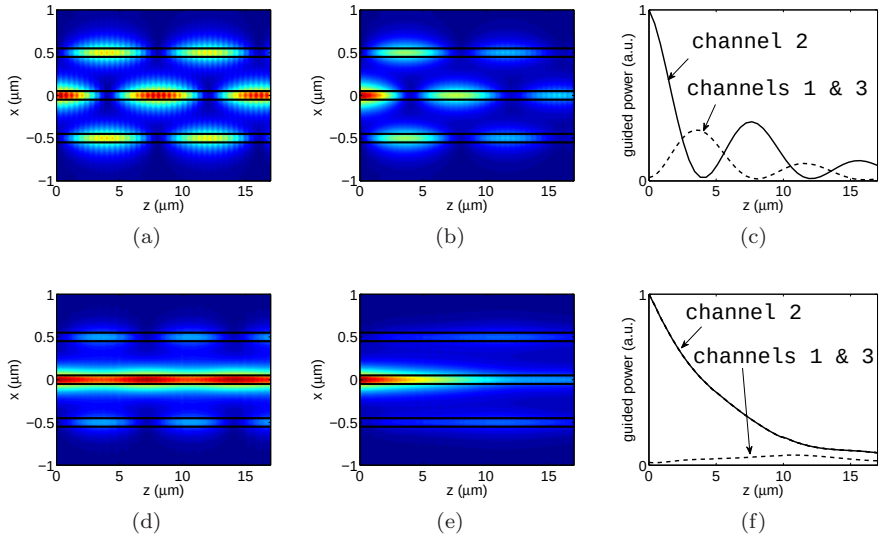

Figure 5.9: Central channel excitation of the three waveguides system. Linear (up) and nonlinear (down) propagation in the absence (a,d) and presence (b,e) of loss along 17μm. The input power for nonlinear simulations with (without) loss is $P = 520$W ($P = 333$W) and it is launched in the channel at $x = 0$nm. $|\vec{\mathcal{E}}|$ is plotted at the $y = 0^{+}$nm plane, corresponding to the semiconductor region in the vicinity of the interface. (c,f) Variations of the normalised power flow in the semiconductor wires. Array geometry paremeters are $w = 100$nm, $h = 260$nm and $d = 400$nm.

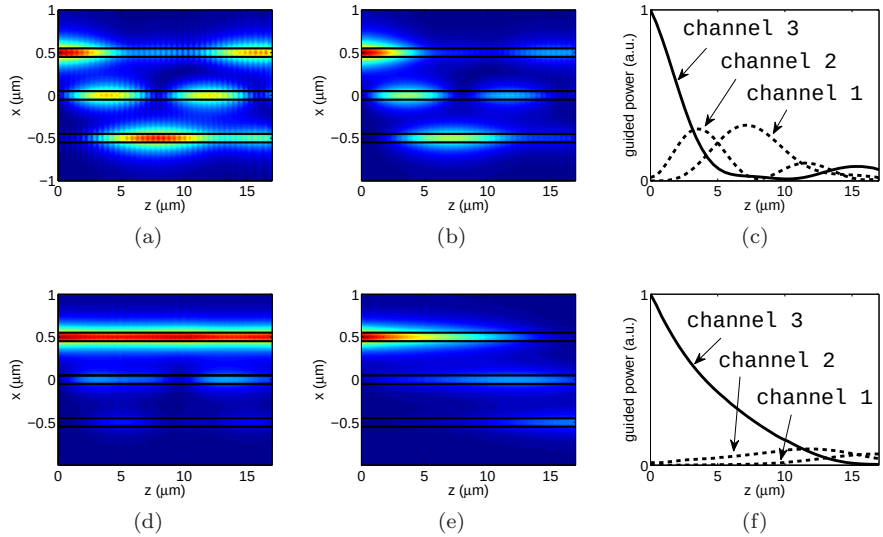

Figure 5.10: Side channel excitation of the three waveguides. Linear (up) and nonlinear (down) propagation in the absence (a,d) and presence (b,e) of loss along 17 μm. The input power for nonlinear simulations with (without) loss is $P = 520$W ($P = 333$W) and it is launched in the channel at $x = 500$ nm. $|\vec{\mathcal{E}}|$ is plotted at the $y = 0^{+}$nm plane, corresponding to the semiconductor region in the vicinity of the interface. (c,f) Variations of the normalised power flow in the semiconductor wires. Array geometry paremeters are $w = 100$ nm, $h = 260$ nm and $d = 400$ nm.

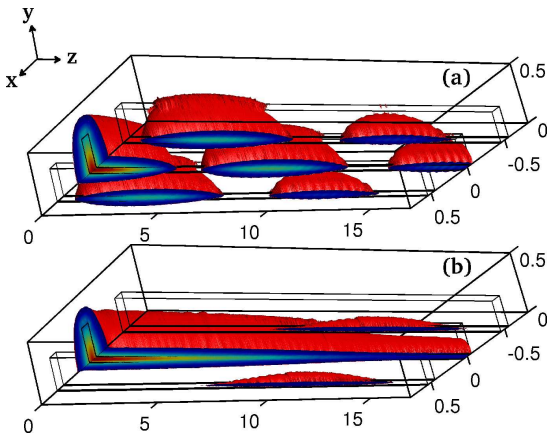

Figure 5.11: Evolution of $|\vec{\mathcal{E}}|$ in the three waveguides array for the central excitation case in the (a) linear and (b) nonlinear regimes. The red iso-surfaces enclose the volume inside the semiconductor ($y > 0$) where $|\vec{\mathcal{E}}| \geq 5.5 \times 10^8$V/m. Distances shown are measured in microns.

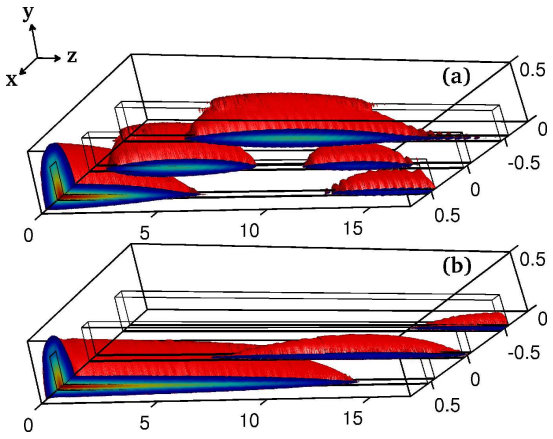

Figure 5.12: The same as fig. 5.11, but when the input is sent into the edge waveguide.

metal hinder the practical use of the arrays considered here. Note from the guided power plots in figs. 5.8(c,f)-5.10(c,f) that the power in the initially excited channels is kept higher than the one in the other channels for just about 10μm$\sim 2L_c$, where the power is reduced so much that linear mode beating takes place again. Hence, further work considering, e.g., the introduction of gain in the semi-conductor material to compensate for the metal losses would be required in order to obtain a miniaturised array for all optical switching applications [Christodoulides88]. This sort of systems are essential elements for integrated photonic circuits [Salgueiro10].

Chapter 6

Existence, stability and dynamics of soliplasmons: soliton-plasmon supermodes

Optical solitons have been considered in this thesis, mostly in the temporal domain, where dispersion is compensated by nonlinearity (chapters 2-4). The *discrete* diffraction compensation in the spatial domain (removal of mode beating) has been the subject of chapter 5, in the context of SPP waveguide modes. In this chapter, we consider the hybrid modes resulting from the coupling between a soliton and a plasmon in the spatial domain, where each of them propagates in its own channel. They are then called *soliplasmon* supermodes. In this case, coupling between the two channels occurs through the strongest electric field component, whereas in chapter 5 the channels where coupled through the weak one.

The success in previous chapter comparing full 3D simulations of the nonlinear Maxwell equations with the scalar NL oscillator model, motivates us to reduce the dimensionality of the current problem to 2D, relying on a modified NL oscillator model.

Our aim here is to proof existence of stationary solutions and their stability, which qualitatively agrees with the Vakhitov-Kolokolov (VK) criterion. Instability generates a rich dynamics that depends on the relative phases between the two components (soliton and SPP). Rigorous understanding of this dynamics is not provided by the model developed here.

The chapter consists on the following parts. Section 6.1 introduces the spatial NLSE and its 1D bright soliton solution. The matching between Solitons and linear plasmons in metal-dielectric-Kerr (MDK) 1D structures is considered in section 6.2

and the corresponding NL oscillator model is introduced in 6.3. Stationary solutions and their properties are derived in section 6.4 and their stability is analysed in 6.5, by means of numerical propagation simulations.

6.1 The spatial solitary wave

As it was discussed in chapter 2, eq. 2.20 assumes a well defined linear polarisation state for the light. When applying the field decomposition $\overrightarrow{\mathcal{E}}_\omega = \overrightarrow{A}e^{i\beta z}$ and using the permittivity tensor in eq. 2.53, $\overrightarrow{\mathcal{D}}_\omega = \epsilon_0\hat{\epsilon}\overrightarrow{\mathcal{E}}_\omega$ and the resulting paraxial equation is

$$2i\beta\partial_z\overrightarrow{A} + \nabla_\perp^2\overrightarrow{A} + \mathcal{O}\left(\partial_z^2 A\right) = \left[\beta^2 - \frac{\omega^2}{c^2}\hat{\epsilon}\right]\overrightarrow{A} = -k^2\hat{\epsilon}_{NL}\overrightarrow{A}, \tag{6.1}$$

where $\hat{\epsilon}_{NL}$ is the nonlinear part of $\hat{\epsilon}$, $k \equiv \omega/c$ and $\beta \equiv k\sqrt{\epsilon_L}$. In the 1D problem, the transverse component y is assumed to be irrelevant, meaning that no net flux is to propagate in this direction and hence $A_y \equiv 0$. Moreover, if $|A| \gg |A_z|$, then $A \approx A_x$ and eq. 6.1 reduces to the well known spatial *Nonlinear Schrödinger Equation* (NLSE),

$$i\partial_z A + \frac{1}{2\beta}\partial_x^2 A + \gamma|A|^2 A = 0, \tag{6.2}$$

where the spatial nonlinear coefficient[1] $\gamma \equiv \frac{k^2\chi^{(3)}}{2\beta}$, $\chi^{(3)} = \epsilon_L\epsilon_0 c n_2$ and $n_2 = 2.6 \times 10^{-20} m^2/\mathrm{W}$ for silica glass. The analytical solution of eq. 6.2 in self-focusing media is the so called spatial bright soliton given by [Kivshar06]

$$A(x,z) = c_s sech(\sqrt{\gamma\beta}|c_s|x)e^{iz\gamma|c_s|^2/2}. \tag{6.3}$$

As in temporal solitons (see, e.g., eqns. 3.3, 3.6, 3.7 and 4.1), the amplitude c_s parametrises the width and the propagation constant, which in our paraxial[2] approach is

$$\beta_s = \beta + \frac{\gamma|c_s|^2}{2} = \beta\left[1 + g|c_s|^2\right], \tag{6.4}$$

where $g \equiv \epsilon_0 c n_2/4$ and $g|c_s|^2$ is dimensionless.

[1] Note the different physical meaning of the nonlinear coefficients, γ, introduced in the context of temporal optics in chapter 2 and the one of eq. 6.2. In the former context, the waveguide modulates the light spatial mode profile and defines the nonlinear coefficient from it. In the latter case, the spatial mode is to be self induced at a given power so γ depends only on the bulk properties of the material and the corresponding plane wave.

[2] Spatial soliton of the non-paraxial non-linear Helmholtz equation can be also found and it has a slightly different wave number. However, non-paraxial propagation is beyond the scope of this chapter.

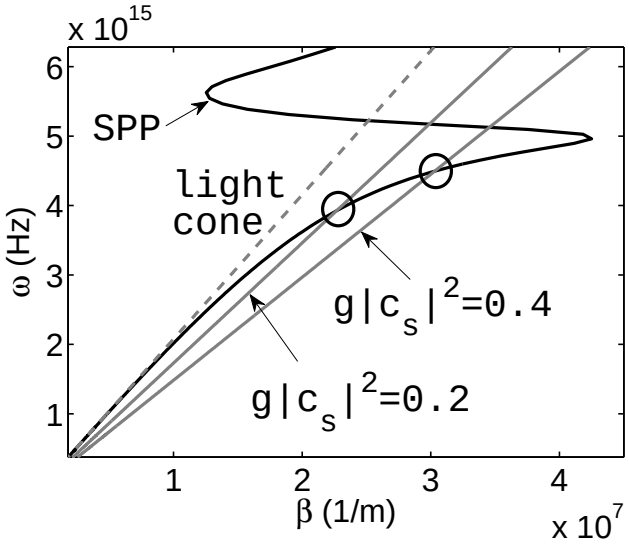

(a)

Figure 6.1: Dispersion relations of linear SPP (black) and spatial soliton (grey) in the single interface between silica glass, with $\epsilon_L = 2.08$, and dispersive silver (as in section 5.3.1). Circles enclose the monochromatic matching points in the (β, ω) plane and the dashed grey marks the light cone $\omega = \beta c/\sqrt{\epsilon_L}$.

6.2 Weak coupling between linear SPP's and spatial solitons

The single interface geometry considered here between the dielectric ($x > 0$) and metallic ($x < 0$) media imposes the nonzero electromagnetic components of the SPP (TM) are $\mathcal{H}_y$, $\mathcal{E}_x$ and $\mathcal{E}_z$, which propagation constant, given in chapter 5 (section 5.2), can be written as

$$\beta_p \equiv \beta\sqrt{\epsilon_m/(\epsilon_m + \epsilon_L)}. \tag{6.5}$$

By comparing eqns. 6.4, 6.5 it is obvious that a feature shared by a spatial soliton and a SPP is that their effective indices are always bigger than that of the bulk dielectric material and their propagation constants are thus above the dielectric light cone[3], what makes possible the intersection between their dispersion relations, what in principle means they can couple. Note, this property is related to the fact that they are not radiation modes, thus having decaying tails along x. Therefore, when they propagate along parallel lines and are far away enough so their tail overlap remains

small (weak coupling), the matching condition, $\beta_s = \beta_p$, is given by

$$|c_s|^2 = \frac{2k\epsilon_L}{\gamma}\left[\sqrt{\frac{\epsilon_m}{\epsilon_m+\epsilon_L}} - 1\right], \tag{6.6}$$

and is controlled only by the soliton amplitude. Fig. 6.1 shows the dispersion relations of the SPP and soliton. The peak power of the latter shifts its propagation constant away from the light cone, and hence the wavelength for the matching decreases. It is our purpose here to focus on the SPP, so resonances above $\omega \approx 5 \times 10^{15}$ are disregarded.

6.3 Coupled oscillator model for Metal-Dielectric-Kerr media

In this section it is derived an oscillator model for the linear plasmon and soliton in 1D. SPP is located at the metal-dielectric interface ($x = 0$) and the soliton is hosted by a Kerr type nonlinear material and is centred at $x = a$. Thickness of the linear medium $d \sim k_d \equiv \sqrt{\beta_p^2 - k^2\epsilon_d} \ll a$ and the nonlinear index $n_2(x) = n_2\mathrm{H}(x-d)$, where H is the Heaviside function. Thus, the linear permittivity takes the values $\epsilon_L(x<0) = \epsilon_m$, $\epsilon_L(0 \le x < d) = \epsilon_d$, $\epsilon_L(x \ge d) = \epsilon_k$. Because the spatial soliton self-induces its own waveguide and it is not a linear mode of a crafted one with well defined geometry, eq. 2.63 (used in chapter 5) is not of use here. Instead, a variational approach is adopted below.

The nonlinear propagation of electromagnetic monochromatic light in our geometry is obtained by combining eqns. 2.7, 2.52 and 5.16,

$$\left(\partial_z^2 + \partial_x^2\right)\overrightarrow{\mathcal{E}}_w + k^2\epsilon_L\overrightarrow{\mathcal{E}}_w = -\overrightarrow{\nabla}\left[\epsilon_L^{-1}\overrightarrow{\nabla}\epsilon_L\overrightarrow{\mathcal{E}}_\omega\right] - k^2\chi^{(3)}\frac{1}{3}\left\{2|\overrightarrow{\mathcal{E}}_\omega|^2\overrightarrow{\mathcal{E}}_\omega + \overrightarrow{\mathcal{E}}_\omega^2\overrightarrow{\mathcal{E}}_\omega^*\right\}, \tag{6.7}$$

which contains both the (non-paraxial) spatial soliton and the SPP, noting that the former obeys it without the first term in the RHS, and the latter without the second term in the RHS. Thus, the variational ansatz is

$$\overrightarrow{\mathcal{E}}_\omega(x,z) = \left[c_p(z)\overrightarrow{e}_p(x) + \hat{u}c_s(z)f_s(x-a)\right]e^{ikn_k z}, \tag{6.8}$$

where $c_{p,s}$ are the amplitudes of the SPP and soliton, respectively, which are

[3] this is strictly true in 1D only, in 2D geometries this occurs below a threshold wavelength. See fig. 5.3 in section 5.3.1 for the case of linear SPP waves.

the only parameters allowed to be z-dependent. The SPP field is given in eq. 5.15 after interchanging the x, y coordinates. $c_p \approx \mathcal{E}_{y0}$ and $e_{px} \sim exp(-k_i|x|)$, $k_i \equiv \sqrt{\beta_p^2 - k^2\epsilon_i}$ and $i = m(x < 0)$, $d(0 \leq x < d)$, $k(x \geq d)$. The soliton field is $f_s(x-a) = sech(\sqrt{\gamma\beta}|c_s|[x-a])$, which polarisation is fixed in the direction of the unitary vector $\hat{u}$. Substitution of eq. 6.8 into the paraxial version of eq. 6.7, i.e. $\partial_z^2(\Psi e^{ikn_k z}) \approx (2ikn_k\partial_z - k^2n_k^2)\Psi e^{ikn_k z}$, results in an equation containing both the soliton and plasmon propagation,

$$
\begin{aligned}
&2ikn_k\frac{d}{dz}c_p(z)\vec{e}_p + \left\{\partial_x^2 + k^2\left[\epsilon_L(x) - n_k^2\right] + \overrightarrow{\nabla}\left(\epsilon_L^{-1}\overrightarrow{\nabla}\epsilon_L\circ\right)\right\}\left[\vec{e}_p c_p(z)\right] + \\
&2ikn_k\frac{d}{dz}c_s(z)\hat{u}f_s + \left\{\partial_x^2 + k^2\left[\epsilon_L(x) - n_k^2\right]\right\}f_s\hat{u}c_s + 2\hat{u}\beta\gamma f_s^3|c_s|^2c_s = \\
&\overrightarrow{\nabla}\left(\epsilon_L^{-1}\overrightarrow{\nabla}\epsilon_L c_s(z)\hat{u}f_s\right) + \mathcal{O}\left(c_s^2c_p\right),
\end{aligned}
\tag{6.9}
$$

where the cross phase modulation (XPM) terms $\sim \mathcal{O}\left(c_s^2c_p\right)$ have been neglected. We focus on the x component of this equation, in virtue of the quasi transversal approximation, what implies that $e_p \approx e_{px}$ and $\hat{u} \approx \hat{x}$. Eq. 6.9 can be solved in the region $x < d$ ($x > d$) to obtain the equation for the plasmon (soliton), taking the effects of $x > d$ ($x < d$) up to first order. When seeking an equation for the SPP, eq. 6.9 shall be rewritten as

$$
\begin{aligned}
&2ikn_k\frac{d}{dz}c_p(z)e_p - k^2n_k^2e_pc_p(z) + \left\{\partial_x^2 + k^2\epsilon_L(x) + \overrightarrow{\nabla}\left(\epsilon_L^{-1}\overrightarrow{\nabla}\epsilon_L\circ\right)\right\}e_pc_p(z) + \\
&k^2\left[\epsilon_L(x) - n_k^2\right]f_sc_s + \mathcal{N}\hat{\mathcal{L}}\mathcal{S}\left(f_sc_s\right) \approx 0,
\end{aligned}
\tag{6.10}
$$

where the operator $\mathcal{N}\hat{\mathcal{L}}\mathcal{S} \equiv 2ikn_k\partial_z + \partial_x^2 + 2\beta\gamma f_s^2|c_s|^2 \equiv 0$ because of eq. 6.2 and $\{\dots\} = \beta_p^2 + \mathcal{O}\left(e_p(x)\epsilon_k\mathrm{H}(x-d)\right)$ in virtue of the linear eigenvalue equations 2.16 and 2.17 (see section 2.2), for the x (transverse) component. Applying the same strategy to the Kerr medium, the equation for the soliton evolution is found in the form

$$
\begin{aligned}
&2ikn_k\frac{d}{dz}c_s(z)f_s + \left\{\partial_x^2 + k^2\left[\epsilon_L(x) - n_k^2\right] + 2\beta\gamma f_s^2|c_s|^2\right\}f_sc_s + \\
&\left[2kn_k\left[kn_k - \beta_p\right] - k^2n_k + \beta_p^2\right]e_pc_p = 0,
\end{aligned}
\tag{6.11}
$$

where it has been used that $-i\frac{d}{dz}c_p(z) = [\beta_p - kn_k]c_p(z)$, as implied by the reference wavenumber, kn_k, used in eq. 6.8. Assuming that $\epsilon_d \approx \epsilon_k$ and $-\epsilon_m \gg \epsilon_d$, $\frac{d}{dz}c_p(z)$ can be neglected and the operator $\{\dots\} = 2\beta\left[-i\partial_z(c_sf_s)\right] + \mathcal{O}\left(f_s(x-a)\epsilon_m\mathrm{H}(-x)\right) \approx$

$\gamma\beta|c_s|^2$, according to eq. 6.2 with $A \to c_s f_s$.

Eqns. 6.10, 6.11 are the system of coupled equations, which reads

$$i\frac{d}{dz}c_p + \mu_p c_p + q c_s = 0 \tag{6.12}$$

$$i\frac{d}{dz}c_s + \mu_s c_s + \bar{q} c_p = 0 \tag{6.13}$$

where,

$$\mu_p \equiv \frac{1}{2kn_k}\left[\beta_p^2 - k^2 n_k^2\right] \tag{6.14}$$

$$\mu_s(|c_s|) \equiv \frac{\gamma}{2}|c_s|^2 \tag{6.15}$$

$$q \equiv \frac{k}{2n_k N_p}\mathrm{I} \tag{6.16}$$

$$\bar{q} \equiv \frac{k}{2n_k N_s}\mathrm{I} = \frac{N_p}{N_s}q \tag{6.17}$$

$$\mathrm{I} \equiv \int_x \left[\epsilon_L - n_k^2\right] e_p(x) f_s(x-a) \tag{6.18}$$

$$N_p \equiv \int_x |\vec{e}_p|^2 \tag{6.19}$$

$$N_s \equiv \int_x f_s^2 \tag{6.20}$$

$\mu_{s,p}$ are a measure of the distance between the the soliton and plasmon wavenumbers and the light cone $\omega = ck/n_k$. In the weakly coupling scenario, the linear dielectric region $x \in [0, d]$ is reached by the soliton tail $f_s(x-a) \approx 2exp(-\kappa_s[x-a])$, where $\kappa_s \equiv \sqrt{\gamma\beta}|c_s|$ is the inverse soliton width. Besides, the plasmon field is assumed small for $x \gtrsim d$. Hence, the coefficients above may be expressed in the explicit form

$$\mathrm{I} \approx 2\frac{\epsilon_d\left[\epsilon_m - \epsilon_k\right]}{\epsilon_m\left[\kappa_s + k_m\right]}e^{-\kappa_s a} + \mathcal{O}\left(\epsilon_d - \epsilon_k\right) \tag{6.21}$$

$$N_p \approx \frac{\epsilon_d}{2}\left[\frac{1}{k_m\epsilon_m} + \frac{1}{k_d\epsilon_d}\right] + \mathcal{O}(e^{-2k_d d}) \equiv \frac{\epsilon_d}{2\mathrm{B}_r} \tag{6.22}$$

$$N_s = \frac{2}{\kappa_s} \tag{6.23}$$

$$q \approx \frac{2k}{n_k\epsilon_m}\frac{\epsilon_m - \epsilon_k}{\kappa_s + k_m}\mathrm{B}_r e^{-\kappa_s a} \tag{6.24}$$

$$\bar{q} = \frac{N_p}{N_s} q = \frac{k\kappa_s \epsilon_d}{2n_k \epsilon_m} \frac{\epsilon_m - \epsilon_k}{\kappa_s + k_m} e^{-\kappa_s a} \tag{6.25}$$

$$\mathrm{B}_r \equiv \frac{k_m \epsilon_m k_d \epsilon_d}{k_m \epsilon_m + k_d \epsilon_d}. \tag{6.26}$$

This coupled model predicts that a SPP can be excited by a soliton (see eq. 6.12), through the driving term qc_s. $q \sim e^{-\kappa_s a}$ and hence it tells us that the decaying exponential soliton tail acts as the driving field for SPP excitation[4]. This suggests an original method to excite plasmons that overcomes the current technical difficulties and would simplify the experimental set-ups [Zayats05].

6.4 Stationary solutions

In this section, the aim is to proof the existence of stationary soliplasmon solutions. They are first obtained theoretically in section 6.4.1 and computed numerically in 6.4.2. After that, the transition to the more realistic configuration MK is proposed and numerically seen to be qualitatively similar to the MDK one, differing mainly in a SPP propagation constant, which is shifted by the nonlinearity.

6.4.1 Metal-Dielectric-Kerr media

Looking for stationary solutions of eqns. 6.12 and 6.13 in the form $c_{p,s}(z) = c_{p0,s0} e^{i\mu z}$ gives the eigenvalue equation

$$\begin{bmatrix} \mu_p & q \\ \bar{q} & \mu_s \end{bmatrix} \begin{bmatrix} c_{p0} \\ c_{s0} \end{bmatrix} = \mu \begin{bmatrix} c_{p0} \\ c_{s0} \end{bmatrix}, \tag{6.27}$$

which solutions are

$$\mu_\delta = \langle \mu \rangle + e^{i\delta} \sqrt{\Delta_\mu^2 + q\bar{q}},\ \delta = 0, \pi, \tag{6.28}$$

where $\langle \mu \rangle \equiv [\mu_p + \mu_s]/2$ is the propagation constant mean value and $\Delta_\mu \equiv [\mu_p - \mu_s]/2$ a detuning. For an arbitrary c_{s0}, the eigenvectors read

[4] In the derivation of eq. 6.10, the vectorial term concerning the soliton, $\overrightarrow{\nabla}\left(\epsilon_L^{-1}\overrightarrow{\nabla}\epsilon_L c_s(z)\hat{u}f_s\right)$, has been neglected by considering the soliton as a scalar wave, i.e. $\overrightarrow{\nabla}\mathcal{E} \approx 0$. The Maxwell equation $\overrightarrow{\nabla}\overrightarrow{\mathcal{D}} \equiv 0$ then implies that $\overrightarrow{\nabla}\epsilon_L \approx 0$ too (see e.g. eq. 5.16). However, if the soliton tail is to excite an initially non existing SPP through its interaction with the metal, at least this little part of the soliton tail must be vectorial and thus $\overrightarrow{\nabla}\left(\epsilon_L^{-1}\overrightarrow{\nabla}\epsilon_L c_s(z)\hat{u}f_s\right) \neq 0$. Evaluating this term at the metal interface ($x = 0$) and projecting it with the plasmon field, the driving coefficient $q \to q + \Delta$, $\Delta \sim c_s e^{-\kappa_s a}\partial_x(1/\epsilon_L)|_{x=0}$. This term is in principle not well defined if one is limited to discrete boundaries and quantifying it is beyond the scope of this thesis. The main reason for this is that Δ has the same physical meaning than q, i.e., provides SPP growth throught the soliton tail $e^{-\kappa_s a}$.

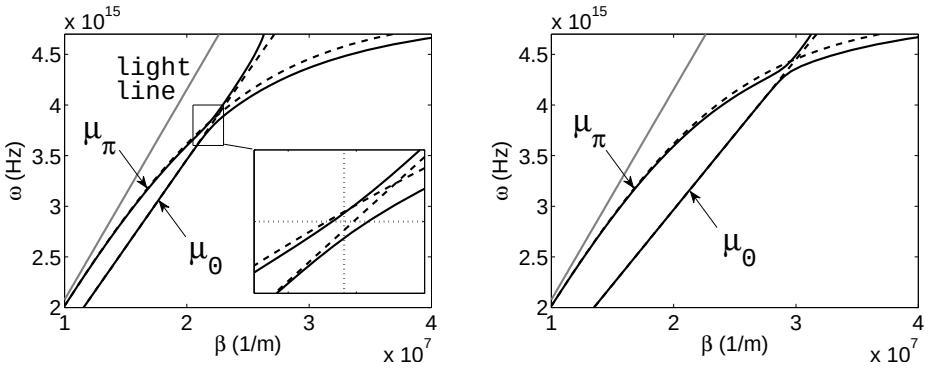

Figure 6.2: Soliplasmon dispersion for soliton peak power levels (a) $g|c_s|^2 = 0.2$ and (b) $g|c_s|^2 = 0.4$. Dashed lines correspond to dispersion of soliton and SPP, separately (as in fig. 6.1).Grey line marks the light line $\omega = \beta c/\sqrt{\epsilon_d}$. Inset in (a) zooms in the anti-crossing region and the intersection of the dotted lines mark the predicted anti-crossing point.

$$| \mu_\delta\rangle = c_{s0} \begin{bmatrix} q/(\mu_\delta - \mu_p) \\ 1 \end{bmatrix} \tag{6.29}$$

and the ansatz in eq. 6.8 takes the explicit form

$$\frac{\mathcal{E}_x(x,z)}{c_{s0}} = \left\{ \frac{q}{\mu_\delta - \mu_p} e_p(x) + sech(\kappa_s(x-a)) \right\} e^{i(kn_k + \mu_\delta)z}, \delta = 0, \pi. \tag{6.30}$$

Note from eq. 6.28 that $\mu_0 > \mu_{s,p}$ and $\mu_\pi < \mu_{s,p}$, so the relative sign between the soliton and plasmon fields is $e^{i\delta}$ and δ has the meaning of the soliplasmon supermode phase. Modes with $\mu_{\delta=0} > \mu_{s,p}$ are referred to as 0-soliplasmons, whereas those with $\mu_{\delta=\pi} < \mu_{s,p}$ are π-soliplasmons, being $\mu = \mu_p$ a phase singularity point, where the electric field takes the form of a SPP wave with zero soliton component.

Dispersion relations of soliplasmons $\beta_{sp}(\omega) \equiv kn_k + \mu_\delta(\omega)$ (μ_δ given in eq. 6.28) are plotted in fig. 6.2. The position of the resonance, the anti-crossing point, shifts towards bigger ω with soliton peak power, as a consequence of its enhanced effective index, which decreases its dispersion slope, $c/[n_k(1 + g|c_s|^2)]$.

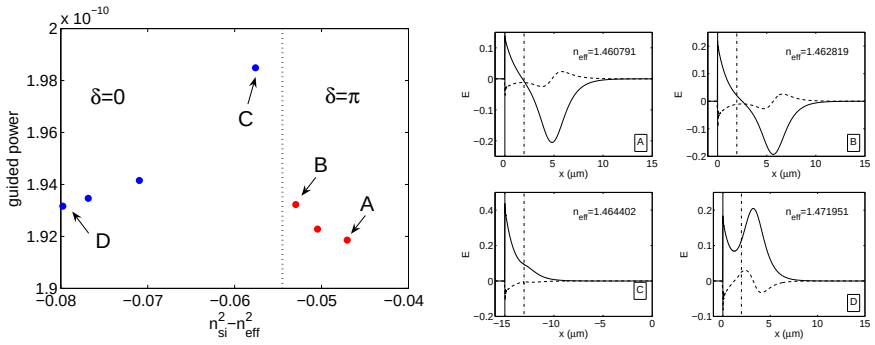

(a) (b)

Figure 6.3: (a) Soliplasmon guided power in the MDK configuration, as a function of the index contrast, $\bar{\mu} \equiv n_{si}^2 - n_{eff}^2$, where $n_{si} = 1.4446 = n_{d,k}$. Dotted vertical line marks the $\bar{\mu}_p \equiv n_{si}^2 - (\beta_p/k)^2$. (b) x (solid) and z (dashed) components of the stationary solutions $\vec{E} \equiv \sqrt{\chi^{(3)}}\vec{\mathcal{E}}$ corresponding to the points A-D in (a). The vertical lines at $x = 0$ and $x = 2/k_d \approx 2.4\mu$m mark the metal-dielectric and dielectric-Kerr interfaces, respectively.

6.4.2 Numerical results: P-μ resonance and δ-soliplamons

The computation of the nonlinear modes is done from eq. 5.17, with the substitution of ϵ_L by the $\epsilon = \epsilon_L + \chi^{(3)}\left[|\mathcal{E}_x|^2 + |\mathcal{E}_z|^2\right]$, assuming the latter in scalar form for simplicity (the numerical method to find the stationary solutions is explained in detail in appendix A). When projecting eq. 5.17 onto the $\hat{XZ}$ plane, a system of two coupled equations for $\mathcal{E}_x$ and $\mathcal{E}_z$ is obtained. The fact that SPP waves are characterised by a strong component of the electric field perpendicular to the metal yields to $|\mathcal{E}_z| << |\mathcal{E}_x|$, so our attention is focused on the equation for $\mathcal{E}_x$, which can be assumed to be real, without loss of generality, by subtracting a global phase. On the other hand $\mathcal{E}_z$ satisfies

$$\mathcal{E}_z = -\frac{i}{\beta_{sp}}\left[\epsilon^{-1}\partial_x(\epsilon\mathcal{E}_x)\right], \tag{6.31}$$

what can be obtained from the Maxwell equation 2.1. This gives us the simple eigenvalue equation for the $\mathcal{E}_x$ component

$$\hat{\mathcal{L}}_{1D}\mathcal{E}_x = \beta_{sp}^2\mathcal{E}_x, \tag{6.32}$$

with

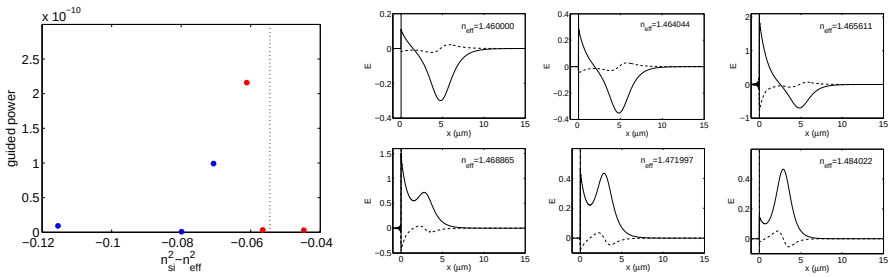

(a) (b)

Figure 6.4: Stationary soliplasmons for MK media. Red (blue) dots in (a) correspond to the $\delta = \pi$ ($\delta = 0$) modes plotted in the top (bottom) row of (b). Dashed line in (a) corresponds to the linear SPP, as in fig. 6.3.

$$\hat{\mathcal{L}}_{1D} \equiv \partial_x^2 + \partial_x \left(\frac{1}{\epsilon} \partial_x \epsilon \circ \right) + k^2 \epsilon. \tag{6.33}$$

Fig. 6.3a shows the soliplasmon normalised guided power, $\gamma P \equiv \int_{\hat{x}} dx S_z$ ($S_z \equiv \frac{1}{2}\mathrm{Re}\left\{\gamma \mathcal{E}_x H_y^*\right\}$), vs the index contrast, $\bar{\mu} \equiv n_k^2 - n_{eff}^2 = -2n_k\mu/k$, for several modes. The asymptotic behaviour is insinuated and the E_x ($\equiv \sqrt{\chi^{(3)}}\mathcal{E}_x$) profiles show the predicted phases $\delta = 0, \pi$ at each side of μ_p, according to eqns. 6.28, 6.30.

6.4.3 Metal-Kerr media

Although more realistic (in principle), a theory based on the MK configuration would complicate the variational approach developed in section 6.3, mainly because the NL-SPP field profiles, which may vary substantially from the linear ones, remain unknown to us. XPM terms could still be neglected in a weakly coupling scheme, since they are not our primary interest in this present work. Indeed, numerical solutions of the MK media are found using the method in section 6.4.2 for MDK. The main conceptual implication of the MK interface is that the SPP increases its wavenumber due to nonlinearity.

Fig. 6.4 shows soliplasmons modes, equivalently to fig. 6.3. The main difference is the shift of the vertical asymptote towards bigger $n_{eff} = n_p + \Delta n_p$. In fact, $\Delta\bar{\mu} \approx 0.1$ yields to $\Delta n_p/n_p \approx 0.2\%$, what an expectable index shift for the SPP in silica glass.

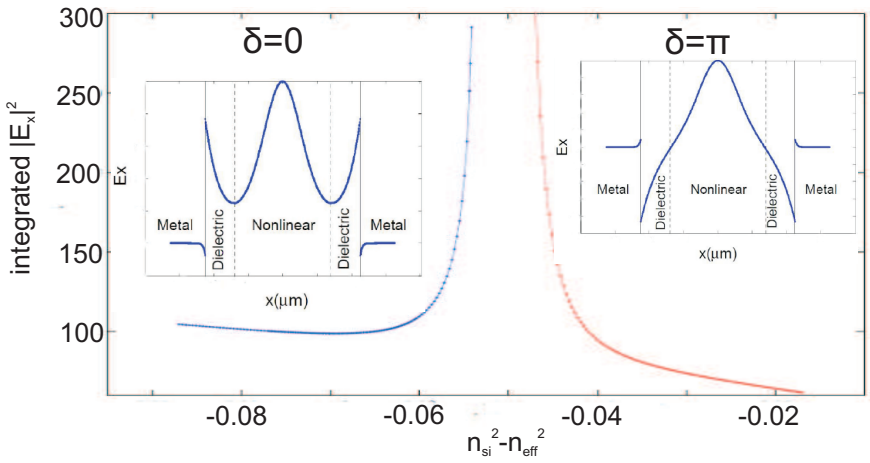

Figure 6.5: Stationary soliplasmons for the MDKDM waveguide.

6.4.4 A note on the soliplasmon waveguide: Metal-Dielectric-Kerr-Dielectric-Metal structure

The most important numerical issue in the computation of soliplasmons, which is not solved here yet, is keeping the soliton position fixed to $x_s = a$. The small variation of x_s from one solution to another does not let us reproduce in great detail the predicted resonant trend in eq. 6.30. To this end, the waveguide configuration MDKDM, with the metal interfaces at $x = 0, 2a$, and $x_s = a$, was considered. Assuming well defined symmetry for the two SPP's implies the theoretical model is only affected by the change $\bar{q} \to 2\bar{q}$ in eq. 6.13. Fig. 6.5 plots the integrated $|E_x|^2$ vs $\bar{\mu}$ curves, proving the resonance and showing the different curvatures in a much clearer way.

6.5 Stability analysis: amplitude-phase dynamics

Four of the stationary solutions shown in fig. 6.4b are exposed numerically to conservative stability analysis, i.e., propagation over long distances ($> 60\mu$m) with input noise and without ohmic losses ($\epsilon_m \in$ Re). The very well known Vakhitov-Kolokolov (VK) stability criterion [Vakhitov73] predicts that a curvature $d|E|/d\beta_{sp} < 0 (> 0)$ (note $\bar{\mu} \sim -\beta_{sp}$) corresponds to stable (unstable) stationary solutions. The great detail provided in fig. 6.5 suggests that the ($\delta = \pi$)-soliplasmons should be stable NL solutions. Indeed, fig. 6.6a,b shows that the propagation of the $\delta = \pi$ solutions with $n_{eff} = 1.46000$, $n_{eff} = 1.464044$ along 60 μm occurs in a very stationary manner.

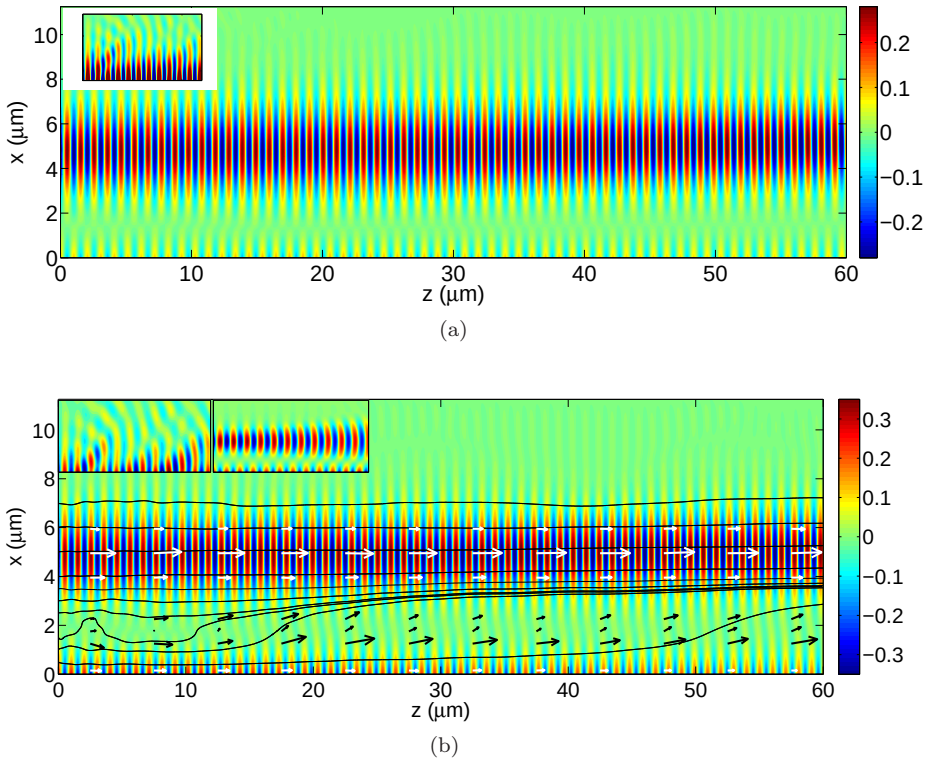

Figure 6.6: Propagation of the (a) $n_{eff} = 1.46000$ and (b) $n_{eff} = 1.464044$ soliplasmons, shown in figs. 6.4b, along 60 μm. Insets in (a) and (b) magnify $|E_x|$ over the area where they are placed, showing the noise is ejected away during the first 12 μm. Second inset in (b) shows the first 12 μm of propagation in the linear regime, with clear soliton diffraction signatures. (b) includes stream lines a flux arrows (being the black ones magnified) to visualise the energy transfer.

Apart from being diffraction free, the input noise used for all the propagations introduces fluctuations of the 20% in the amplitude and it is seen to propagate away the soliplasmon towards $x > 0$ (see inset of fig. 6.6a[5]).

0-soliplasmons, however, lie on a curve where $d|E|/d\bar{\mu} < 0$ for $\bar{\mu} \ll \bar{\mu}_p$ and $d|E|/d\bar{\mu} > 0$ for $\bar{\mu} \lesssim \bar{\mu}_p$. Fig. 6.7a shows the propagation of the $n_{eff} = 1.471997$ 0-soliplasmon (see fig. 6.4b), which is clearly a non-stationary evolution. Interestingly, it is associated with the dynamics of the soliplasmon phase, ϕ_{sp} (fig. 6.7)b), and the

[5]Numerical checks to compare linear (diffractive) vs nonlinear (non-diffractive) modelling and to observe the expulsion of the input noise have been done for all the cases, but only this representative examples in the insets of fig. 6.6 are shown.

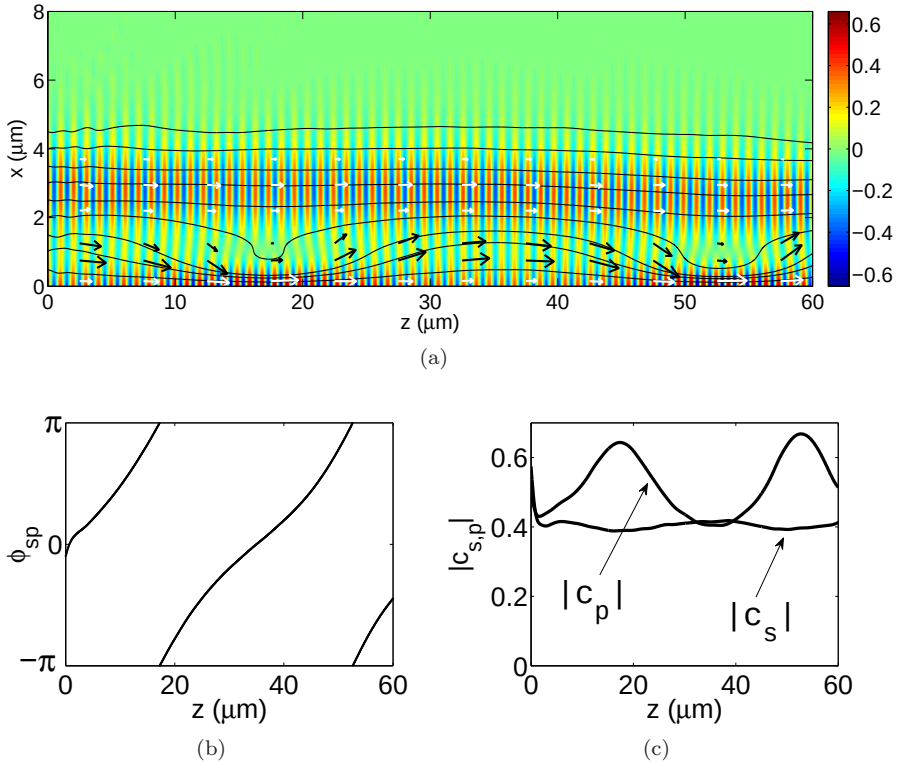

Figure 6.7: Evolution along 60μm of the $n_{eff} = 1.471997$ 0-soliplasmon. (a) norm of the electric field $|E_x|^2$, (b) soliton-plasmon relative phase ϕ_{sp} and (c) soliton and plasmon amplitudes $|c_{s,p}|$. Sharp initial jumps are due to the large input noise $\sim 20\%$ in amplitude. (a) includes stream lines a flux arrows (being the black ones magnified) to visualise the energy transfer.

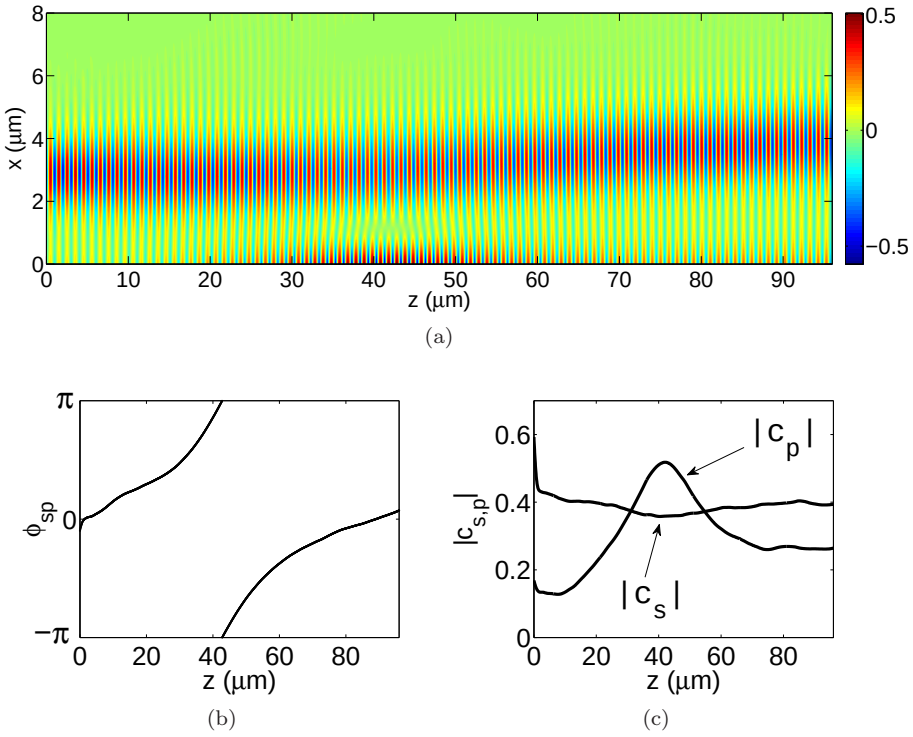

Figure 6.8: Same as fig. 6.7 for the $\delta = 0$ solution with $n_{eff} = 1.484022$.

amplitudes, $c_{s,p}$ (fig. 6.7c,d), whereas the soliton position stays approximately steady around $x_s = a$ (fig. 6.7a). We speculate that this soliplasmon is in the $d|E|/d\bar{\mu} > 0$ unstable region (unfortunately not apparent in fig. 6.4a) so instability seems to be associated with the soliplasmon parameters dynamics, rather than with a destruction of the solution (at least for the distances shown here).

The amplitude-phase oscillations seem to occur in this case in the following qualitative way. The initial soliton tail that reaches the metal interface pumps the SPP wave, what rises $|c_p|$, β_p, decreases $|c_s|$, β_s and a velocity miss-match is induced between the soliton and plasmon, with the corresponding increase of ϕ_{sp}. At $z \approx 18\mu$m, $\phi_{sp} = \pi$ and the stable π-soliplasmon can not be formed due to their different velocities. As they come back on phase, the SPP returns some of the energy to the soliton channel and the initial parameters are approximately restored at $z = 35\mu$m. In this particular example, the soliton is slowly attracted towards the interface, but it is not possible to explain the dynamics further with our current knowledge.

The solution with $n_{eff} = 1.484022$ and $\delta = 0$ (fig. 6.4b) is further away from $\bar{\mu}_p$ (than the one with $n_{eff} = 1.471997$) and thus expected to behave in a (more) stable manner. From fig. 6.8, we see that it needs larger propagation distances (now $z = 96\mu$m) to develop the $\phi_{sp}, c_{s,p}$ oscillations (the fact that these are still generated invites us to locate it in the $d|E|/d\bar{\mu} > 0$ too).

In this case, the initial SPP is very small, $|c_s|/|c_p| \approx 3$, so the soliton needs $\sim 30-40\mu$m to excite it. Apart from the soliton position, the first $\sim 60\mu$m are qualitatively similar to those of fig. 6.7. However, in the last $\sim 40\mu$m the interaction between the SPP and the refracted soliton is minimised. Clear features of that are the constant values reached by the quantities $d^2\phi_{sp}/dz^2$, $d^2a/dz^2 \approx 0$ and $|c_p|$. Presumably, the prolonged lack of a SPP in the initial stages exposed the soliton too much to the metal repulsion (reflection).

Greater n_{eff}'s should eventually recover a purely spatial soliton solution, which is known to be stable (see e.g. appendix A of [Biancalana05] for the formal and equivalent proof for the case of temporal bright solitons), and thus $d|E|/d\bar{\mu} < 0$ should be recovered too, in agreement with the numerical calculations of fig. 6.5. 0-soliplasmons are then thought as being conditionally stable below a critical $\bar{\mu} < \bar{\mu}_p$ value.

6.5.1 Effect of metal losses

Taking into account realistic metal losses is essential for practical realisations (see chapter 5 and [Milián11]). Only to give an idea of its influence, fig. 6.9 shows the

propagation under the same initial conditions as fig. 6.7, and comparison is made between the two figures. The first stage of 20μm in which the soliton pumps the SPP are very similar and losses have a small effect. However, as soon as phase reaches $\phi_{sp} = \pi$, the energy transfer is stopped and $|c_p|$ drops dramatically ($\sim 80\%$) due to losses. This reduces β_p, SPP accelerates and ϕ_{sp} decreases towards the initial value 0, not 2π as in the loss less case. Again, exposure to metal repulsion bends soliton trajectory and it goes away from the interface, leaving behind a SPP that will be exponentially attenuated by the ohmic losses.

The fact that the energy transfer stops at $\phi_{sp} = \pi$ gives a qualitative reason of why stable soliplasmons (with $|c_s| \approx |c_p|$) are the ones with $\delta = \pi$. The nodal point in the amplitude of the strongest component $\mathcal{E}_x$ (see fig. 6.3b and 6.4b) frustrates an efficient energy transfer between solitonic and plasmonic components, so $\phi_{sp}(z) = 0$ and $\beta_s(z) = \beta_p(z) = \beta_{sp}$.

6.6 Conclusions

In this chapter, the soliplasmons, a new type of hybrid nonlinear bound states, have been presented. The properties of the stationary solutions have been well predicted by a forced oscillator model, and their stability has been explained qualitatively. However, many opened problems are left opened (see chapter 8), among which are the study of the dynamics associated to the instability, considering further degrees of freedom such as the soliton position and, of course, the dynamics close to the resonant points, in which the effects are expected to develop over shorter lengths and the excitation of SPP waves from a soliton is to be explored.

A crucial point to address in general in plasmonic systems is the effect of the Ohmic losses. In this case two important points are to be mentioned. First, in this system the spatial soliton acts as a reservoir for the plasmon as shown in fig. 6.9, so the latter propagates for longer distances than a single SPP wave. Second, in the single interface scenario the soliton suffers from reflections if the SPP becomes very weak. In principle this could be solved by considering the waveguide in fig. 6.5, although asymmetric modes could lead to soliton crashing in an interface. Again, as in the last chapter, inclusion of gain in the dielectric to compensate for losses might lead to interesting results.

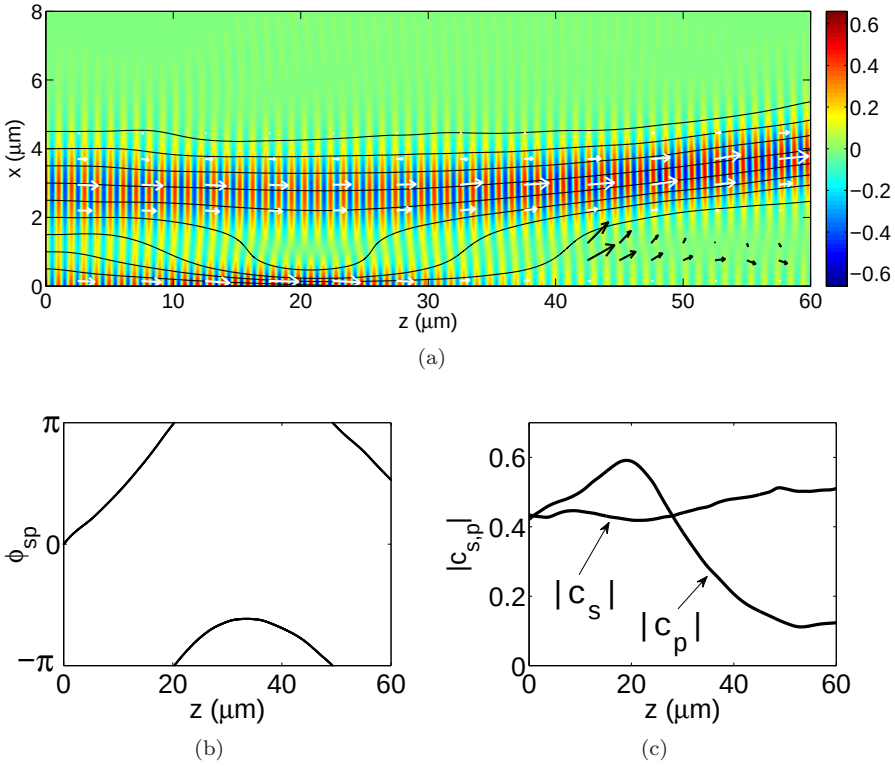

Figure 6.9: Same initial conditions as in fig. 6.7 but accounting now for the meatl losses, $\epsilon_m = -82 + i8.3$.

Chapter 7

Optimisation of a fibre based narrow-band optical source in Grid platform

This brief chapter describes the progress made in a broad collaborative frame[1] towards the optimization of optical fibre spectra (SC related dynamics) using automated procedures based on Genetic Algorithms (GA). Large amount of computations involved in the optimization process invite to use Grid technologies that are able to cope with the computational requirements. Here it is described the integration of a service-oriented Grid meta-scheduler and a Genetic Algorithm, in order to create an automated tool which is able to find optimal solutions to our problem. The developed tool provides an scalable solution to computationally intensive problems and enables the optimization of other more complex fibre designs.

Section 7.1 motivates and describes the optimisation problem. Sections 7.2 and 7.3 describe the algorithm chosen for our particular application and the grid service, respectively. Finally, the results achieved with this approach are presented in section 7.4.

7.1 Motivation and case study

Dynamics associated with nonlinear partial differential equations is usually non trivial. In the previous chapters, several problems of this nature have been studied in detail

[1]Grid support and technical information in section 7.3 was provided by Germán Moltó (gmolto@dsic.upv.es). Java code implementing the chosen algorithm was developed by Miguel Arevalillo (miguel.arevalillo@uv.es), who also provided details for section 7.2.

and in all of them there were parameters, characterising either the incident light or the device geometry, that required to be optimised in order to obtain the desired functionality. This was successfully achieved in a simple way through the intuition and knowledge gained for those cases. In particular, physics underlying SC generation in the fs regime is very well known nowadays, [Skryabin10], what opens a scope for engineering problem proposals.

Our purpose here is to optimise the width, τ, carrier wavelength, λ_0 and peak power, P, of the input pulse, for the output of an $L \equiv 1$cm long fibre to produce an output spectrum which power is maximised in a predefined interval. This type of problems are important for applications in nonlinear microscopy of biological samples [Aviles-Espinosa11], where it is often needed to excite certain transition(s) of a biological molecule, with a wavelength that is not efficiently provided by standard sources. From the numerical point of view, it is important to give a solution with a relatively fine precision.

Intuition is not expected to be in general enough for this type of problems and an optimisation strategy should be designed. The challenge in doing so relies on the definition of a suitable optimisation criterion, *fitness function*, and an efficient algorithm to find the optimal solutions. For this purpose genetic algorithms (GA) have been chosen.

The propagation of the pulse is assumed (at least one m_k must be zero)to be described by the NLSE plus TOD and Raman effect (see eq. 2.32),

$$-i\partial_z A(z,t) = \left[-\frac{\beta_2}{2}\partial_t^2 - i\frac{\beta_3}{6}\partial_t^3\right] A(z,t) + \gamma A(z,t)\int_{-\infty}^{\infty} dt_1 R(t_1)|A(z,t-t_1)|^2. \quad (7.1)$$

Dispersion parameters take the values $\beta_2 = -11.83ps^2/\text{Km}$, $\beta_3 = 0.08ps^3/\text{Km}$ at the reference wavelength $\lambda_{ref} \equiv 780$nm, and the nonlinear coefficient $\gamma = 0.11/\text{W/m}$, as in [Ranka00, Dudley06]. Dispersion terms $\sim \beta_k, k \geq 4$ have been neglected because the primary interest here is to test the optimisation tool. By changing the pump wavelength, λ_0, the GVD takes the values $\beta_2(\lambda_0) = \beta_2 + 2\pi c\beta_3(1/\lambda_0 - 1/\lambda_{ref})$, where $c \equiv 2.99792458$m/s. Initial peak power of the input pulses, $\sqrt{P}sech(t/\tau)$, is expressed as $P = [1+63\alpha]|\beta_2(\lambda_0)|/(\gamma\tau^2)$, so $\alpha \in [0,1] \implies$ a soliton order $N \in [1,8]$ ($N \equiv \tau\sqrt{\gamma P/|\beta_2(\lambda_0)|}$).

The optimisation problem consists in finding the initial $\alpha \in [0,1]$, $\lambda_0 \in [700,900]$nm and $\tau \in [0.01, 0.050]$ps, that maximise the spectral output power in the range of frequencies $\omega \in [1780, 1820]$THz, what corresponds to the vacuum wavelength interval $\lambda \in [1035, 1060]$nm. Thus, the fitness function to minimise is defined here simply as

$$\Phi \equiv \left[\int_{\omega_1}^{\omega_2} d\omega |\tilde{A}|^2\right]^{-1},\ \omega_1 = 1780THz,\ \omega_2 = 1820THz. \tag{7.2}$$

The frequency interval was intentionally located in the anomalous GVD region (see section 7.4). For that, its width was set to the approximate expected width of a foundamental soliton. Particular values for $\omega_{1,2}$ where chosen around the centre of the spectral region covered by the solitons in the different simulations that are possible, according to all the possible values of τ, λ_0 and α.

Eq.7.1 is solved numerically by a matlab code that implements the 4th order Runge-Kutta method to discretise the z-derivative. Fast Fourier transform routines, *FFT*, *IFFT*, are used for the rest of the operations. They speed up the calculations because derivative operators ∂_t^m and convolution $R \star |A|^2(t)$ in eq. 7.1 simplify to direct products $(\omega - \omega_0)^m$ and $\tilde{R}\widetilde{|A|^2}(\omega - \omega_0)$, respectively, in the reciprocal Fourier space (denoted by the tildes on top of the functions).

7.2 The genetic algorithm

Minimisation problems can be solved by using deterministic or meta-heuristic algorithms. The latter are required when exhaustive enumeration of the search space becomes impractical. For that, a shorter runtime is achieved by accepting solutions which approximate a global optima, but may not exactly match it. Genetic Algorithms (GA) are a class of meta-heuristic evolutionary algorithms, and consider each genome $\mid g\rangle \equiv [g_1, g_2, g_3]^T = [\tau, \lambda_0, \alpha]^T$, representing each simulation, as an *individual* of the population. They place a special emphasis on the application of genetic operators, to approach optimal solutions. These are mainly the identity operator $\hat{\mathcal{I}}$, random generation $\hat{\mathcal{R}}$, mutation $\hat{\mathcal{M}}$ and crossover $\hat{\mathcal{X}}$.

Random generation is regarded as

$$\hat{\mathcal{R}} \mid \phi\rangle \equiv \begin{bmatrix} R_1 & 0 & 0 \\ 0 & R_2 & 0 \\ 0 & 0 & R_3 \end{bmatrix} \mid \phi\rangle \rightarrow \mid g\rangle, \tag{7.3}$$

R_k are the random generators obeying the uniform statistical distribution. $\mid \phi\rangle$ is the zero or *vacuum* state, so $\hat{\mathcal{R}}$ plays in eq. 7.3 the role of a creation operator, resembling $a^\dagger$ in quantum field theory (QFT), or $\hat{\chi}^{(0)}$ in optical media with electric dipole moment in the absence of external field (see discussion in section 2.1.1).

The mutation process $\hat{\mathcal{M}} :\mid g\rangle \rightarrow \mid g'\rangle$ uses the well-known polynomial mutation [Deb01] for real coded problems (continuous valued variables), and generates the new

genes

$$g'_k = g_k + m_k \Delta_k \bar{\delta}_k;\ m_k \equiv \mathrm{H}(u_k - \frac{2}{3}), \tag{7.4}$$

where Δ_k is half of the allowed interval for each variable ($\Delta_\tau = 20$ fs, $\Delta_\lambda = 100$ nm, $\alpha = 1/2$), H is the Heaviside step function and $u_k \in [0,1]$ a uniform random number. The latter implies that in average, one gene is mutated per individual when mutation is applied (a rate of one mutation per individual). $\bar{\delta}_k \in [-1,1]$ satisfies the (normalised) probability distribution $\mathcal{P}_m(\delta) = 0.5[n + 1[1 - |\delta|]^n]$ and $n = 20$ (see 7.1a). $\mathcal{P}$ becomes the normal distribution for $n = 0$ or it is very peaked around zero for $n \gg 1$, so it is clearly distinguished from R_k. The stochastic variable is chosen via a new random $u_k \in [0,1]$

$$\bar{\delta}_k = \delta \ / \int_{-1}^{\delta} \mathcal{P}_m(\delta) = u_k;\ u_k \in [0,1]. \tag{7.5}$$

Cross-over is the process by which two *childs* $\mid g_c^{1,2}\rangle$ are generated by a combination of two existing *parents*, $\mid g_p^{1,2}\rangle$, without destroying the lattes, i.e., $\hat{\mathcal{X}}[\mid g_p^1\rangle^T, \mid g_p^2\rangle^T, \mid \phi\rangle^T, \mid \phi\rangle^T]^T = [\mid g_p^1\rangle^T, \mid g_p^2\rangle^T, \mid g_c^1\rangle^T, \mid g_c^2\rangle^T]^T$. We have used SBX (Simulated Binary Crossover) [Agrawal94] and it can be expressed as the $[12 \times 12]$ operator

$$\hat{\mathcal{X}} \equiv \begin{bmatrix} \hat{\mathcal{I}} & \hat{0} & \hat{0} & \hat{0} \\ \hat{0} & \hat{\mathcal{I}} & \hat{0} & \hat{0} \\ \hat{\alpha}_+ & \hat{\alpha}_- & \hat{0} & \hat{0} \\ \hat{\alpha}_- & \hat{\alpha}_+ & \hat{0} & \hat{0} \end{bmatrix};\ (\hat{\alpha}_\pm)_{jk} \equiv x_k \frac{1 \pm \bar{\beta}_k}{2} \delta_{jk},;\ x_k \equiv \mathrm{H}(u_k - 0.05), \tag{7.6}$$

where $\hat{0} \equiv 0 \times \hat{\mathcal{I}}$. The crossover *activators*, x_k, set a probability for cross over of 95% per gene and the deffinition of $(\hat{\alpha}_\pm)_{jk}$ ensures the average value of each parameter is preserved after the crossover operation, $|g_{pk}^2 - g_{pk}^1| = |g_{ck}^2 - g_{ck}^1|$. The stochastic variables for crossover, $\bar{\beta}_k$ (see 7.1b), are also chosen from random $u_k \in [0,1]$,

$$\bar{\beta}_k = \beta \ / \int_0^{\beta} \mathcal{P}_x(\beta) = u_k;\ \mathcal{P}_x(\beta) = \begin{cases} 0.5(n+1)\beta^n,\ \beta \leq 1 \\ 0.5(n+1)\beta^{-(n-2)},\ \beta > 1 \end{cases} \tag{7.7}$$

Note the certain similarity between $\hat{\mathcal{X}}$ and the optical $\hat{\chi}^{(3)}$, which mediates the interaction between two *input* and *output* fields.

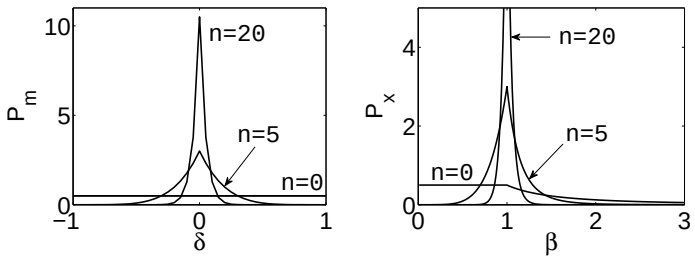

Figure 7.1: Probability distributions for the stochastic variables involved in (a) polynomial mutation and (b) simulated binary crossover.

7.2.1 Steady state algorithm

Most of traditional GA are *generational*, i.e., start from a randomly generated population and the most promising individuals are allowed to reproduce to determine the next generation of individuals, according to the pre-established evolution rules (parent selection method, definition of $\hat{\mathcal{M}}$, $\hat{\mathcal{X}}$ and their rates, to obtain the offspring for the next generation). Most parent selection methods are stochastic in order to keep the diversity of the population, preventing premature convergence to a sub-optimal solution.

In our particular problem, no prior knowledge about the search space is assumed, and a rugged landscape $\Phi(\tau, \lambda_0, \alpha)$ is expected. Indeed, there exist efficient evolutionary algorithms for general purpose applications. As an example, CMA-ES (Covariance Matrix Adaptation Evolutionary Strategy) [Hansen03, Hansen96] is an evolutionary algorithm for difficult non-linear non-convex optimisation problems in rugged search spaces. However, our interest is in problems in which the fitness function may have a varying computational cost (ranging from minutes to several hours). Under these circumstances, the paralleling of generational algorithms in a Grid may not be an efficient approach. Instead, a steady state genetic algorithm has been used, changing one member of the population at a time. This allows computation of several fitness in parallel (after an initial population has been built) and processed once they are available. To this end, a *replace the worst* strategy has been adopted, which fully exploits the processing power of the Grid, keeping it constantly computing new individuals. In its current state, the algorithm lets a user to modify the following parameters:

- n: approximate number of computing elements simultaneously in the Grid. This is used to determine the number of processors needed.

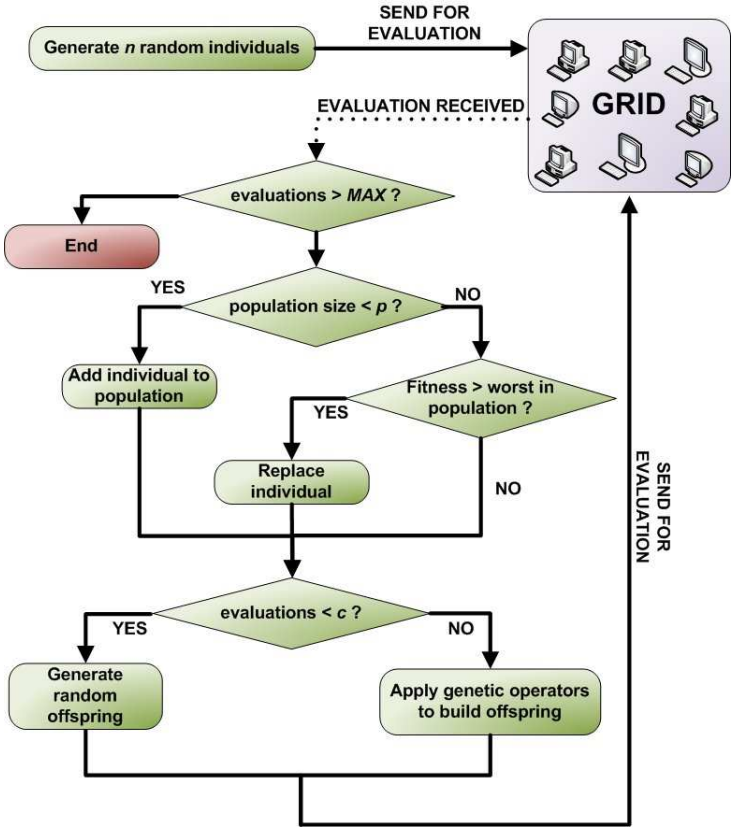

Figure 7.2: Scheme of the steady state GA.

- p: population size.

- MAX: maximum number of evaluations to perform, after which the smallest fitness value and input parameters are returned.

- c: number of individuals which are generated before any genetic operator (selection, crossover and mutation) is applied. The algorithm is then initiated with c randomly generated seeds.

Figure 7.2 provides a flowchart of the algorithm, which in the first stage decides what to do with the generated individuals and in the second, how to make the new ones. In the former, a newly generated individual is added to the population (regardless its Φ) if the size is less than p. If the current population is already p, the new candidate replaces the individual with the worst (biggest) Φ if any, or it is discarded. The second stage is to generate new off-springs to be sent to the Grid for evaluation. This is done by $\hat{\mathcal{R}}$ if population is smaller than the threshold value c ($c < p$), or by the genetic operators $\hat{\mathcal{M}}$ and $\hat{\mathcal{X}}$ otherwise. In this latter case, the stochastic variables α_k^l, m_k and R_k and the relative weights between $\hat{\mathcal{M}}$ and $\hat{\mathcal{X}}$, w_m and w_x, play which is probably the most crucial point of the algorythm. Whilst $\hat{\mathcal{M}}$ provides diversity to the population, $\hat{\mathcal{X}}$ pulls the new individuals closer to the currently lowest Φ.

Generation is thus a not a well defined concept of our scheme, since an individual survival is guaranteed untill it becomes the worst one in the population. In that sense, the identity operator $\hat{\mathcal{I}}$ is always present in the system and only mutation and cross-over are explicitly applied to generate off-springs.

7.3 The Grid service

Current Grid computing technologies [Foster05] use standard protocols for sharing both computational power and data storage capacity among geographically distant resources. Therefore, they are an ideal infrastructure for the execution of the high throughput problem that lies beneath the optimization via Genetic Algorithms. We have used an integrated computational approach, using clusters of PCs within a Grid infrastructure (middle-ware). The usage of Grid protocols to support these executions makes it possible to provide the GA with an scalable[3] solution to its demanding computational requirements. If additional computational resources were required to speed up a problem, or to make it more complex (e.g., with more parameters), the Grid infrastructure could be enlarged, remianing unchanged the applications employed to

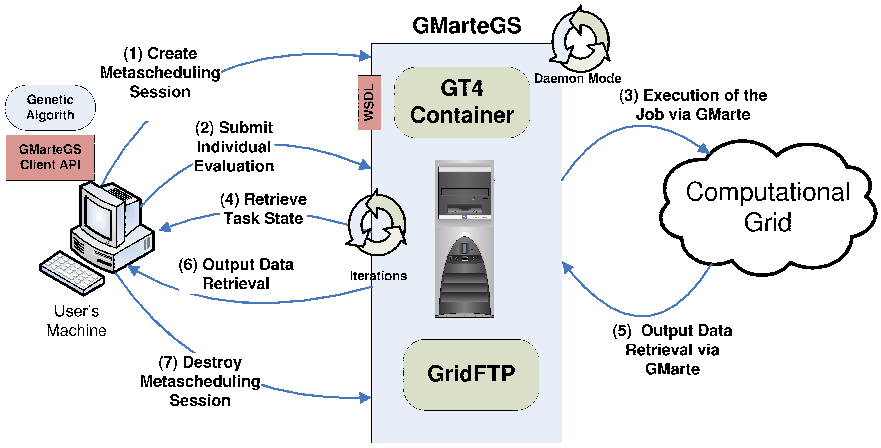

Figure 7.3: Interaction between the GA and GMarteGS.

submit the executions, thus reducing development efforts.

The following subsections briefly describe the GMarteGS service-oriented meta-scheduler employed to support the evaluation of individuals.

7.3.1 GMarteGS: A Service-Oriented Meta-Scheduler

GMarteGS [Moltó08] is a service-oriented facade to the GMarte [Alonso06] meta-scheduler. GMarte enables the reliable execution of high performance computing applications on Grid based on the Globus Toolkit (GT) [Foster05]. It manages the execution of the tasks by providing fault-tolerant data transfer services between the client machines and the remote computational resources. It also monitors the application during its lifetime to detect failures, which are silently handled by re-scheduling the tasks on other available resources.

GMarteGS is entirely developed in Java and uses common standards like the Web Services Definition Language (WSDL) and the Web Service Resource Framework (WSRF). It introduces secure multi-user resource brokering on computational Grids for the execution of computationally intensive applications. Its architecture allows different users to simultaneously use its functionality to submit the execution of tasks. In addition, the Grid service uses the Grid Security Infrastructure (GSI) provided by GT to achieve privacy between the client and the service, as the principal

[3]This is a crucial point which *Cloud Computing* actually solves in a more flexible way than Grid infrastructures. However, the fact that all the information is on the internet makes the cloud security protocols much easier to corrupt.

communications are ciphered, as well as data integrity.

Thus, GMarteGS acts as a mediator between the users and the Grid infrastructure. As such, it provides a high level Application Programming Interface (API), both in WSDL and in Java, which can be easily employed to incorporate its functionality to existing programs requiring the execution of tasks in a Grid infrastructure.

Figure 7.3 depicts the interaction between the genetic algorithm and the Grid service. First of all, the GA creates a session and then it starts the optimization strategy, according to fig. 7.2. When the GA requires an individual to be evaluated, it uses the GMarteGS Client API to define a new execution task with the appropriate parameters that describe the individual. This task is submitted to the Grid infrastructure and its state can be easily monitored via high level methods that describe the state of the task (i.e. scheduled, staged in, active, staged out, completed or failed).

7.3.2 Interfacing the Genetic Algorithm with GMarteGS

GMarteGS exposes its functionality via WSDL. Therefore, it can be accessed from virtually every possible application, regardless of the programming language used. However, as the Genetic Algorithm has also been implemented in Java, a lightweight client-side Java API was developed to ease the usage of GMarteGS from a client Java code. This includes methods and objects for defining tasks, creating sessions, gathering the state of the meta-scheduling sessions and their tasks, destroying sessions and transferring data between the client machine (where the GA runs) and the Grid service machine via the GridFTP protocol.

Gathering the state of the tasks is usually done actively (the client requests this information from the Grid service). However, GMarteGS also supports the standard notification mechanisms available in GT version 4 so that the client is notified whenever the state of a session (i.e., the state of any of its tasks) has changed. The main problem is that supporting notifications by the client requires that it deploys a GT4 container (at least the Java WS Core) to receive the incoming connections. This can be a drawback, as the client requires a special firewall configuration and can no longer be considered a thin client.

The application that evaluates the individuals has been implemented in Matlab. Although it is possible to create a re-distributable application which only depends on the Matlab runtime, this last piece of software is heavyweight and should be transferred to the remote computational resource along with the application. Therefore, to avoid this overhead we have relied on the installation of the required Matlab libraries in the remote computational resources. Once we have assessed the effectiveness of the

Φ_c			Φ_{min}		
τ	λ_0	N	τ	λ_0	N
11.7705	851.8005	7.0289	10.0097	840.3179	7.9987
11.0086	866.7541	5.7297	10.1034	843.1355	7.9635
15.1166	853.9194	7.6615	10.0037	775.0495	7.9996
10.2487	894.0204	5.3020	10.6762	848.0502	7.9903

Table 7.1: Input pulse parameters for the best fitness values found (left) in the first 35 randomly generated individuals, Φ_c, and (right) after $MAX = 1000$ individuals, Φ_{min}. Rows 1 to 4 correspond to figs. 7.4a,b, 7.5a and b, respectively.

optimization codes, a C-based version of the code would be able to seamlessly run on a wide variety of machines in a Grid infrastructure.

We have used a small Grid infrastructure which uses the Globus Toolkit 4.0.8 and is composed of two clusters of PCs (20 and 55 nodes) running on Intel Xeon 2.8 Ghz with 2.0 GBytes of RAM. A total of 12 such nodes have been used in this particular work. The execution of this case study required 90 minutes in the Grid infrastructure considered. Running the same GA in a single PC requires a total execution time of over 10 hours.

7.4 Results

In the experiments, we have used a population $p = 50$, and evaluated a total of $MAX = 1000$ candidate solutions to the problem. In order to achieve sufficient diversity amongst the initial population, $\hat{\mathcal{R}}$ generated the first $c = 35$ individuals. The particular deffinitions for n, m_k that has been reported to yield good results in a wide diversity of problems [Back93].

Figures 7.4 and 7.5 show the convergence process for 4 different optimisation runs. Top figures plot Φ for each generated individual in chronological order and the current smallest Φ (red line). Because the first $c = 35$ individuals are generated randomly, only the best fitness of that region, Φ_c, is marked.

Usefulness of a GA relies in both obtaining a substantially better fitness, Φ_{min}, than the one found randomly, Φ_c, and providing a qualitative criterion for convergence, which is provided by the approximately constant Φ along the last ~ 300 individuals. The former requirement gives typical values $\Phi_c/\Phi_{min} \in [3, 5]$, as can be seen explicitely in the plots (c) and (d). The spectral evolutions corresponding to Φ_{min} in each case are shown in plots (e), (f). Comparison

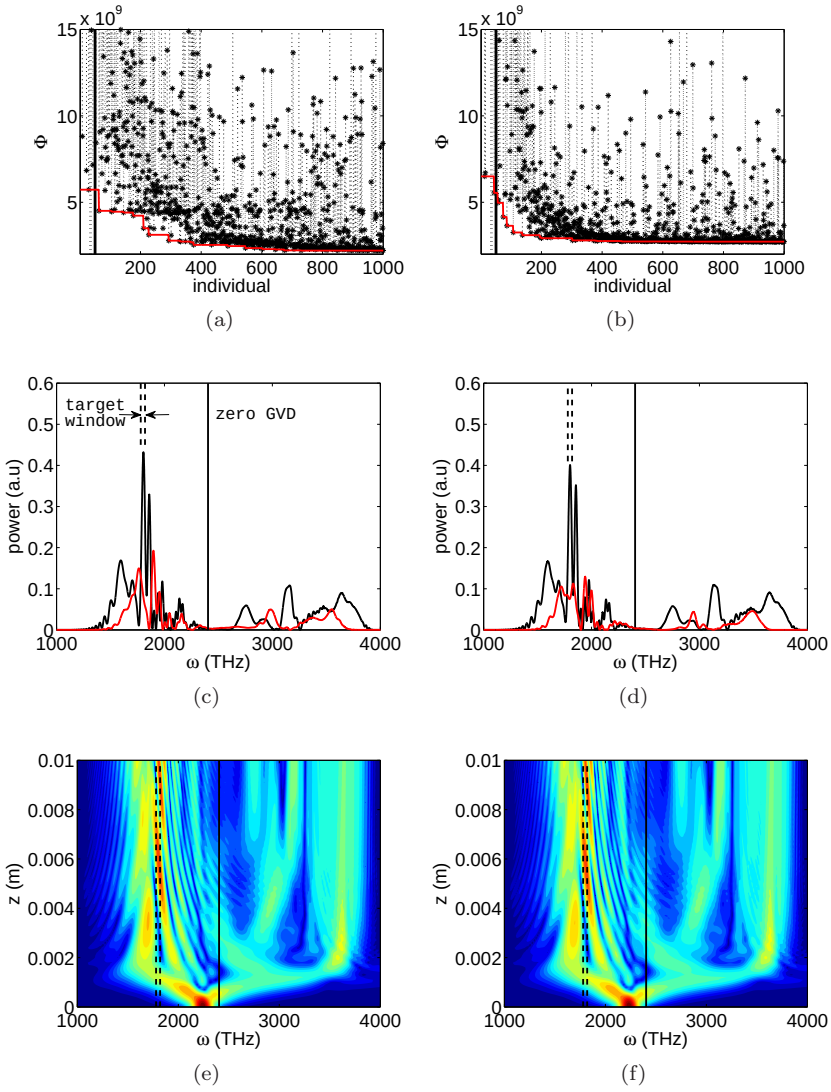

Figure 7.4: (a), (b) Evolution of fitness (stars), Φ, for the 1000 individual simulations. Dashed and full vertical lines mark cross-over threshold, $c = 35$, and population size, $p = 50$, respectively. Red line marks the best Φ. (c), (d) show the normalised output spectra corresponding to (red) Φ_c and (black) Φ_{min} (see table 7.1 for input parameter values). The spectral evolution of the optimum solutions are shown in figs (e), (f). In all spectral plots, full and dashed vertical lines mark the zero GVD and the target spectral window, respectively.

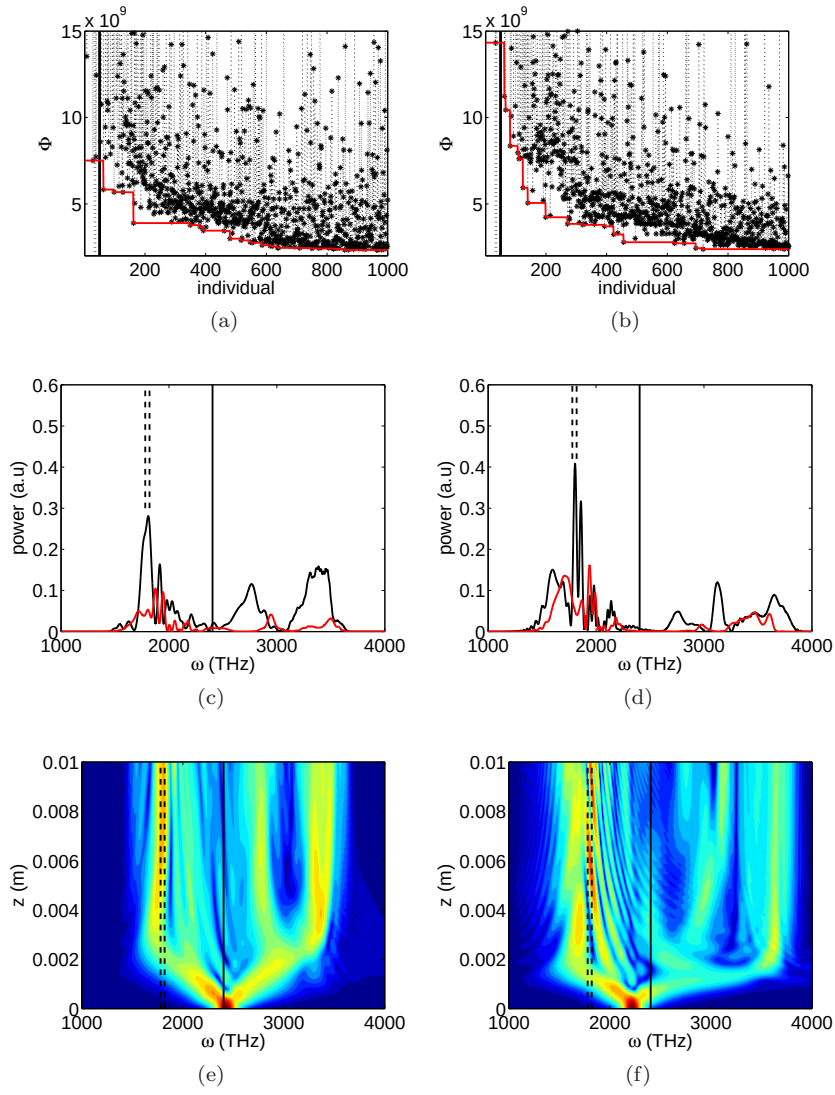

Figure 7.5: . Same as fig. 7.4, for other two optimisation executions.

The optimum solution found has the expected features. Indeed the narrow target spectral window imposed in this problem is likely to select peaked spectra, such that those of the bright solitons in the anomalous GVD regime. In this case, the GA provides a useful tool for a fine tuning of the input pulse parameters to achieve the required maximised spectral power.

The results presented here are the simplest possible approach towards a full optimization process not predictable, in principle, just on the basis of physical grounds. The results obtained in this section are promising and motivate the study of other more complex problems, e.g., involving other pulse parameters (e.g., chirp) or several fibres with different lengths and full dispersion profiles.

7.5 Conclusion

This chapter has presented the development of an automatic tool to optimize optical fibers based on Genetic Algorithms and supported by the computational power of a Grid infrastructure. In this case, we have used a simple genetic algorithm to find the best combination of parameters that leads to the maximised spectral power in a targeted window. It is believed that combining global optimization techniques with other local optimization strategies may considerably improve the results for certain classes of problems. Although we have used the software to solve an specific problem, the future work would be to build a library that allows the user to easily solve other optimization problems using Grid computing.

Chapter 8

Conclusions and future work

The work presented in this thesis belongs mainly to two different areas of photonics, i.e., supercontinuum generation in optical fibres and nonlinear effects in surface plasmon polariton SPP waves. In both areas, theoretical and numerical work has been developed. On the one hand, the theory work had the twofold purpose of, first, understanding the equations present in the current literature (chapter 2) and second, studying the complex nonlinear properties of *radiating dark solitons* (chapter 3) and the existence of *soliplasmon* solutions (chapter 6). On the other hand, the numerical work consisted, on the first stage, in developing our own codes for temporal propagation in optical waveguides with uniform and slowly varying cross-sections (chapters 3, 4 and 7). A second and more complex stage, was the one of adapting the commercial software Comsol for nonlinear and vector time-independent modelling (chapters 5 and 6).

All the theoretical and numerical tools developed provided us with the knowledge to optimise several devices. Briefly, continuum spectra generation by dark solitons (chapter 3) is critically influenced by the soliton parameters, mainly frequency and greyness. When continuum spectra are to be generated from bright pulses with high input power, again the input light conditions have to be properly set to obtain the desired output spectral features (chapter 7). Such spectra can indeed also be generated by fundamental bright solitons (chapter 4), but here the fiber cross section (device geometry) has to vary in a very particular way together with the pulse frequency along the propagation. As in the latter case, the geometry of waveguide arrays also needs to be carefully adjusted for the observation of the nonlinear switching effect over the loss length, when using metallic substrates (chapter 5). Finally, the excitation of SPP's waves by spatial solitons is an important effect behind the work in chapter 6. However, because of its novelty, most of the effort was invested in the understanding of the hybrid solutions, *soliplasmons*, and the resonant dynamics is left for further

investigation.

Future work

The diversity of topics faced in the thesis left many opened problems and gave rise to all sort of questions and research interests. Tentative titles for potential future work arising from the thesis are motivated and listed in what follows.

Temporal solitons and supercontinuum

Generalised NLS equations and their impact in subwavelength waveguides.

The potential impact of eqns. 2.19 and 2.27 in SC modelling, specially in waveguides with subwavelength dimensions is still to be explored.

Theory for perturbed dark solitons: stability and adiabatic shift of soliton parameters in the presence of TOD and Raman effect.

The results in chapter 3 suggest a better understanding of the radiation amplitude might be required to match the theory with the modelling, what motivates an adiabatic model for the soliton frequency and greyness shifts. Furthermore, the Raman enhancement or suppression of the amplitude can be analysed by means of a similar perturbation theory to that developed here, accounting for the Raman term. It is expected that accounting for the nonlinear terms associated to the perturbation would bring insight about the little dark soliton emitted onto the tail in which there is no radiation (see e.g., fig. 3.5). Moreover, proving the stability of dark solitons is still an opened formal problem, even in the simpler case the NLSE.

Soliton radiation mechanisms and conservative Lagrangian formulation for dissipative effects.

Cherenkov radiation, Airy waves and cascaded effects are known types of solitonic radiation. New or modified mechanisms of radiation emission (such as Hawking's radiation) might arise when accounting for higher order terms in the GNLSE. A possibility to explore this is through the local phase invariance applied on the Lagrangians of the GNLS-type equations (see e.g., eq.2.41).

Non radiative solitonic corrections: kinks and shock waves.

Higher order effects do not only induce emission of radiation, but also modifications to the soliton profile [Karpman93]. The contribution to the standard shock term [Agrawal07] appears in section 2.3.3 (see eq. 2.43) in a modified way. Although introduced in a rather *artificial* way it can be actually found as in [Tran09]. The two different ways of accounting for shocks are conceptually different, since the latter conserves the Hamiltonian and the former does not. Further studies of shock and kinks (see e.g., [Frantzeskakis97]) should clarify the proper way to describe and the physical consequences in bright and dark solitons.

Variational theory for soliton propagation under power consuming and Hamiltonian dissipative effects.

Eq. 2.46 motivates the development of models which describe the dynamics of solitons with decreasing power along propagation in uniform or tapered fibers. Such models could provide, e.g., support to the results presented in chapter 4 and generalisation of well-known results, such as [Gordon86].

Optimisation of soliton red-shift in tapered fibres.

Optimising a soliton red-shift around the second zero GVD wavelength of a fiber, keeping small the Cherenkov radiation and big the SSFS ratio is still an opened problem which could find applications in UV generation.

Polychromatic IR extended Cherenkov radiation in tapered fibres.

Radiation trapping across the second GVD wavelength by a single soliton is only possible in a tapered fiber. Tapering can provide control on further red-shifting of the radiation.

Coupled systems

Bifurcation theory for characterising the NL modes of waveguide arrays.

Results in chapter 5 showed that bifurcations appear in the system of three waveguides at a lower power than for the two waveguides. Together with the shorter beat length, arrays of a large amount of waveguides my offer a good alternative for low power nonlinear switching over shorter propagation distances.

Spin model for amplitude-phase dynamics for on resonance soliplasmons.

Description of the phase-amplitude dynamics observed in the modelling of chapter 6 requires further development of the model. A promising approach is the spin (Maxwell-Bloch) model introduced through the density matrix formalism.

Attractive and repulsive intra soliplasmon forces.

On and *off* phase between plasmon and soliton, plus the exposure to reflections with the metal, motivate the inclusion of the soliton position as a free parameter in the model developed in chapter 6.

A temporal equation for soliplasmon supermodes.

Temporal dynamics associated to soliplasmons is motivated by the stable set, with $\delta = \pi$, having anomalous dispersion ($d\beta^2/d\omega^2 < 0$) for frequencies around the crossing-point and above (see fig. 6.2).

Two colour soliplasmons and UV generation.

Fig. 6.1 shows that the coupling between a soliton and a plasmon ($\beta_s = \beta_p$) indeed occurs when they have different frequencies too, what could originate *two colour soliplasmons*. Besides, further matching with the radiation in the metal above plasma frequency might provide a method for UV generation. Similar ideas matching several colour nonlinear modes through their group indices have been explored in [Skryabin04].

Appendix A

Numerical method to compute stationary soliplasmons

The numerical solutions in section 6.4.2 are compute numerically by solving the equations

$$\hat{\mathcal{L}}_{1D}\mathcal{E}_x = \beta^2\mathcal{E}_x,\ \hat{\mathcal{L}}_{1D} \equiv \partial_x^2 + \partial_x\left(\frac{1}{\epsilon}\partial_x\epsilon\circ\right) + k^2\epsilon \tag{A.1}$$

$$\epsilon = \epsilon_L + \chi^{(3)}\left[|\mathcal{E}_x|^2 + |\mathcal{E}_z|^2\right],\ \mathcal{E}_z = -\frac{i}{\beta}\left[\epsilon^{-1}\partial_x(\epsilon\mathcal{E}_x)\right], \tag{A.2}$$

as a self-consistent linear problem, using eq. A.2 as a constrain and keeping β as close as possible to the desired propagation constant, β_{sp}. Because the transversal derivatives are performed using the *fast Fourier transform* (FFT) and its inverse, periodic boundary conditions are required, so the numerical domain is defined by a large nonlinear dielectric region surrounded by metal ends.

The algorithm is sketched in fig. A.1 and works as follows. In first place $\mathcal{E}_x$ is given as a Gaussian with certain norm $\int dx|\mathcal{E}_x|$ and at a certain distance to the target metal interface, being the effect of the second interface negligible. This introduces a self-modulated profile of the refractive index ($n = \sqrt{\epsilon}$) since the very beginning and hence forces the algorithm to keep the soliton component relatively close to the one metal interface, what in turn prevents from convergence to the modes of the large dielectric waveguide. With this, the eigenvalues (β^2) and eigenvectors ($\mathcal{E}_x(x)$) of the operator $\hat{\mathcal{L}}_{1D}$ are computed as if the problem was a linear one. The eigenvector which qualitatively resembles more the targeted profile is chosen. However, the numerical

method returns the eigenvector normalised as $\int dx|\mathcal{E}_x| \equiv 1$, so it needs to be rescaled in order to have a propagation constant $\beta \approx \beta_{sp}$. This scaling is done as follows. The operator $\hat{\mathcal{L}}_{1D}$ is regarded to as

$$\hat{\mathcal{L}}_{1D} = \hat{\mathcal{O}}_1 + \hat{\mathcal{O}}_2,\ \hat{\mathcal{O}}_1 \equiv \partial_x^2 + \partial_x\left(\frac{1}{\epsilon}\partial_x\epsilon\circ\right),\ \hat{\mathcal{O}}_2 \equiv k^2\epsilon, \tag{A.3}$$

and we need to find $e_x = N\mathcal{E}_x$ such that $\hat{\mathcal{L}}_{1D}(e_x)e_x = \beta_{sp}^2 e_x$, so

$$\beta_{sp}^2 = \frac{\langle e_x \mid \hat{\mathcal{L}}_{1D}(e_x) \mid e_x\rangle}{\langle e_x \mid e_x\rangle} = \frac{\langle e_x \mid \hat{\mathcal{O}}_1(e_x) \mid e_x\rangle}{\langle e_x \mid e_x\rangle} + \frac{\langle e_x \mid \hat{\mathcal{O}}_2(e_x) \mid e_x\rangle}{\langle e_x \mid e_x\rangle} =$$
$$\langle \mathcal{E}_x \mid \hat{\mathcal{O}}_1(N\mathcal{E}_x) \mid \mathcal{E}_x\rangle + N^2\langle \mathcal{E}_x \mid \hat{\mathcal{O}}_2(N\mathcal{E}_x) \mid \mathcal{E}_x\rangle,$$

what leads to the transcendent equation for the normalisation factor

$$N^2 = \frac{\beta_{sp}^2 - \langle \mathcal{E}_x \mid \hat{\mathcal{O}}_1(N\mathcal{E}_x) \mid \mathcal{E}_x\rangle}{\langle \mathcal{E}_x \mid \hat{\mathcal{O}}_2(N\mathcal{E}_x) \mid \mathcal{E}_x\rangle}, \tag{A.4}$$

which, together with $\epsilon = \epsilon_L + \chi^{(3)}\left[|\mathcal{E}_x|^2 + |\mathcal{E}_z|^2\right]$, is solved iteratively inside the code (iterative processes are symbolised by the circular arrows in fig. A.1). After this, the estimate of $\mathcal{E}_z$ is done, with eq. A.2. The new values of $\mathcal{E}_x$ and $\mathcal{E}_z$ initialise the next iteration and the process carries on until the change between two subsequent solutions, $\int_x \left[|\mathcal{E}_x^{(1)}|^2 - |\mathcal{E}_x^{(0)}|^2\right]$, does not experience a change bigger than the tolerance, which is usually 10^{-6} in the propagation constant.

The biggest issue of this method is that the soliton possition can not be kept at a strictly fixed distance from the interafce. An alternative is to restrict to the study of the waveguide MDKDM only (see section 6.4.4), which not only is favorable from the numercal point of view, but seems to be the best experimental set-up, since the soliton can not be sent away by the metal reflections (see sections 6.5 and 6.5.1).

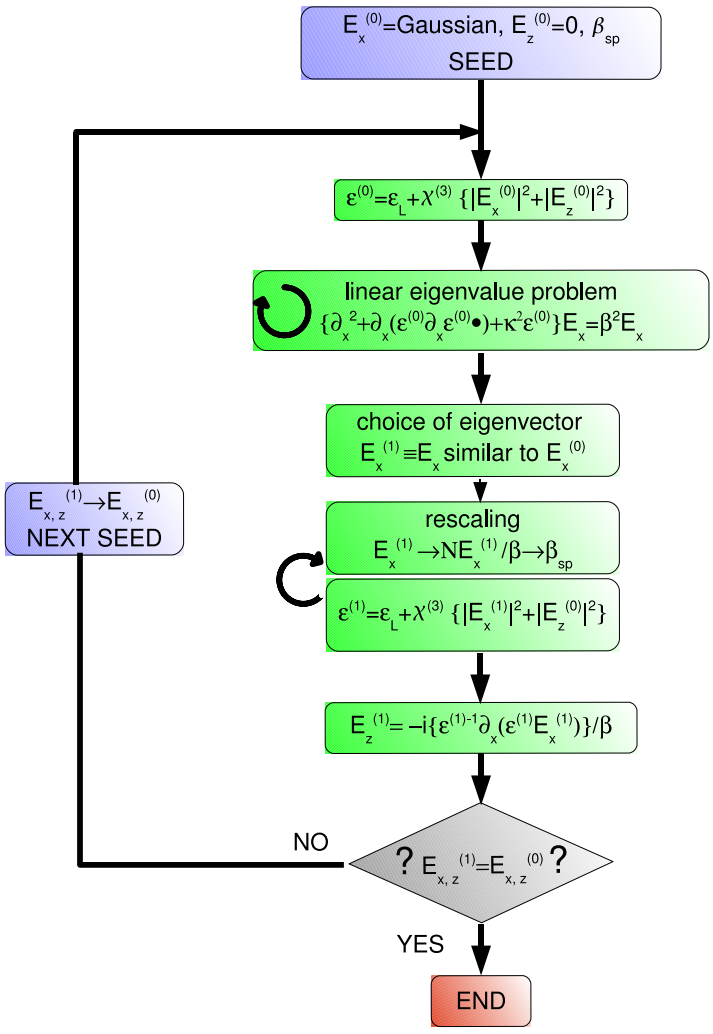

Figure A.1: Scheme of the algorithm used to find stationary soliplasmon solutions.

Appendix B

Papers, conferences and workshops

Papers published

C. Milián, D. V. Skryabin and A. Ferrando, *Continuum generation by dark solitons*, **OL** (34) 14, pp. 2096 (2009).

C. Milián and D. V. Skryabin, *Nonlinear switching in arrays of semiconductor on metal photonic wires*, **APL** (98) 11, pp. 111104 (2010).

Paper submitted

C. Milián, A. Ferrando, D. V. Skryabin, *Polychromatic Cherenkov radiation and supercontinuum in tapered optical fibers*, submitted to JOSAB (with results from section 4.3).

Paper in preparation

A Maxwell equation approach to nonlinear excitations of surface plasmon polaritons, with all the results presented in chapter 6.

Selected workshop and conference contributions

C. Milián, D. V. Skryabin, A. Ferrando, *Continuum generation by dark solitons in optical fibers* Oral presentation Localized Excitations in Nonlinear COmplex Systems (LENCOS 09) Sevilla (Spain), 14-17/07/2009

G. Moltó, M. Arevalillo-Herráez, C. Milián, M. Zacarés, V. Hernández, A. Ferrando *Optimization of Supercontinuum spectrum using genetic algorithms on service-oriented grids*, ISBN 978-84-9745-406-3 (IBERGRID 09) Valencia (Spain), 20-22/05/2009

A. Ferrando, C. Milián, D. Ceballos, and D.V. Skryabin *Stability of soliplasmon excitations at metal/dielectric interfaces* (invited talk) International Workshop on NONLINEAR PHOTONICS (NLP*2011) Kharkov (Ukraine), 06/09/2011

A. Ferrando, C. Milián, N. González, G. Moltó, P. Loza, M. Arevalillo-Herráez, M. Zacarés, I. Torres-Gómez, and V. Hernández *Designing supercontinuum spectra using Grid technology* ISBN 9780819483607 (and invited talk) 2nd Workshop on Specialty Optical Fibers and Their Applications (WSOF-2) Oaxaca (México), 10/2010

Bibliography

[Aceves96] A. B. Aceves, C. De Angelis, T. Peschel, R. Muschall, F. Lederer, S. Trillo and S. Wabnitz. "Discrete self-trapping, soliton interactions, and beam steering in nonlinear waveguide arrays". *Phys. Rev. E* **53**, 1172 (1996). doi:10.1103/PhysRevE.53.1172.

[Afanasjev96] V. V. Afanasjev, Y. S. Kivshar and C. R. Menyuk. "Effect of third-order dispersion on dark solitons". *Opt. Lett.* **21**, 1975 (1996). doi:10.1364/OL.21.001975.

[Agrawal94] R. B. Agrawal and K. Deb. "Simulated Binary Crossover for Continuous Search Space". Technical report (1994).

[Agrawal07] G. P. Agrawal. *Nonlinear Fiber Optics*. Academic Press (2007).

[Agrawal08] G. P. Agrawal. *Aplications of Nonlinear Fiber Optics*. Academic Press (2008).

[Aitchison97] J. S. Aitchison, D. C. Hutchings, J. U. Kang, G. I. Stegeman and A. Villeneuve. "The nonlinear optical properties of AlGaAs at the half band gap". *Quantum Electronics, IEEE Journal of* **33**, 341 (1997). ISSN 0018-9197. doi:10.1109/3.556002.

[Akhmediev95] N. Akhmediev and M. Karlsson. "Cherenkov radiation emitted by solitons in optical fibers". *Phys. Rev. A* **51**, 2602 (1995). doi:10.1103/PhysRevA.51.2602.

[Alfano70a] R. R. Alfano and S. L. Shapiro. "Emission in the Region 4000 to 7000 Å Via Four-Photon Coupling in Glass". *Phys. Rev. Lett.* **24**, 584 (1970). doi:10.1103/PhysRevLett.24.584.

[Alfano70b] R. R. Alfano and S. L. Shapiro. "Observation of Self-Phase Modulation and Small-Scale Filaments in Crystals and Glasses". *Phys. Rev. Lett.* **24**, 592 (1970). doi:10.1103/PhysRevLett.24.592.

[Alonso06] J. M. Alonso, V. Hernández and G. Moltó. "GMarte: Grid middleware to abstract remote task execution". *Concurrency and Computation: Practice and Experience* **18**, 2021 (2006). ISSN 1532-0634. doi:10.1002/cpe.1052.

[Anderson83] D. Anderson and M. Lisak. "Nonlinear asymmetric self-phase modulation and self-steepening of pulses in long optical waveguides". *Phys. Rev. A* **27**, 1393 (1983). doi:10.1103/PhysRevA.27.1393.

[Ashlock06] D. Ashlock. *Evolutionary comptutation for modeling and optimization*. Springer (2006).

[Auston84] D. H. Auston, K. P. Cheung, J. A. Valdmanis and D. A. Kleinman. "Cherenkov Radiation from Femtosecond Optical Pulses in Electro-Optic Media". *Phys. Rev. Lett.* **53**, 1555 (1984). doi:10.1103/PhysRevLett.53.1555.

[Aviles-Espinosa11] R. Aviles-Espinosa, G. Filippidis, C. Hamilton, G. Malcolm, K. J. Weingarten, T. Südmeyer, Y. Barbarin, U. Keller, S. I.C.O Santos, D. Artigas and P. Loza-Alvarez. "Compact ultrafast semiconductor disk laser: targeting GFP based nonlinear applications in living organisms". *Biomed. Opt. Express* **2**, 739 (2011). doi:10.1364/BOE.2.000739.

[Back93] T. Back. "Optimal Mutation Rates in Genetic Search". In "Proceedings of the fifth International Conference on Genetic Algorithms", pages 2–8. Morgan Kaufmann (1993).

[Biancalana04] F. Biancalana, D. V. Skryabin and A. V. Yulin. "Theory of the soliton self-frequency shift compensation by the resonant radiation in photonic crystal fibers". *Phys. Rev. E* **70**, 016615 (2004). doi:10.1103/PhysRevE.70.016615.

[Biancalana05] F. Biancalana. *Modelling of nonlinear effects in microstructured fibres*. Ph. D Thesis (2005).

[Bliokh09] K. Y. Bliokh, Y. P. Bliokh and A. Ferrando. "Resonant plasmon-soliton interaction". *Phys. Rev. A* **79**, 041803 (2009). doi:10.1103/PhysRevA.79.041803.

[Blow89] K.J. Blow and D. Wood. "Theoretical description of transient stimulated Raman scattering in optical fibers". *Quantum Electronics, IEEE Journal of* **25**, 2665 (1989). ISSN 0018-9197. doi:10.1109/3.40655.

[Born99] M. Born and E. Wolf. *Principles of Optics*. Cambridge University Press (1999).

[Boyd03] R. W. Boyd. *Nonlinear Optics*. Academic Press (2003).

[Bozhevolnyi06] S. I. Bozhevolnyi, V. S. Volkov, E. Devaux, J. Y. Laluet and T. W. Ebbesen. "Channel plasmon subwavelength waveguide components including interferometers and ring resonators". *Nature* **440**, 508 (2006). doi:10.1038/nature04594.

[Chapman10] B. H. Chapman, J. C. Travers, S. V. Popov, A. Mussot and A. Kudlinski. "Long wavelength extension of CW-pumped supercontinuum throughsoliton-dispersive wave interactions". *Opt. Express* **18**, 24729 (2010). doi:10.1364/OE.18.024729.

[Chernikov93] S. V. Chernikov, E. M. Dianov, D. J. Richardson and D. N. Payne. "Soliton pulse compression in dispersion-decreasing fiber". *Opt. Lett.* **18**, 476 (1993).

[Christodoulides88] D. N. Christodoulides and R. I. Joseph. "Discrete self-focusing in nonlinear arrays of coupled waveguides". *Opt. Lett.* **13**, 794 (1988).

[Courant66] R. Courant and D. Hilbert. *Methods of Mathematical Physics*, Vol. 1. John Wiley & Sons (1966).

[Davoyan08] A. R. Davoyan, I. V. Shadrivov and Y. S. Kivshar. "Nonlinear plasmonic slot waveguides". *Opt. Express* **16**, 21209 (2008). doi:10.1364/OE.16.021209.

[Davoyan09] A. R. Davoyan, I. V. Shadrivov and Y. S. Kivshar. "Self-focusing and spatial plasmon-polariton solitons". *Opt. Express* **17**, 21732 (2009).

[Davoyan10] A. R. Davoyan, I. V. Shadrivov, A. A. Zharov, D. K. Gramotnev and Y. S. Kivshar. "Nonlinear Nanofocusing in Tapered Plasmonic Waveguides". *Phys. Rev. Lett.* **105**, 116804 (2010). doi:10.1103/PhysRevLett.105.116804.

[Deb01] K. Deb. *Multi-Objective Optimization using Evolutionary Algorithms* . Wiley & Sons (2001).

[Dudley06] J. M. Dudley, G. Genty and S. Coen. "Supercontinuum generation in photonic crystal fiber". *Rev. Mod. Phys.* **78**, 1135 (2006). doi:10.1103/RevModPhys.78.1135.

[Durillo06] J. J. Durillo, A. J. Nebro, F. Luna, B. Dorronsoro and E. Alba. "jMetal: a Java Framework for Developing Multi-Objective Optimization Metaheuristics". Technical report (2006).

[Eisenberg98] H. S. Eisenberg, Y. Silberberg, R. Morandotti, A. R. Boyd and J. S. Aitchison. "Discrete Spatial Optical Solitons in Waveguide Arrays". *Phys. Rev. Lett.* **81**, 3383 (1998). doi: 10.1103/PhysRevLett.81.3383.

[Falk05] P. Falk, M. Frosz and O. Bang. "Supercontinuum generation in a photonic crystal fiber with two zero-dispersion wavelengths tapered to normal dispersion at all wavelengths". *Opt. Express* **13**, 7535 (2005).

[Feigenbaum07] E. Feigenbaum and M. Orenstein. "Plasmon-soliton". *Opt. Lett.* **32**, 674 (2007). doi:10.1364/OL.32.000674.

[Ferrando] A. Ferrando, C. Milián, N. González, G. Moltó, P. Loza, M. Arevalillo-Herráez, M. Zacarés, I. Torres-Gómez, and V. Hernández. "Designing supercontinuum spectra using Grid technology". ISBN 978-08-1948-360-7.

[Ferrando99] A. Ferrando, E. Silvestre, J. J. Miret, P. André s and M. V. Andrés. "Full-vector analysis of a realistic photonic crystal fiber". *Opt. Lett.* **24**, 276 (1999). doi:10.1364/OL.24.000276.

[Ferrando00] A. Ferrando, E. Silvestre, J. J. Miret and P. Andrés. "Nearly zero ultraflattened dispersion in photonic crystal fibers". *Opt. Lett.* **25**, 790 (2000). doi:10.1364/OL.25.000790.

[Finlayson90] N. Finlayson and G. I. Stegeman. "Spatial switching, instabilities, and chaos in a three waveguide nonlinear directional coupler". *Appl. Phys. Lett.* **56**, 2276 (1990). ISSN 0003-6951. doi:10.1063/1.102938.

[Finot06] C. Finot, J. M. Dudley and G. Millot. "Generation of dark solitons by interaction between similaritons in Raman fiber amplifiers". *Opt. Fib. Tech.* **12**, 217 (2006). ISSN 1068-5200. doi: 10.1016/j.yofte.2006.02.002.

[Foster04] I. Foster and C. Kesselman. *The grid: Blue print for a new computing infrastructure*. Elsevier (2004).

[Foster05] I. Foster. "Globus Toolkit Version 4: Software for Service-Oriented Systems". In Hai Jin, Daniel Reed and Wenbin Jiang, editores, "Network and Parallel Computing", Vol. 3779 of *Lecture Notes in Computer Science*, pages 2–13. Springer Berlin / Heidelberg (2005). ISBN 978-3-540-29810-6.

[Frantzeskakis97] D. J. Frantzeskakis. "Weak topological optical solitons in the femtosecond time scale". *J. Opt. Soc. Am. B* **14**, 2359 (1997).

[Gérôme07] F. Gérôme, K. Cook, A. K. George, W. J. Wadsworth and J. C. Knight. "Delivery of sub-100fs pulses through 8m of hollow-core fiber using soliton compression". *Opt. Express* **15**, 7126 (2007).

[Gorbach07] A. V. Gorbach and D. V. Skryabin. "Light trapping in gravity-like potentials and expansion os supercontinuum spectra in photonic-crystal fibres". *Nature Phot.* **1**, 653 (2007).

[Gorbach08] A. V. Gorbach and D. V. Skryabin. "Soliton self-frequency shift, non-solitonic radiation and self-induced transparencyin air-core fibers". *Opt. Express* **16**, 4858 (2008).

[Gordon86] J. P. Gordon. "Theory of the soliton self-frequency shift". *Opt. Lett.* **11**, 662 (1986).

[Hansen96] N. Hansen and A. Ostermeier. "Adapting Arbitrary Normal Mutation Distributions in Evolution Strategies: The Covariance Matrix Adaptation". pages 312–317. Morgan Kaufmann (1996).

[Hansen03] N. Hansen, S.D. Muller and P Koumoutsakos. "Reducing the Time Complexity of the Derandomized Evolution Strategy with Covariance Matrix Adaptation (CMA-ES)". *Evolutionary Computation* **11**, 1 (2003).

[Hasegawa73a] A. Hasegawa and F. Tappert. "Transmission of stationary nonlinear optical pulses in dispersive dielectric fibers. II. Normal dispersion". *Appl. Phys. Lett.* **23**, 171 (1973). ISSN 0003-6951. doi:10.1063/1.1654847.

[Hasegawa73b] A. Hasegawa and F. Tappert. "Transmission of stationary nonlinear optical pulses in dispersive dielectric fibers.I.Anomalous dispersion". *Appl. Phys. Lett.* **23**, 142 (1973). ISSN 0003-6951. doi:10.1063/1.1654836.

[Haus83] H. Haus and L. Molter-Orr. "Coupled multiple waveguide systems". *Quantum Electronics, IEEE Journal of* **19**, 840 (1983). ISSN 0018-9197. doi:10.1109/JQE.1983.1071950.

[her] http://heraeus-quarzglas.com/en/quarzglas/mechanicalproperties.

[Jackson62] J. D. Jackson. *Classical Electrodynamics*. John Wiley & Sons (1962).

[Jensen82] S. Jensen. "The nonlinear coherent coupler". *Quantum Electronics, IEEE Journal of* **18**, 1580 (1982). ISSN 0018-9197. doi:10.1109/JQE.1982.1071438.

[Judge09] A. C. Judge, O. Bang, B. J. Eggleton, B. T. Kuhlmey, E. C. Mägi, R. Pant and C. Martijn de Sterke. "Optimization of the soliton self-frequency shift in a tapered photonic crystal fiber". *J. Opt. Soc. Am. B* **26**, 2064 (2009).

[Judge10] A. C. Judge, O. Bang and C. Martijn de Sterke. "Theory of dispersive wave frequency shift via trapping by a soliton in an axially nonuniform optical fiber". *J. Opt. Soc. Am. B* **27**, 2195 (2010).

[Karpman93] V. I. Karpman. "Stationary and radiating dark solitons of the third order nonlinear Schrödinger equation". *Phys. Lett. A* **181**, 211 (1993). ISSN 0375-9601. doi:DOI:10.1016/0375-9601(93)90641-C.

[Kenny91] R. P. Kenny, T.A. Birks and K.P. Oakley. "Control of optical fibre taper shape". *Electronics Letters* **27**, 1654 (1991). ISSN 0013-5194. doi:10.1049/el:19911034.

[Kivshar97] Y S Kivshar and B Luther-Davies. "Dark optical solitons: physics and applications". *Physics Reports* **298**, 81 (1997).

[Kivshar06] Y. S. Kivshar and G. P. Agrawal. *Optical solitons. From fibers to photonic crystals.* Academic Press (2006).

[Knight03] J. C. Knight. "Photonic crystal fibres". *Nature* **424**, 847 (2003). doi:10.1038/nature01940.

[Koos07] C. Koos, L. Jacome, C. Poulton, J. Leuthold and W. Freude. "Nonlinear silicon-on-insulator waveguides for all-optical signal processing". *Opt. Express* **15**, 5976 (2007).

[Krasavin10] A. V. Krasavin and A. V. Zayats. "Silicon-based plasmonic waveguides". *Opt. Express* **18**, 11791 (2010).

[Kudlinski06] A. Kudlinski, A. K. George, J. C. Knight, J. C. Travers, A. B. Rulkov, S. V. Popov and J. R. Taylor. "Zero-dispersion wavelength decreasing photonic crystal fibers for ultraviolet-extended supercontinuum generation". *Opt. Express* **14**, 5715 (2006).

[Latkin07] A. I. Latkin, S.i K. Turitsyn and A. A. Sysoliatin. "Theory of parabolic pulse generation in tapered fiber". *Opt. Lett.* **32**, 331 (2007). doi:10.1364/OL.32.000331.

[Lederer08] F. Lederer, G. I. Stegeman, D. N. Christodoulides, G. Assanto, M. Segev and Y. Silberberg. "Discrete solitons in optics". *Physics Reports* **463**, 1 (2008). ISSN 0370-1573. doi: DOI:10.1016/j.physrep.2008.04.004.

[Liu07] Y. Liu, G. Bartal, D. A. Genov and X. Zhang. "Subwavelength Discrete Solitons in Nonlinear Metamaterials". *Phys. Rev. Lett.* **99**, 153901 (2007). doi:10.1103/PhysRevLett.99.153901.

[Maier07] S. A. Maier. *Plasmonics: fundamentals and applications.* Springer (2007).

[Maiman60] T. H. Maiman. "Stimulated Optical Radiation in Ruby". *Nature* **187**, 493 (1960). doi:10.1038/187493a0.

[Marini09] A. Marini, A. V. Gorbach, D. V. Skryabin and A. V. Zayats. "Amplification of surface plasmon polaritons in the presence of nonlinearity and spectral signatures of threshold crossover". *Opt. Lett.* **34**, 2864 (2009). doi:10.1364/OL.34.002864.

[Marini10a] A. Marini, A. V. Gorbach and D. V. Skryabin. "Coupled-mode approach to surface plasmon polaritons in nonlinear periodic structures". *Opt. Lett.* **35**, 3532 (2010). doi:10.1364/OL.35.003532.

[Marini10b] A. Marini and D. V. Skryabin. "Ginzburg-Landau equation bound to the metal-dielectric interface and transverse nonlinear optics with amplified plasmon polaritons". *Phys. Rev. A* **81**, 033850 (2010). doi:10.1103/PhysRevA.81.033850.

[Mihalache87] D. Mihalache, G. I. Stegeman, C. T. Seaton, E. M. Wright, R. Zanoni, A. D. Boardman and T. Twardowski. "Exact dispersion relations for transverse magnetic polarized guided waves at a nonlinear interface". *Opt. Lett.* **12**, 187 (1987). doi:10.1364/OL.12.000187.

[Milián09] C. Milián, D. V. Skryabin and A. Ferrando. "Continuum generation by dark solitons". *Opt. Lett.* **34**, 2096 (2009). doi:10.1364/OL.34.002096.

[Milián11] C. Milián and D. V. Skryabin. "Nonlinear switching in arrays of semiconductor on metal photonic wires". *Appl. Phys. Lett.* **98**, 111104 (2011). doi:10.1063/1.3565167.

[Mills91] D. L. Mills. *Nonlinear Optics*. Springer-Verlag (1991).

[Mollenauer06] L. Mollenauer and J. Gordon. *Solitons in Optical Fibers: Fundamentals and Applcations*. Academic Press (2006).

[Moltó] G. Moltó, M. Arevalillo-Herráez, C.Milián, M. Zacarés, V. Hernández and A. Ferrando. "Optimization of Supercontinuum spectrum using genetic algorithms on service-oriented grids". ISBN 978-84-9745-406-3.

[Moltó08] G. Moltó, V. Hernández and J. M. Alonso. "A service-oriented WSRF-based architecture for metascheduling on computational Grids". *Future Gener. Comput. Syst.* **24**, 317 (2008). ISSN 0167-739X. doi:10.1016/j.future.2007.05.001.

[Mosley10] P. J. Mosley, W. C. Huang, M. G. Welch, B. J. Mangan, W. J. Wadsworth and J. C. Knight. "Ultrashort pulse compression and delivery in a hollow-core photonic crystal fiber at 540 nm wavelength". *Opt. Lett.* **35**, 3589 (2010).

[Pant10] R. Pant, A. C. Judge, E. C. Magi, B. T. Kuhlmey, Ma. de Sterke and B. J. Eggleton. "Characterization and optimization of photonic crystal fibers for enhanced soliton self-frequency shift". *J. Opt. Soc. Am. B* **27**, 1894 (2010).

[Rakic98] A. D. Rakic, A. B. Djurišic, J. M. Elazar and M. L. Majewski. "Optical Properties of Metallic Films for Vertical-Cavity Optoelectronic Devices". *Appl. Opt.* **37**, 5271 (1998). doi: 10.1364/AO.37.005271.

[Ranka00] J. K. Ranka, R. S. Windeler and A. J. Stentz. "Visible continuum generation in air-silica microstructure optical fibers with anomalous dispersion at 800 nm". *Opt. Lett.* **25**, 25 (2000). doi:10.1364/OL.25.000025.

[Riley06] K. F. Riley, M. P. Hobson and S. J. Bence. *Mathematical methods for physics and engineering.* Cambridge University Press (2006).

[Rothenberg91] J. E. Rothenberg. "Dark soliton trains formed by visible pulse collisions in optical fibers". *Optics Communications* **82**, 107 (1991). ISSN 0030-4018. doi:DOI:10.1016/0030-4018(91) 90200-W.

[Rothenberg92] J. E. Rothenberg and H. K. Heinrich. "Observation of the formation of dark-soliton trains in optical fibers". *Opt. Lett.* **17**, 261 (1992). doi:10.1364/OL.17.000261.

[Russell03] P. St. Russell. "Photonic Crystal Fibers". *Science* **299**, 358 (2003). doi:10.1126/science.1079280.

[Saleh11a] M. F. Saleh and F. Biancalana. "Understanding the dynamics of photoionization-induced solitons in gas-filled hollow-core photonic crystal fibers". *submitted* **0** (2011).

[Saleh11b] M. F. Saleh, W. Chang, P. Hölzer, A. Nazarkin, J. C. Travers, N. Y. Joly, P. St. J. Russell and F. Biancalana. "Theory of photoionization-induced blueshift of ultrashort solitons in gas-filled hollow-core photonic crystal fibers". *Phys. Rev. Lett.* **107**, 203902 (2011).

[Salgueiro10] J. R. Salgueiro and Y. S. Kivshar. "Nonlinear plasmonic directional couplers". *Appl. Phys. Lett.* **97**, 081106 (2010). doi: 10.1063/1.3482939.

[Sears75] F. W. Sears. *Thermodynamics, Kinetic Theory, and Statistical Thermodynamics*. Addison Wesley (1975).

[Senior95] T. B. A. Senior and J. L. Volakis. *Approximate boundary conditions in electromagnetics*. IEE (1995).

[Shahraam Afshar09] V. Shahraam Afshar and T. M. Monro. "A full vectorial model for pulse propagation in emerging waveguides with subwavelength structures part I: Kerr nonlinearity". *Opt. Express* **17**, 2298 (2009).

[Silvestre98] E. Silvestre, M. V. Andres and P. Andres. "Biorthonormal-basis method for the vector description of optical-fiber modes". *Lightwave Technology, Journal of* **16**, 923 (1998). ISSN 0733-8724. doi:10.1109/50.669048.

[Skryabin03] D. V. Luan Skryabin, F., J. C. Knight, and P. St. J. Russell. "Soliton Self-Frequency Shift Cancellation in Photonic Crystal Fibers". *Science* **301**, 1705 (2003). doi:10.1126/science.1088516.

[Skryabin04] D. V. Skryabin, F. Biancalana, D. M. Bird and F. Benabid. "Effective Kerr nonlinearity and two-color solitons in photonic band-gap fibers filled with a Raman active gas". *Physical Review Letters* **93**, 143907 (2004). doi:http://dx.doi.org/10.1103/PhysRevLett.93.143907.

[Skryabin06] D. V. Skryabin, A. V. Yulin and A. I. Maimistov. "Localized Polaritons and Second-Harmonic Generation in a Resonant Medium with Quadratic Nonlinearity". *Phys. Rev. Lett.* **96**, 163904 (2006). doi:10.1103/PhysRevLett.96.163904.

[Skryabin10] D. V. Skryabin and A. V. Gorbach. "Colloquium: Looking at a soliton throught the prism of optical supercontinuum". *Rev. Mod. Phys.* **82**, 1287 (2010). doi:10.1103/RevModPhys.82.1287.

[Skryabin11] D. V. Skryabin, A. V. Gorbach and A. Marini. "Surface-induced nonlinearity enhancement of TM modes in planar subwavelength waveguides". *J. Opt. Soc. Am. B* **28**, 109 (2011). doi: 10.1364/JOSAB.28.000109.

[Snyder91] A. W. Snyder, D. J. Mitchell, L. Poladian, D. R. Rowland and Y. Chen. "Physics of nonlinear fiber couplers". *J. Opt. Soc. Am. B* **8**, 2102 (1991).

[Stark11a] S. P. Stark, F. Biancalana, A. Podlipensky and P. St. J. Russell. "Nonlinear wavelength conversion in photonic crystal fibers with three zero-dispersion points". *Phys. Rev. A* **83**, 023808 (2011). doi:10.1103/PhysRevA.83.023808.

[Stark11b] S. P. Stark, A. Podlipensky and P. St. J. Russell. "Soliton Blueshift in Tapered Photonic Crystal Fibers". *Phys. Rev. Lett.* **106**, 083903 (2011). doi:10.1103/PhysRevLett.106.083903.

[Stolen89] R. H. Stolen, J. P. Gordon, W. J. Tomlinson and H. A. Haus. "Raman response function of silica-core fibers". *J. Opt. Soc. Am. B* **6**, 1159 (1989).

[Szabo91] B Szabo and I Babuska. *Finite Element Analysis*. John Wiley & Sons (1991).

[Tran09] T. X. Tran and F. Biancalana. "An accurate envelope equation for lightpropagation in photonic nanowires: newnonlinear effects". *Opt. Express* **17**, 17934 (2009). doi:10.1364/OE.17.017934.

[Travers07] J. C. Travers, J. M. Stone, A. B. Rulkov, B. A. Cumberland, A. K. George, S. V. Popov, J. C. Knight and J. R. Taylor.

"Optical pulse compression in dispersion decreasing photonic crystal fiber". *Opt. Express* **15**, 13203 (2007).

[Travers09] J. C. Travers and J. R. Taylor. "Soliton trapping of dispersive waves in tapered optical fibers". *Opt. Lett.* **34**, 115 (2009).

[Tsakmakidis07] K. L. Tsakmakidis, A. D. Boardman and O. Hess. "'Trapped rainbow' storage of light in metamaterials". *Nature* **450**, 397 (2007). doi:10.1038/nature06285.

[Vakhitov73] N. G. Vakhitov and A.A. Kolokolov. *Izv. Vyss. Uchebn. Zaved. Radiofiz.* **16**, 1020 (1973).

[Vukovic10] N. Vukovic and N. G. R. Broderick. "Method for improving the spectral flatness of the supercontinuum at 1.55 μm in tapered microstructured optical fibers". *Phys. Rev. A* **82**, 043840 (2010). doi:10.1103/PhysRevA.82.043840.

[Wai86] P. K. A. Wai, C. R. Menyuk, Y. C. Lee and H. H. Chen. "Nonlinear pulse propagation in the neighborhood of the zero-dispersion wavelength of monomode optical fibers". *Opt. Lett.* **11**, 464 (1986).

[Wan07] W. Wan, S. Jia and J. W. Fleischer. "Dispersive, superfluid-like shock waves in nonlinear optics". *Nature Phys.* **3**, 46. 21 p (2007).

[Weiner89] A. M. Weiner, R. N. Thurston, W. J. Tomlinson, J. P. Heritage, D. E. Leaird, E. M. Kirschner and R. J. Hawkins. "Temporal and spectral self-shifts of dark optical solitons". *Opt. Lett.* **14**, 868 (1989). doi:10.1364/OL.14.000868.

[Wiggins90] S. Wiggins. *Inytoduction to Applied Nonlinear Dynamical Systems and Chaos.* Springer-Verlag (1990).

[Wurtz06] G. A. Wurtz, R. Pollard and A. V. Zayats. "Optical Bistability in Nonlinear Surface-Plasmon Polaritonic Crystals". *Phys. Rev. Lett.* **97**, 057402 (2006). doi:10.1103/PhysRevLett.97.057402.

[Ye10] F. Ye, D. Mihalache, B. Hu and N. C. Panoiu. "Subwavelength Plasmonic Lattice Solitons in Arrays of Metallic Nanowires". *Phys. Rev. Lett.* **104**, 106802 (2010). doi:10.1103/PhysRevLett.104.106802.

[Ye11] F. Ye, D. Mihalache, B. Hu and N. C. Panoiu. "Subwavelength vortical plasmonic lattice solitons". *Opt. Lett.* **36**, 1179 (2011). doi:10.1364/OL.36.001179.

[Zayats05] A. V. Zayats, I. I. Smolyaninov and A. A. Maradudin. "Nano-optics of surface plasmon polaritons". *Physics Reports* **408**, 131 (2005). ISSN 0370-1573. doi:DOI:10.1016/j.physrep.2004.11.001.